Approximation techniques in strongly correlated electron systems

A dissertation submitted to the
Division of Research and Advanced Studies
of the University of Cincinnati
in partial fulfillment of the requirements for the degree of
DOCTOR OF PHILOSOPHY
at the Department of Physics of the College of Arts and Sciences

Karan Aryanpour

M.Sc., University of Cincinnati, Cincinnati, 1999
B.Sc, Sharif University of Technology, Tehran, 1996

August 2003

Committee Chair: Prof. Mark Jarrell

Abstract

This dissertation details the study and application of three approximation techniques for strongly correlated electron systems. These techniques are the dynamical mean field approximation (DMFA), dynamical cluster approximation (DCA) and cellular dynamical mean field theory (CDMFT). The DMFA is a local approximation in which electron-electron correlations are only dynamical in time and all non-local correlations in space are suppressed. This technique becomes exact in the limit of infinite dimensions. The DCA and CDMFT are both approaches to systematically add non-local correlations to the DMFA. The DCA is a cluster technique in reciprocal space while the CDMFT is a cluster technique in real space. Both techniques become exact when the cluster size diverges.

Two chapters of this dissertation have been dedicated to the DCA, its combination with a perturbation theory technique called the fluctuation exchange approximation (FLEX) to study the Hubbard model and a microscopic theory that uniquely prescribes how to implement the DCA in terms of Feynman diagrammatics for the thermodynamic potential. A comparison between the convergence behaviors of the DCA and CDMFT is the topic of another chapter. Lastly, the DMFA is employed to study ferromagnetism in III-V dilute magnetic semiconductors with the particular example of $Ga_{1-x}Mn_xAs$.

The last chapter summarizes the results and conclusions presented in individual chapters and outlines prospective future developments.

Preface

This dissertation is the collection of several projects undertaken between July 1999 and August 2003 under the supervision of Prof. Mark Jarrell in the Condensed Matter Theory group at the University of Cincinnati, Cincinnati, OH, and in collaboration with:
Dr. Matthias H. Hettler (Material Science Division, Argonne National Laboratory (ANL), Argonne, IL and Forschungszentrum Karlsruhe, Institut für Nanotechnologie, Karlsruhe, Germany)
Dr. Thomas. A. Maier (Condensed Matter Theory group at the University of Cincinnati, Cincinnati, OH)
Dr. Randy Fishman and Dr. Juana Moreno (Solid State Division, Oak Ridge National Laboratory (ORNL), Oak Ridge, TN)

Except where reference is made to the work of others, this dissertation is the result of my own work and everything which is the outcome of work done in collaboration has been explicitly cited. This thesis has not been submitted in whole or in part for any degree or diploma at this or any other institute.

Karan Aryanpour

August 2003

Acknowledgements

I greatly appreciate all the faculty members of the Physics Department at the University of Cincinnati for their contributions to my education and providing a friendly and intellectual atmosphere in which I could develop my career as a physicist. In particular, I am indebted to my advisor, Prof. Mark Jarrell, for his outstanding supervision and discipline, thoughtful insight, and financial support over the past few years.

I am very grateful to my co-advisor, Dr. Matthias H. Hettler for all that he taught me, and also his admirable patience and care in helping me through the hardships in the early days of my research. Our collaboration was indeed a great opportunity and pleasure for me.

My special thanks to my other collaborators, Dr. Thomas. A. Maier, Dr. Randy Fishman and Dr. Juana Moreno without whose contributions and insight all that I have achieved would have taken far longer. Also my regards to Prof. John J. Deisz and Prof. Samuel Moukouri for their very helpful comments and suggestions throughout these years and to Dr. Paul R. C. Kent for his help in the preparation of this dissertation.

I would like to collectively acknowledge and thank the Physics Department administration and staff, in particular Prof. Frank Pinski, the chair, Mr. David Will, Mrs. Melody Whitlock and Mrs. Donna Deutenberg, for their utmost efforts in facilitating daily tasks and providing a comfortable working environment.

Finally, I dedicate this dissertation to all my great teachers including my beloved parents Rouhi and Mina and my beloved brother Ardevan without whose love, care and attention I would not be who I am today. Finally, I would like to make a special dedication to the late Prof. Fereydoon Mansouri whose presence in my defense session was greatly missed. May he rest in peace.

Contents

List of Figures

Chapter 1

Introduction

1.1 Strongly correlated electron systems

Strongly correlated electron systems are characterized by an electron- electron repulsions U which is much larger than the energies associated with the overlap of atomic orbitals belonging to different atoms. The latter is usually characterized by the width W of the dispersion band. The ratio U/W normally becomes large in systems with well-localized $4f$ or $5f$ electrons such as rare-earth or actinide atoms. However, d electron systems like CoO or La_2CuO_4 can at times be strongly correlated. [5]

Among many proposed models for these systems, the *Hubbard model* is one of the most fundamental Hamiltonians that takes into consideration the hoppings of electrons amongst the atomic orbitals due to their overlaps and also the Coulomb repulsion between electrons residing on the same lattice site. Despite the relative simplicity of the local electron-electron interaction in this model, there is no exact solution to it except in one and infinite dimensions. Of interest is the two-dimensional Hubbard model as a candidate for studying high-T_c superconductivity in cuprates. [6] This model has certain limitations in terms of describing the realistic physics of solids. Nevertheless, there is hope that its basic features can be generalized to more realistic models. There is a great amount of attention to the two-dimensional Hubbard model and some of its properties in the next two chapters of this dissertation. This model has been the basis for some of the approximation techniques employed in this project. Certain well-known features of the Hubbard model (e.g. anti-ferromagnetism at half filling) can be verified by these approximation schemes. The goal is to study the abilities and also limitations of different approximation methods in exhibiting these features in order to benchmark the one that yields the most physically realistic results. In chapter 3, the Hubbard model is also envoked to derive a microscopic theory for one of these approximation methods (DCA). However, this microscopic theory will be generalized to other models as well later in the same chapter.

Another interesting topic is magnetic impurities embedded in the sea of conduction electrons (Kondo [7], Anderson [8]). These systems are usually produced by dissolving transition metal ions or rare earth impurities in another metal and exhibit anomalous transport properties. For example, instead of decreasing monotonically with temperature, the resistance shows a minimum at a temperature T_K (Kondo temperature) as a characteristic property of the system. Kondo showed that this anomaly along with few others (e.g. in the heat conduction) are due to an important correlation or many-body effect. He introduced a Hamiltonian in which the conduction electrons interact with impurities having internal degrees of freedom through their spins S. It is understood that when conduction electrons are scattered off non-magnetic impurities, the computation of the scattering cross section is a purely one-electron scattering problem. Due to the lack of spin degrees of freedom and consequently the Pauli exclusion principle, the Fermi distribution function appears nowhere in the calculations. By introducing internal degrees of freedom like the spin in magnetic impurities, the Fermi distribution function can no longer be omitted. The scattering is therefore a many-body problem involving all the electrons of the system entering through the Fermi function. [5] This dissertation is less focused on this particular topic in strongly correlated electrons. Nonetheless, it uses some of its general ideas to describe ferromagnetism in magnetic impurity doped semiconductors.

Recently, ferromagnetic semiconductors have become a major focus in both physics and industry as these materials are the bases of a newly developed field called *spintronics.* In spintronics, the spin degree of freedom of charge carriers (electrons or holes) is utilized to carry information. Due to the the insolubility of most magnetic impurities in semiconductors, the preparation of these compounds are normally difficult. However, recently, the *molecular beam epitaxy* (MBE) technique [9] has led to the successful growth of ferromagnetic $Ga_{1-x}Mn_xAs$. G. Zaránd and B. Jankó [10] have employed a model to study the competition between ferromagnetism and disorder in $Ga_{1-x}Mn_xAs$. This Hamiltonian takes into account the spin-orbit coupling of the valance band holes by simplifying a more general model originally introduced by Kohn and Luttinger. [11] Based on this model and a perturbative approach (RKKY) to solve it, Zaránd and Jankó show than $Ga_{1-x}Mn_xAs$ is a frustrated ferromagnet and behaves similarly to spin-glass materials. In this dissertation, the effect of spin-orbit coupling in the GaAs band structure along with the interaction between valance band holes and local Mn impurity spins in $Ga_{1-x}Mn_xAs$ are studied systematically using a mean field type approximation (DMFA). The attempt is to inspect the conclusion drawn by Zaránd and Jankó through the computation of the ferromagnetic phase transition temperature T_c for different concentrations of Mn impurities and valance band carrier concentrations, studying the charge carries (holes) spin polarization in the ferromagnetic regime and also obtaining a phase diagram for this material.

In all the abovementioned systems, electrons (or holes) share a common effect called *strong correlations.* The understanding of these correlations and developing clever methods to incorporate them in our calculations are of great importance in order to realistically describe the physics of these systems.

This dissertation concentrates on description, implementation and analysis of three approximation methods for strong correlations in great detail. It starts out with the *dynamical mean field approximation* (DMFA) which is a local mean filed approach incorporating only correlations in time space. Next, the *dynamical cluster approximation* (DCA) and the *cellular dynamical mean field theory* (CDMFT) will be introduced as systematic algorithms for adding real space nonlocal corrections to the DMFA. In the following chapters, the properties of these techniques will be elaborated upon and they will also be utilized to solve and study certain physical models. The DMFA will be employed in chapter 5 to systematically study ferromagnetism in $Ga_{1-x}Mn_xAs$ using a model proposed by Zaránd-Jankó. [10] Chapters 2 and 3 are both dedicated to the DCA, its most significant features and properties, its complementarity to the finite size lattice approach and also a unique prescription to implement it based on its microscopic theory. Chapter 4 makes a comparison between the DCA and the CDMFT in terms of their convergence schemes and addresses the advantages of each technique over the other.

1.2 The dynamical mean field approximation (DMFA)

The DMFA [12,13] is a self-consistent mean field theory on a single site of a lattice in which the correlations amongst electrons are dynamical only in time and fully local in space. In terms of Feynman diagrammatics, the DMFA can be derived in any dimension by relaxing the momentum conservation at the internal vertices of the self-energy diagrams [14]. However, this approximation becomes exact in the limit of infinite dimensions $D \to \infty$ (e.g., infinite number of nearest neighbors around a lattice site).

For a general Hamiltonian

$$H = H_0 + H_I \,, \tag{1.1}$$

where

$$H_0 = -t \sum_{\sigma} \sum_{<ij>} c^{\dagger}_{i\sigma} c_{j\sigma} \,, \tag{1.2}$$

and

$$H_I = \frac{1}{2} \sum_{jl,\sigma\sigma'} n_{j\sigma} n_{l\sigma'} V(R_j - R_l)\,, \tag{1.3}$$

(factors t and $V(R)$ correspond to nearest neighbor electron hopping integrals and electron-electron interactions respectively and $n_{j\sigma}$ and $n_{l\sigma'}$ are electron number operators) in order to obtain a finite density of states (DOS) in the infinite dimensional limit, the nearest neighbor electronic hopping integral should be renormalized as $t \sim D^{-1/2}$ [15]. Thus, the single particle Green function in real space $G(r) \sim t^r \sim D^{-r/2}$ which yields a fully local self-energy (and also vertex functions in case of two-body propagators) independent of momentum as $\Sigma(k,\omega) = \Sigma_{i,i}(\omega) + \mathcal{O}(1/\sqrt{D})$. The DMFA maps the lattice problem onto a self-consistently embedded impurity problem. Fig. 1.1 illustrates the algorithm as follows:

1. We start by making a guess for the local self-energy $\Sigma_{i,i}(\omega)$, usually zero.

2. We calculate the local lattice Green function $G_{i,i}(\omega) = 1/N \sum_k [G_0^{-1}(k,\omega) - \Sigma_{i,i}(\omega)]^{-1}$, where $G_0^{-1}(k,\omega) = \omega - \epsilon_k + \mu$ is the bare (non-interacting) lattice Green function with ϵ_k the non-interacting dispersion, μ the chemical potential and N is the number of lattice points.

3. We compute the cluster excluded Green function $\mathcal{G}(\omega)$ via $\mathcal{G}^{-1}(\omega) = G_{i,i}^{-1}(\omega) + \Sigma_{i,i}(\omega)$ in which the self-energy corresponding to the impurity site i is being excluded. $\mathcal{G}(\omega)$ is used as the bare Green function for the impurity problem.

4. The impurity problem is solved by employing some technique, e.g., the QMC(Quantum Monte Carlo) method or the CPA (Coherent Potential Approximation) yielding the impurity Green function G_{imp}.

5. The self-energy can be derived via $\Sigma_{i,i}(\omega) = \mathcal{G}^{-1}(\omega) - G_{imp}^{-1}(\omega)$ and used again in step (2) to continue the procedure. The cycle continues until $G_{i,i} = G_{imp}$ within the desired

accuracy. This procedure is fully causal, i.e., it preserves spectral weight and yields positive definite DOS.

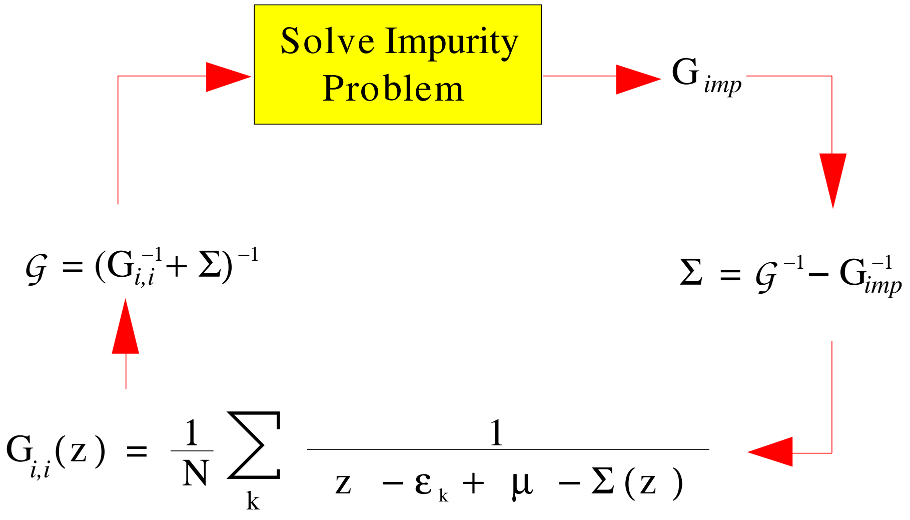

Figure 1.1: The DMFA algorithm.

As mentioned earlier, the DMFA is exact in infinite dimensions $D = \infty$. In finite dimensions, it is very difficult to add $1/D$ corrections to the DMFA causally and systematically at the same time. In addition, despite the capability of this technique to capture many of the key features of strongly correlated systems even at finite dimensions, due to the absence of non-local dynamical correlations, this method carries certain significant limitations. The non-local correlations in this approximation are crucial to describe non-local order parameters such as those in $d-$wave superconductivity. Even phases with local order parameters such as commensurate magnetism are greatly affected by non-local dynamical correlations (spin waves) suppressed in the DMFA [16]. Hence, our objective is to develop a systematic and causal procedure to incorporate these non-local correlations as a step towards the realistic physics of strongly correlated systems.

1.3 The dynamical cluster approximation (DCA)

The DCA is a self-consistent approach to include non-local corrections to the DMFA. In the DCA, the DMFA single impurity is replaced by a finite size cluster. This scheme is causal and systematic (but not in $1/D$). [2,16]

The DCA systematically restores the momentum conservation relinquished in the DMFA. In the DCA, the first Brillouin zone in the reciprocal space is divided into Nc equal cells of linear size Δk labeled by $\mathbf{K}$ in their centers, and the momenta within each cell are labeled by $\tilde{\mathbf{k}}$. Then $\mathbf{k} = \mathbf{K} + \tilde{\mathbf{k}}$ (c.f. Fig. 1.2). To visualize this scheme in the real lattice, one could consider tiling the lattice of N sites by N/N_c clusters each composed of $N_c = L^D$ sites where L is the linear size of the subcell and D is dimensionality (c.f. Fig. 1.2 for $L = 2$). We label the origin of the real lattice clusters by $\tilde{\mathbf{x}}$ and the N_c interacluster sites by $\mathbf{X}$. So for each site in the original lattice $\mathbf{x} = \mathbf{X} + \tilde{\mathbf{x}}$. This picture is similar to the block spin transformation for the Ising model in the Kadanoff renormalization group approach and will be employed in chapter 3 while discussing the microscopic theory of the DCA. However, one should note that the effective model of the DCA cannot be thought of N/N_c clusters composing the original lattice as this picture violates the translational invariance of the original lattice. Instead, it consists of N/N_c clusters composing the first Brillouin zone in the reciprocal lattice. Care must be taken when choosing the cluster geometries in order to preserve the lattice point group symmetry and also satisfy some other criteria for cubic or square lattices. [17]

The main assumption behind the DCA is that the irreducible self-energy $\Sigma^c(\mathbf{K}, \omega)$ and also the two-particle irreducible vertex functions of the cluster are good approximations to the irreducible self-energy and vertex functions of the real lattice within the cells around the cluster momenta. This assumption holds as long as the non-local correlations in the real space are short ranged with a cutoff $b < L/2$ (c.f. Fig. 1.2 for $L = 2$). Thus, according to the Nyquist sampling theorem, [18] we may only sample the reciprocal lattice in intervals of size $\Delta k = 2\pi/L$ on a set of $N_c = L^D$ points in the first Brillouin zone. Hence, as shown

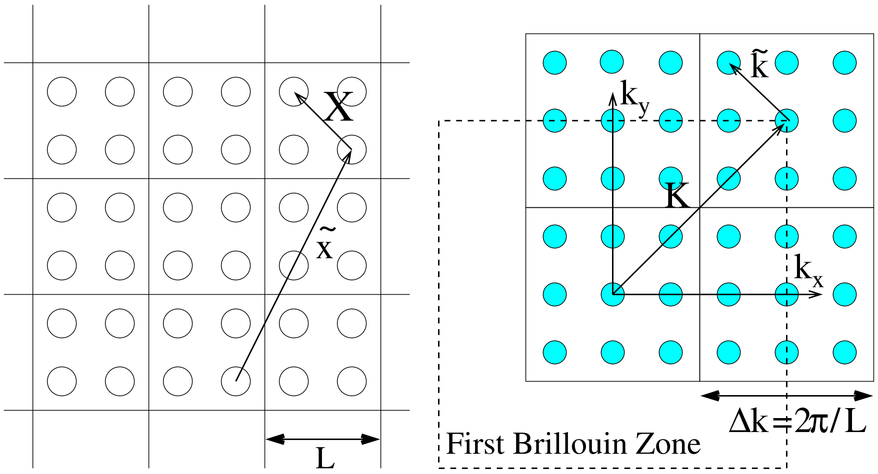

Figure 1.2: *The real lattice clusters (right) and (left) the first Brillouin zone divided into subcells.*

in Fig. 1.2, $\Sigma(\mathbf{K}+\tilde{\mathbf{k}},\omega)=\Sigma^c(\mathbf{K},\omega)$ for each $\tilde{\mathbf{k}}$ within a cell of size $(\pi/b)^2$ around $\mathbf{K}$. The vertex functions follow the same argument.

Both the DCA and the DMFA may also be derived by exploring the momentum conservation in the Feynman diagrammatics. As depicted in Fig. 1.3, momentum conservation at each vertex is described by the Laue function:

$$\Delta=\sum_{\mathbf{x}} e^{i\mathbf{x}\cdot(\mathbf{k}_1-\mathbf{q}-\mathbf{k}_2)}=N\delta_{\mathbf{k}_1,\mathbf{q}+\mathbf{k}_2}\,. \tag{1.4}$$

In the DMFA, momentum conservation at the internal vertices of irreducible Feynman diagrams is completely relinquished. I.e., the DMFA simply sets $\Delta=1$. [14] Hence, we may sum freely over all the internal momenta entering and leaving each vertex. Only local contributions survive the sum.

In the DCA, we first make the following separation in Eq. 1.4

$$\Delta=\sum_{\mathbf{x}} e^{i(\tilde{\mathbf{x}}+\mathbf{X})\cdot(\mathbf{K}_1-\mathbf{Q}-\mathbf{K}_2+\tilde{\mathbf{k}}_1-\tilde{\mathbf{q}}-\tilde{\mathbf{k}}_2)}\,. \tag{1.5}$$

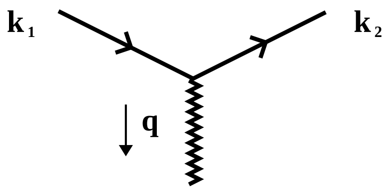

Figure 1.3: *A typical vertex in a Feynman diagram with solid lines as one particle Green functions and the wiggly line as an interaction.*

The products $\mathbf{K}_1 \cdot \tilde{\mathbf{x}}$, $\mathbf{Q} \cdot \tilde{\mathbf{x}}$ and $\mathbf{K}_2 \cdot \tilde{\mathbf{x}} = 2n\pi$ where n is an integer. Therefore, their associated phases may be neglected and Eq. 1.3 splits into two parts

$$\Delta = \frac{N}{N_c}\, \delta_{\tilde{\mathbf{k}}_1, \tilde{\mathbf{q}}+\tilde{\mathbf{k}}_2}\, N_c\, \delta_{\mathbf{K}_1, \mathbf{Q}+\mathbf{K}_2} \,. \tag{1.6}$$

The DCA also ignores the phases $e^{-i\tilde{\mathbf{k}}\cdot\tilde{\mathbf{x}}}$ due to the position of the cluster in the original lattice and (far less important) $e^{-i\tilde{\mathbf{k}}\cdot\mathbf{X}}$ corresponding to the position within the cluster. As a result, it approximates $N/N_c\, \delta_{\tilde{\mathbf{k}}_1, \tilde{\mathbf{q}}+\tilde{\mathbf{k}}_2} \cong 1$, so that

$$\Delta_{DCA} = N_c\, \delta_{\mathbf{K}_1, \mathbf{Q}+\mathbf{K}_2} \,, \tag{1.7}$$

which indicates that the momentum is conserved modulo Δk for transfers between the cells.

The approximation made through the substitution $\Delta \to \Delta_{DCA}$ corresponds to replacing all internal legs in the compact (skeletal) diagrams by the coarse-grained Green function $\bar{G}$ and interaction potential $\bar{V}$ defined by

$$\bar{G}(\mathbf{K}, \omega) = \frac{N_c}{N} \sum_{\tilde{\mathbf{k}}} G(\mathbf{K} + \tilde{\mathbf{k}}, \omega) \,, \tag{1.8}$$

$$\bar{V}(\mathbf{Q}) = \frac{N_c}{N} \sum_{\tilde{\mathbf{q}}} V(\mathbf{Q} + \tilde{\mathbf{q}}) \,. \tag{1.9}$$

In chapter 3, we will define the compact and non-compact diagrams and elaborately discuss why only the compact ones undergo the coarse-graining approximation.

Replacing Δ by Δ_{DCA} tremendously reduces the complexity of the problem because instead of having to perform sums over all N states in the entire first Brillouin zone, we have sums over only a set of N_c states where $N_c << N$.

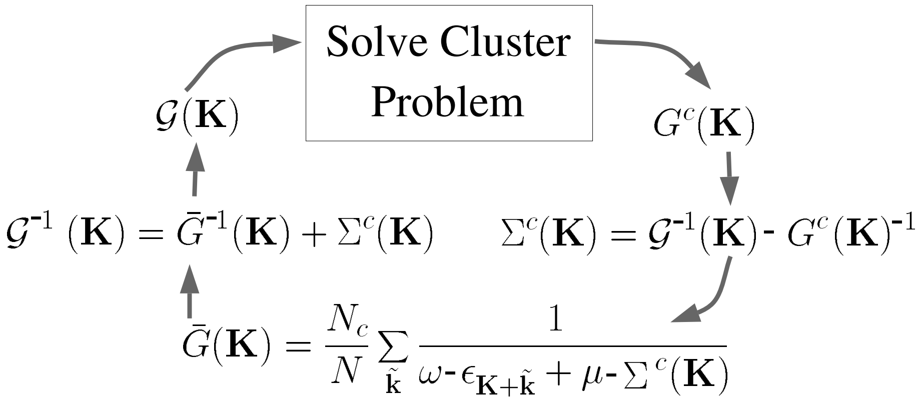

Figure 1.4: *The DCA algorithm.*

Similar to the DMFA, the DCA algortihm has been illustrated in Fig. 1.4. We start with the coarse-grained Green function

$$G^c(\mathbf{K},\omega) = \bar{G}(\mathbf{K},\omega) = \frac{N_c}{N}\sum_{\tilde{\mathbf{k}}} \frac{1}{\omega - \epsilon_{\mathbf{K}+\tilde{\mathbf{k}}} + \mu - \Sigma^c(\mathbf{K},\omega)}\,, \tag{1.10}$$

with a guess for the self-energy usually zero. The cluster-excluded Green function similar to the DMFA case can be calculated as

$$\mathcal{G}^{-1}(\mathbf{K},\omega) = \bar{G}^{-1}(\mathbf{K},\omega) + \Sigma^c(\mathbf{K},\omega)\,. \tag{1.11}$$

$\mathcal{G}(\mathbf{K},\omega)$ is used to solve the cluster problem by employing some technique including perturbation theory, QMC or the non-crossing approximation (if a compact diagram perturbation theory is used, the cluster exclusion step is skipped). The output of the cluster solver is either the fully dressed cluster Green function $G^c(\mathbf{K},\omega)$ or the cluster self-energy $\Sigma^c(\mathbf{K},\omega)$ depending whether the QMC, non-crossing approximation or a compact diagram perturbation approachs are being employed. For the QMC and non-crossing approximation, the cluster self-energy is simply computed by

$$\Sigma^c(\mathbf{K},\omega) = \mathcal{G}^{-1}(\mathbf{K},\omega) - \bar{G}^{-1}(\mathbf{K},\omega)\,, \tag{1.12}$$

and it is again used as an input to construct the dressed Green function shown in Fig. 1.4 and by coarse-graining the full Green function the loop is closed. Iterations will continue until $\bar{G}(\mathbf{K},\omega) = G^c(\mathbf{K},\omega)$ within the desired accuracy.

It should be mentioned that the coarse-grained Green function is only used to construct the one-particle irreducible and compact (two-particle irreducible) quantities such as the self-energy. The reducible and non-compact quantities such as the Green function must be constructed explicitly using the Dyson equation. In chapter 3, the concept of compact and non-compact quantities will be extensively elaborated upon and there will also be introduced the microscopic theory of the DCA as a systematic prescription for the implementation of the DCA.

1.4 The cellular dynamical mean field theory (CDMFT)

The CDMFT [19] is another self-consistent and causal technique to incorporate non-local correction in the DMFA. In the CDMFT the real lattice is divided into a series of identical molecules and the interactions between molecules are treated in a mean field approximation while the interactions within molecules are explicitly taken into account. (c.f. Fig. 1.2 on the left for $L = 2$)

Similar to the DCA, The CDMFT can be visualized in terms of relaxing momentum conservation at the internal vertices of compact Feynman diagrams illustrated in Fig. 1.3. [20]

Taking the Laue function in Eq. 1.4 and rewriting it in the form shown in Eq. 1.5, we only omit the phase factors $e^{i\tilde{\mathbf{k}}\cdot\tilde{\mathbf{x}}}$ resulting from the position of the molecule or cluster in the lattice but retain the phase factors $e^{i\tilde{\mathbf{k}}\cdot\mathbf{X}}$ corresponding to the position within clusters. As a result

$$\Delta_{CDT} = \sum_{\mathbf{X}} e^{i\mathbf{X}\cdot(\mathbf{K}_1-\mathbf{Q}-\mathbf{K}_2+\tilde{\mathbf{k}}_1-\tilde{\mathbf{q}}-\tilde{\mathbf{k}}_2)}\,. \tag{1.13}$$

The above choice for the Laue function in the CDMFT leads to the following coarse-graining scheme for the Green functions and interaction lines in Feynman diagrams

$$\begin{aligned}\bar{G}(\mathbf{X}_1,\mathbf{X}_2;\tilde{\mathbf{x}}=0) = \frac{1}{N^2}\sum_{\substack{\mathbf{K}_1,\mathbf{K}_2\\ \tilde{\mathbf{k}}_1,\tilde{\mathbf{k}}_2}} e^{i(\mathbf{K}_1+\tilde{\mathbf{k}}_1)\cdot\mathbf{X}_1} G(\mathbf{K}_1,\mathbf{K}_2;\tilde{\mathbf{k}}_1,\tilde{\mathbf{k}}_2) e^{-i(\mathbf{K}_2+\tilde{\mathbf{k}}_2)\cdot\mathbf{X}_2} = \\ \frac{{N_c}^2}{N^2}\sum_{\tilde{\mathbf{k}}_1,\tilde{\mathbf{k}}_2} G(\mathbf{X}_1,\mathbf{X}_2;\tilde{\mathbf{k}}_1,\tilde{\mathbf{k}}_2)\,.\end{aligned} \tag{1.14}$$

or in a matrix compact notation for cluster sites X_1 and X_2

$$\hat{\bar{G}} = \frac{N_c}{N}\sum_{\tilde{\mathbf{k}}} \hat{G}(\tilde{\mathbf{k}})\,. \tag{1.15}$$

(We have dropped the frequency label for simplicity) For the interaction lines as well

$$\begin{aligned}\bar{V}(\mathbf{X}_1,\mathbf{X}_2;\tilde{\mathbf{x}}=0) = \frac{1}{N^2}\sum_{\substack{\mathbf{K}_1,\mathbf{K}_2\\ \tilde{\mathbf{k}}_1,\tilde{\mathbf{k}}_2}} e^{i(\mathbf{K}_1+\tilde{\mathbf{k}}_1)\cdot\mathbf{X}_1} V(\mathbf{K}_1,\mathbf{K}_2;\tilde{\mathbf{k}}_1,\tilde{\mathbf{k}}_2) e^{-i(\mathbf{K}_2+\tilde{\mathbf{k}}_2)\cdot\mathbf{X}_2} = \\ \frac{{N_c}^2}{N^2}\sum_{\tilde{\mathbf{k}}_1,\tilde{\mathbf{k}}_2} V(\mathbf{X}_1,\mathbf{X}_2;\tilde{\mathbf{k}}_1,\tilde{\mathbf{k}}_2)\,.\end{aligned} \tag{1.16}$$

or in a matrix compact notation for cluster sites X_1 and X_2

$$\hat{\bar{V}} = \frac{N_c}{N}\sum_{\tilde{\mathbf{k}}} \hat{V}(\tilde{\mathbf{k}})\,. \tag{1.17}$$

The $\mathbf{X}$ summations of the cluster sites within each diagram are left to be performed. Both

$\hat{\bar{G}}$ and $\hat{\bar{V}}$ are truncated outside of the cluster. I.e., if the interaction V is non-local, $\hat{\bar{V}}$ will include only interactions within but not between clusters. Hence, the inclusion of the phase factors $e^{i\tilde{\mathbf{k}}\cdot\mathbf{X}}$ in the CDMFT Laue function leads to an approximation in the real space that violates the translational invariance of the original lattice. As a result, Green function propagators and interactions are functions of two cluster sites $\mathbf{X}_1$ and $\mathbf{X}_2$ in real space or two cluster momenta $\mathbf{K}_1$ and $\mathbf{K}_2$ in the reciprocal space.

The CDMFT algorithm is very similar to the one for the DCA. We start with a guess for the self-energy matrix $\hat{\Sigma}_{CDT}(\mathbf{X}_1, \mathbf{X}_2)$ usually zero. Then the Green function matrix is constructed as

$$\hat{G}(\tilde{\mathbf{k}}, \omega) = \left[\omega I - \hat{\epsilon}(\tilde{\mathbf{k}}) - \hat{\Sigma}_{CDT}(\omega)\right]^{-1}, \tag{1.18}$$

with

$$[\hat{\epsilon}(\tilde{\mathbf{k}})]_{\mathbf{X}_1,\mathbf{X}_2} = \epsilon(\mathbf{X}_1 - \mathbf{X}_2, \tilde{\mathbf{k}}) = \frac{1}{N_c}\sum_{\mathbf{K}} e^{i(\mathbf{K}+\tilde{\mathbf{k}})\cdot(\mathbf{X}_1-\mathbf{X}_2)}\epsilon_{\mathbf{K}+\tilde{\mathbf{k}}}, \tag{1.19}$$

being the Fourier transform of the dispersion for cluster sites $\mathbf{X}_1$ and $\mathbf{X}_2$. This matrix is coarse-grained over all $\tilde{\mathbf{k}}$ values and just as it was the case for the DCA, the cluster excluded Green function $\hat{\mathcal{G}}$ is calculated via $\hat{\mathcal{G}}^{-1}(\tilde{\mathbf{k}}, \omega) = \hat{\bar{G}}^{-1}(\tilde{\mathbf{k}}, \omega) + \hat{\Sigma}_{CDT}(\omega)$. The cluster excluded Green function is employed as an input to the cluster solver (If a compact diagram perturbation approach is used, the cluster exclusion step can be skipped). The output of the cluster solver is the fully dressed cluster Green function. We again calculate the self-energy via $\hat{\Sigma}_{CDT}(\omega) = \hat{\mathcal{G}}^{-1}(\tilde{\mathbf{k}}, \omega) - \hat{G^c}^{-1}(\tilde{\mathbf{k}}, \omega)$ and use it to compute the $\hat{\bar{G}}$ for the next iteration. Iterations will continue until $\hat{\bar{G}} = \hat{G}^c$ within the desired accuracy. Fig. 1.5 illustrates the algorithm

To differentiate between the DCA and CDMFT, we rewrite Green functions in both these two schemes in terms of a hybridization host-function Γ corresponding to the coupling of the cluster to its mean field host. We start by splitting the hopping integral t defined in Ref. 2.2 into an inter- and intracluster part. For the CDMFT, the intercluster hopping

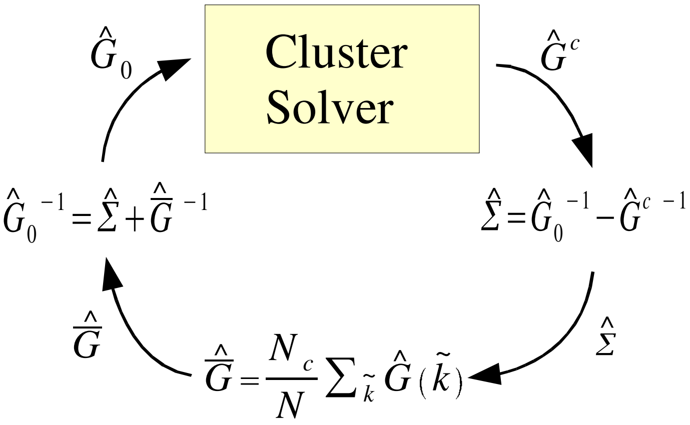

Figure 1.5: The CDMFT algorithm.

$[\hat{T}_{CDT}]_{X_1,X_2} = \hat{T}_{CDT}(\tilde{\mathbf{k}}) = \hat{\epsilon}(\tilde{\mathbf{k}}) - \hat{\epsilon}_0$ and reads in the real space

$$\hat{T}_{CDT}(\tilde{\mathbf{x}}) = \hat{t}(\tilde{\mathbf{x}}) - \hat{\epsilon}_0 \delta(\tilde{\mathbf{x}})\,, \tag{1.20}$$

where $\hat{\epsilon}_0 = N_c/N \sum_{\tilde{\mathbf{k}}} \hat{\epsilon}(\tilde{\mathbf{k}}) = \hat{t}(\tilde{\mathbf{x}} = 0)$. Thus, $\hat{T}_{CDT}$ is only non-zero for $\tilde{\mathbf{x}} \neq 0$ and therefore has non-vanishing matrix elements only for the sites on the boundary of the cluster. For the DCA, the intercluster hopping integral is defined as $\hat{T}_{DCA}(\mathbf{K}, \tilde{\mathbf{k}}) = \hat{\epsilon}(\mathbf{K}, \tilde{\mathbf{k}}) - \bar{\epsilon}_{\mathbf{K}}$ and can be written in real space as

$$\hat{T}_{DCA}(\tilde{\mathbf{x}}) = \hat{t}(\tilde{\mathbf{x}}) - \hat{\bar{\epsilon}}\hat{\delta}^c(\tilde{\mathbf{x}})\,, \tag{1.21}$$

where $[\hat{t}]_{\mathbf{X}_1,\mathbf{X}_2} = \bar{t}(\mathbf{X}_1 - \mathbf{X}_2) = 1/N_c \sum_{\mathbf{K}} e^{i\mathbf{K}\cdot(\mathbf{X}_1 - \mathbf{X}_2)} \bar{\epsilon}_{\mathbf{K}}$ and the cluster delta like function $[\hat{\delta}^c(\tilde{\mathbf{x}})]_{\mathbf{X}_1,\mathbf{X}_2} = \hat{\delta}^c(\mathbf{X}_1 - \mathbf{X}_2, \tilde{\mathbf{x}}) = N_c/N \sum_{\tilde{\mathbf{k}}} e^{i\tilde{\mathbf{k}}\cdot(\mathbf{X}_1 - \mathbf{X}_2 + \tilde{\mathbf{x}})}$. It can be shown that $\hat{\delta}^c(\mathbf{X}_1 - \mathbf{X}_2, \tilde{\mathbf{x}}) \approx 1$ for $\tilde{\mathbf{x}} = 0$ and falls off rapidly for finite $\tilde{\mathbf{x}}$. It follows that $\bar{t}(\mathbf{X}_1 - \mathbf{X}_2) = \bar{t}(\mathbf{X}_1 - \mathbf{X}_2, \tilde{\mathbf{x}} = 0)$ for $N_c = N$, but $|\bar{t}(\mathbf{X}_1 - \mathbf{X}_2)| < |\bar{t}(\mathbf{X}_1 - \mathbf{X}_2, \tilde{\mathbf{x}} = 0)|$ for $N_c < N$ and therefore, the DCA intercluster hopping $T_{DCA}(\mathbf{X}_1 - \mathbf{X}_2, \tilde{\mathbf{x}})$ is even finite for $\tilde{\mathbf{x}} = 0$ i.e., between sites belonging to the same cluster when $N_c < N$ but is significantly reduced compared to $\tilde{\mathbf{x}} \neq 0$. This is due to the periodicity of the DCA cluster. Hence, as mentioned earlier, the effective model of the DCA can not be thought of N/N_c clusters composing the original lattice. Rather, it can be viewed as a renormalized model in real space.

To define the hybridization function Γ, we first define the CDMFT Green function matrix as

$$\hat{g}(z) = [zI - \hat{\epsilon}_0 - \hat{\Sigma}_{CDT}(z)]^{-1}\,, \tag{1.22}$$

that is localize on the impurity cluster. Using this definition, Eq. 1.15 reads

$$\hat{\bar{G}} = \frac{N_c}{N}\sum_{\tilde{\mathbf{k}}} \hat{G}(\tilde{\mathbf{k}}) = [\hat{g}^{-1} - \hat{\Gamma}_{CDT}]^{-1}\,, \tag{1.23}$$

and Eq. 1.18 can be rewritten as

$$\hat{G}(\tilde{\mathbf{k}}) = \hat{g} + \hat{g}\ \hat{T}_{CDT}(\tilde{\mathbf{k}})\ \hat{G}(\tilde{\mathbf{k}})\,. \tag{1.24}$$

By inserting Eq. 1.24 into Eq. 1.23 and invoking $\sum_{\tilde{\mathbf{k}}} \hat{T}_{CDT}(\tilde{\mathbf{k}}) = 0$, after some algebra, we arrive at the following expression for the CDMFT hybridization function

$$\hat{\Gamma}_{CDT} = \left[I + \frac{N_c}{N}\sum_{\tilde{\mathbf{k}}} \hat{T}_{CDT}(\tilde{\mathbf{k}})\hat{G}(\tilde{\mathbf{k}})\right]^{-1} \frac{N_c}{N}\sum_{\tilde{\mathbf{k}}} \hat{T}_{CDT}(\tilde{\mathbf{k}})\hat{G}(\tilde{\mathbf{k}})\hat{T}_{CDT}(\tilde{\mathbf{k}})\,. \tag{1.25}$$

$\hat{\Gamma}_{CDT}$ is finite only for sites on the boundary of the cluster and vanishes for sites inside the clusters. This is because $\hat{T}_{CDT}$ has only non-vanishing matrix elements between the sites sitting on the boundary. Hence, the average hybridization strength per site for the CDMFT cluster is

$$\hat{\bar{\Gamma}}_{CDT} = \frac{1}{N_c}\sum_{\mathbf{X}_1,\mathbf{X}_2} \hat{\Gamma}_{CDT}(\mathbf{X}_1,\mathbf{X}_2) \sim \mathcal{O}\Big(\frac{2D}{L_c}\Big)\,, \tag{1.26}$$

since only the sites on the boundary of the cluster $\propto 2D \cdot {L_c}^{D-1}$ contribute and $N_c = {L_c}^D$.

For the DCA, by following the same procedure as we did for the CDMFT and taking into account that $\Gamma_{DCA}(\mathbf{K})$ is a diagonal matrix in $\mathbf{K}$, the hybridization function becomes

$$\Gamma_{DCA}(\mathbf{K}) = \frac{\frac{N_c}{N}\sum_{\tilde{\mathbf{k}}} T^2{}_{DCA}(\mathbf{K}, \tilde{\mathbf{k}})G(\mathbf{K}, \tilde{\mathbf{k}})}{1 + \frac{N_c}{N}\sum_{\tilde{\mathbf{k}}} T_{DCA}(\mathbf{K}, \tilde{\mathbf{k}})G(\mathbf{K}, \tilde{\mathbf{k}})} \,. \tag{1.27}$$

The momenta $\tilde{\mathbf{k}}$ are restricted to the DCA coarse-graining cell and therefore in the order of $\Delta k \propto 1/L_c$. Knowing that, $\epsilon(\mathbf{K}) - \bar{\epsilon}_{\mathbf{K}} \sim \mathcal{O}((\Delta k)^2)$, by performing a Taylor series expansion on $T_{DCA}(\mathbf{K}, \tilde{\mathbf{k}})$ around $\epsilon(\mathbf{K})$ we find that $T_{DCA}(\mathbf{K}, \tilde{\mathbf{k}}) \sim \mathcal{O}(1/L_c)$. After some algebra we find

$$\bar{\Gamma}_{DCA} = \frac{1}{N_c}\sum_{\mathbf{K}} \Gamma_{DCA}(\mathbf{K}) \sim \mathcal{O}(1/{L_c}^2) \,. \tag{1.28}$$

Using Eq. 1.25 and Eq. 1.27 we can redefine the coarse-grained Green functions for both the DCA and CDMFT as follows

$$\hat{\bar{G}}(z) = [zI - \hat{\epsilon}_0 - \hat{\Sigma}_{CDT}(z) - \hat{\Gamma}_{CDT}(z)]^{-1} \,, \tag{1.29}$$

$$\bar{G}(\mathbf{K}, z) = [z - \bar{\epsilon}_{\mathbf{K}} - \Sigma_{DCA}(\mathbf{K}, z) - \Gamma_{DCA}(\mathbf{K}, z)]^{-1} \,. \tag{1.30}$$

In both the DCA and CDMFT, $\bar{\Gamma}$ acts as a small parameter. Hence, the approximations implemented by the DCA and CDMFT are equivalent to replacing their Green functions by their coarse-grained counter parts $\bar{G}(\mathbf{K})$ and $\hat{\bar{G}}$ in diagrams for the self-energy. After performing all the summations over $\tilde{\mathbf{k}}$, terms of lower order in $1/L_c$ than Γ vanish. Thus, the DCA is an approximation with corrections of order $\bar{\Gamma} \sim \mathcal{O}(1/L^2{}_c)$ while the CDMFT corrections are of order $\bar{\Gamma} \sim \mathcal{O}(1/L_c)$. chapter 4 is dedicated to a more elaborate comparison of these two techniques.

1.5 Outline of dissertation

This dissertation consists of six chapters as follows:

In chapter 2, the DCA is employed in conjunction with the Fluctuation Exchange Approximation (FLEX) to study the Hubbard model. FLEX is a perturbative diagrammatic approach in which classes of Feynman diagrams are summed over analytically using geometric series. The FLEX is used as a tool to investigate the complementarity of the DCA and the finite size lattice technique with periodic boundary conditions by comparing their results for the Hubbard model. The significant advantages of the DCA implementation in momentum space suggests the development of the same formalism for the frequency space. However, it will be shown that such a formalism for Matsubara frequencies at finite temperatures leads to acausal results and is not viable. However, a real frequency approach is shown to be feasible.

In chapter 3, a central approximation of DCA by example of the Hubbard model will be examined. Both compact (skeletal) and non-compact contributions to the thermodynamic potential are studied using analytical and numerical means. One finds that approximating non-compact diagrams by their cluster analogs results in a larger systematic error as compared to the compact diagrams. Consequently, only the compact contributions should be taken from the cluster, whereas non-compact graphs should be inferred from the appropriate Dyson equation. The distinction between non-compact and compact diagrams persists even in the limit of infinite dimensions. Non-local corrections beyond the DCA exist for the non-compact diagrams, whereas they vanish for compact diagrams. There will also be proposed a microscopic theory underlying the DCA in terms of the Green function's exponential falloff as a function of distance in real space. This approach is independent of a specific model and ties the derivation of the DCA to the original derivation of the DMFA in the limit of infinite dimensions. [15]

In chapter 4 a toy model called *the simplified one-dimensional large-N model*, first introduced and studied by I. Affleck *et al.* [21], is employed to demonstrate the convergence comparison between the DCA and CDMFT. This model has a mean filed solution which becomes exact as one approaches the thermodynamic limit. As shown earlier, [20, 22] due to the periodic (open) boundary conditions, the DCA (CDMFT) converges with corrections of $\mathcal{O}(1/L_c^2)$ ($\mathcal{O}(1/L_c)$) with L_c the linear size of the cluster. Hence, for large enough L_c, one would expect the DCA to converge more quickly than the CDMFT to the exact results. Studying the convergence of the DCA and CDMFT towards the exact results for this model concludes that for large enough cluster sizes the DCA converges much faster than the CDMFT. The DCA also requires much less CPU time than the CDMFT for large L_c calculations.

In chapter 5, a DMFA approach is employed to study ferromagnetism in $\mathrm{Ga}_{1-x}\mathrm{Mn}_x\mathrm{As}$ using a simplified Kohn-Luttinger Hamiltonian proposed by Zaránd-Jankó. [10] In this Hamiltonian, the spin-orbit coupling effect in the band structure of pure GaAs along with the interaction between Mn impurity spins and the spins of valance band holes are taken into account. This approach is the first systematic analysis to this two-band model for holes corresponding to the total spin of $J = 3/2$ and $J_z = \pm 3/2$ and $\pm 1/2$ respectively. Holes spins are quantized along the direction of their momenta (chiral basis) in order for the dispersion to have a simple diagonal form. Mn impurity spins $S = 5/2$ and are treated classically. The Green function is self-consistently computed using the DMFT while averaging over all possible orientations and configurations of the Mn impurity spins. The objective is to calculate the ferromagnetic phase transition temperature T_c by calculating the magnetization versus temperature for different concentrations of Mn impurities and valance band carrier concentrations. Also the holes spin polarization and magnetic phase diagram for $\mathrm{Ga}_{1-x}\mathrm{Mn}_x\mathrm{As}$ are studied in this chapter. Results will be compared with those obtained earlier via a perturbation approach in Ref. [10] and also experiments [23] as an inspection for conclusions derived by Zaránd-Jankó in Ref. [10]. Finally, chapter 6, summarizes the achievements in each chapter and outlines possible developments in the future.

Chapter 2

The dynamical cluster approximation employing the fluctuation exchange approximation as cluster solver

2.1 Introduction

Non-local correlations play an important role in the physics of strongly correlated electron systems such as high-Tc superconductors, heavy fermion metals, etc. The Dynamical Mean Field Approximation (DMFA), [13] in which all the non-local correlations are ignored, can capture some of the major features of strongly correlated systems. Nevertheless, the non-local correlations become crucial in the physics of phases with non-local order parameters such as d-wave superconductivity. Even phases with local order parameters such as commensurate magnetism can be significantly affected by the non-local correlations (e.g. spin waves) ignored in the DMFA.

The early attempts to extend the DMFA by including non-local correlations resulted in the violation of causality which is a requirement for positive definiteness of the spectral weight and the density of states (DOS). [24] The Dynamical Cluster Approximation (DCA) is a fully causal technique used to systematically add nonlocal corrections to the DMFA by mapping the lattice onto a self-consistently embedded cluster problem. The mapping from the lattice to the cluster is accompanied by coarse-graining the lattice problem in its reciprocal space. Thus far, the DCA has been combined with Quantum Monte Carlo (QMC) [16,25], the Non-Crossing Approximation (NCA) [26] and the Fluctuation Exchange Approximation (FLEX) [2,3,27] to solve the corresponding cluster problems.

The FLEX is a perturbative diagrammatic approach in which classes of Feynman diagrams are summed to all orders using geometric series. [28,29] Others [1,30] have employed the FLEX for finite size lattices with periodic boundary conditions. Due to the absence of contributions from some relevant diagrams, the FLEX is not capable of addressing the Hubbard model physics in the strong regime precisely. However, the main objective of this work is to make a comparison between the DCA-FLEX combination results and previous finite size lattice FLEX calculations. It is hoped that this study will lead to a better understanding of the DCA.

In this work we also consider the extension of the DCA to frequency space. The many-body theory at finite temperatures is conventionally derived in terms of discrete imaginary Matsubara frequencies. We illustrate that even for a self-consistent algorithm like the FLEX, coarse-graining the imaginary frequency propagators results in causality violations and can not be implemented. However, a real frequency formalism is shown to be causal and applicable not only to the FLEX, but also to other cluster solving methods such as the NCA.

This chapter is structured as follows. In the next three sections, we briefly review the DCA application to the Hubbard model, the FLEX, and then we describe how the FLEX and the DCA may be merged into a single algorithm. In the next three sections, we use the FLEX-DCA, in comparison to the FLEX for finite-sized systems, to explore the properties of the DCA. The last section, is devoted to an extension of the DCA to frequency space.

2.2 Hubbard Model

We will apply the DCA to study the Hubbard model Hamiltonian incorporating interactions between the electrons on a lattice. It includes a tight-binding part due to the hopping of electrons among the sites and an interaction between the electrons. The general Hamiltonian reads

$$H = H_0 + H_I \,, \tag{2.1}$$

where

$$H_0 = -t \sum_{\sigma} \sum_{<ij>} c^{\dagger}_{i\sigma} c_{j\sigma} \,, \tag{2.2}$$

and

$$\begin{aligned} H_I &= \frac{1}{2} \sum_{jl,\sigma\sigma'} n_{j\sigma} n_{l\sigma'} V(R_j - R_l) \\ V(R) &\approx \frac{e^2}{R} \,. \end{aligned} \tag{2.3}$$

Factors t and $V(R)$ correspond to electron hoppings and Coulomb interactions respectively. Later in this chapter, we will study the simplest Hubbard interaction which is fully local and only between electrons sitting at the same site having opposite spin directions. The interaction strength is a constant called U. Hence, for the local model, Eq. 2.3 simplifies to

$$H_I = U \sum_i n_{i\uparrow} n_{i\downarrow} \,. \tag{2.4}$$

In terms of the vertex properties (addressed in section 1.3), since the interaction is local and therefore independent of $\mathbf{q}$, we may sum freely over the $\mathbf{q}$ momentum for a pair of Laue functions in Eq. 1.3 sharing a common interaction wiggly line as depicted in Fig. 1.3. As a result, the corresponding Laue function will become

$$\Delta = \frac{1}{N}\sum_{\mathbf{q}}\sum_{\mathbf{x}} e^{i\mathbf{x}\cdot(\mathbf{k}_1-\mathbf{q}-\mathbf{k}_2)}\sum_{\mathbf{y}} e^{i\mathbf{y}\cdot(\mathbf{k}_3+\mathbf{q}-\mathbf{k}_4)} = \\ N\sum_{\mathbf{q}}\delta_{\mathbf{k}_1,\mathbf{q}+\mathbf{k}_2}\ \delta_{\mathbf{k}_3+\mathbf{q},\mathbf{k}_4} = N\delta_{\mathbf{k}_1+\mathbf{k}_3,\mathbf{k}_2+\mathbf{k}_4}\,, \tag{2.5}$$

and analogously for the DCA, by summing freely over $\mathbf{Q}$

$$\Delta_{DCA} = N_c\ \delta_{\mathbf{K}_1+\mathbf{K}_3,\mathbf{K}_2+\mathbf{K}_4}\,. \tag{2.6}$$

2.3 Fluctuation Exchange Approximation (FLEX)

In the Feynman diagrammatics of the Hubbard model with a local interaction, all the interactions (wiggly lines in Fig. 2.1) contribute a c-number U from Eq. 2.4. The electronic Green functions (solid lines) which interact with one another should have opposite spins. Considering these restrictions, had we been able to include all the possible diagrams in our expansion we would have solved the problem exactly. However, in practice this is not feasible.

The Fluctuation Exchange Approximation (FLEX) was introduced as an approximate technique to simplify this diagrammatic sum [28, 29], while retaining a conserving approximation. In the FLEX, the interaction part of the Hubbard model Hamiltonian is treated perturbatively by selecting a certain class of all the possible diagrams which may be summed as a geometric series. Following Baym [31], we define the generating functional $\Phi[G(k,\omega_n)]$ as the collection of all the selected families of diagrams illustrated in Fig. 2.1. Therefore, $\Phi[G(k,\omega_n)]$ for the FLEX can be written

$$\Phi = \Phi^{df}_{ph} + \Phi^{sf}_{ph} + \Phi_{pp}\,, \tag{2.7}$$

$$\Phi^{df}_{ph} = -\frac{1}{2}\,\mathrm{Tr}\,[\chi_{\mathrm{ph}}]^2 + \frac{1}{2}\,\mathrm{Tr}\,[\ln(1+\chi_{\mathrm{ph}}) - \chi_{\mathrm{ph}} + \frac{1}{2}{\chi^2}_{\mathrm{ph}}]\,, \tag{2.8}$$

$$\Phi_{ph}^{sf} = \frac{3}{2}\,\mathrm{Tr}\left[\ln(1-\chi_{\mathrm{ph}}) + \chi_{\mathrm{ph}} + \frac{1}{2}{\chi^2}_{\mathrm{ph}}\right], \tag{2.9}$$

$$\Phi_{pp} = \mathrm{Tr}\left[\ln(1+\chi_{\mathrm{pp}}) - \chi_{\mathrm{pp}} + \frac{1}{2}{\chi^2}_{\mathrm{pp}}\right], \tag{2.10}$$

where $\mathrm{Tr} = (T/N)\sum_k \sum_n$ with T the temperature and N the number of lattice sites. The particle-hole and particle-particle susceptibility bubbles are

$$\chi_{pp}(q,\omega_n) = U(T/N)\sum_k \sum_m G(k+q,\omega_n+\omega_m)G(-k,-\omega_m)\,, \tag{2.11}$$

$$\chi_{ph}(q,\omega_n) = -U(T/N)\sum_k \sum_m G(k+q,\omega_n+\omega_m)G(k,\omega_m)\,. \tag{2.12}$$

The self-energy and the Green function are defined by

$$\Sigma(k,\omega_n) = \frac{1}{2}\frac{\delta\Phi[G]}{\delta G(k,\omega_n)}\,, \tag{2.13}$$

$$G(k,\omega_n) = [G^{(0)-1}(k,\omega_n) - \Sigma(k,\omega_n)]^{-1}\,, \tag{2.14}$$

where $G^{(0)}$ is the non-interacting one particle Green function defined by

$$G^{(0)}(k,\omega_n) = \frac{1}{i\omega_n - \epsilon_{\mathbf{k}} + \mu}\,, \tag{2.15}$$

with $\epsilon_{\mathbf{k}}$ the non-interacting Hubbard model dispersion and μ the chemical potential.

Calculating the self-energy for Eq. 2.7 using Eq. 2.13 we get

$$\begin{aligned}\Sigma(k,\omega_n) = U(T/N)\sum_q \sum_m [V^{(ph)}(q,\omega_m)G(k-q,\omega_n-\omega_m) - V^{(pp)}(q,\omega_m) \times \\ G(-k+q,-\omega_n+\omega_m)]\,,\end{aligned} \tag{2.16}$$

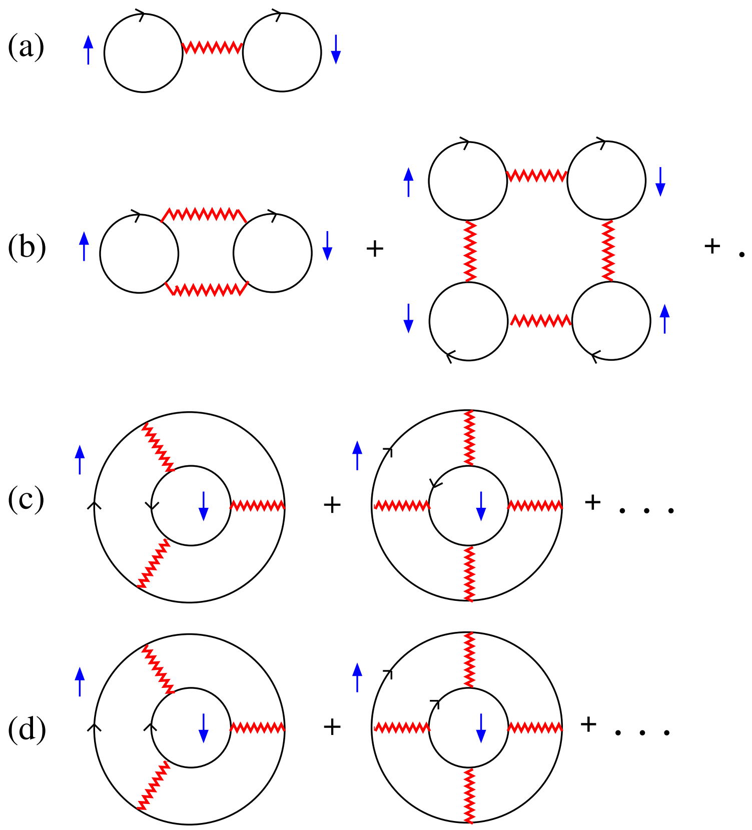

Figure 2.1: *(a) Lowest order diagram (Hartree term), (b) longitudinal spin and density fluctuation Φ diagrams with an even number of bubbles (Φ_{ph}^{df}), (c) transverse spin fluctuations (Φ_{ph}^{sf}) and (d) particle-particle fluctuations (Φ_{pp}).*

in which

$$V^{(ph)}(q,\omega_m) = \chi_{ph}(q,\omega_m) + \frac{1}{2}\chi_{ph}(q,\omega_m)[\frac{1}{1+\chi_{ph}(q,\omega_m)} - 1] + \frac{3}{2}\chi_{ph}(q,\omega_m)) \times [\frac{1}{1-\chi_{ph}(q,\omega_m)} - 1]\,, \tag{2.17}$$

$$V^{(pp)}(q,\omega_m) = \chi_{pp}(q,\omega_m)[\frac{1}{1+\chi_{pp}(q,\omega_m)} - 1]\,. \tag{2.18}$$

Eq. 2.17,2.18 for the potential functions $V^{(ph)}$ and $V^{(pp)}$ are geometric series for χ_{ph} and χ_{pp}

similar to the *random phase approximation* (RPA) results. The Hartree term contribution to the self-energy has not explicitly appeared in Eq. 2.16 as it is constant and can be always embedded in the chemical potential in Eq. 2.15.

The difference $\Delta\Omega(T,\mu)$ between interacting and non-interacting thermodynamic potential functional is also expressible in terms of the Green functions, self-energy, and $\Phi[G]$

$$\Delta\Omega(T,\mu) = \Omega - \Omega_0 = -2\mathrm{Tr}[\Sigma G - \ln(G/G_0)] + \Phi[G]\,. \tag{2.19}$$

In the FLEX, since we include only a limited set of all the diagrammatic contributions, we do not anticipate to precisely address the Hubbard model physics. However, there are a number of significant physical features such as anti-ferromagnetic order at half filling and low temperatures that this approximation is able to capture. Moreover, by using the FLEX both together with the DCA and to study finite sized systems with periodic boundary conditions, we can study the differences between these approaches. For example, as we will shortly illustrate, the complementarity of the DCA and finite size lattice techniques is manifest in the FLEX. The FLEX can also be invoked as a good test for the microscopic theory of the DCA and the coarse-graining effects in the compact and non-compact diagrams for Eq. 3.1.

2.4 The Combination of the FLEX and DCA (Algorithm)

In the combination of the FLEX and DCA, our goal is to calculate the self-energy in Eq. 2.13 whereby we construct the dressed Green function for the lattice as a building block for all the relevant physical quantities. We start out with the bare (non-interacting) Green function $G^{(0)}(\mathbf{k},z)$ defined in Eq. 2.15 with z the Matsubara frequency (complex). We coarse-grain G as directed in Eq. 3.5 and calculate the self-energy using Eq. 2.13. This is used to recompute

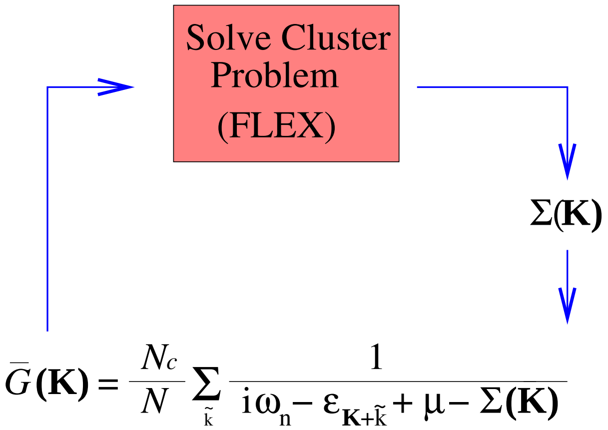

Figure 2.2: The FLEX-DCA numerical algorithm. The dressed G is solved self-consistently with Σ. The iteration process stops whenever convergence is achieved.

the dressed Green function

$$G(\mathbf{k}, z) = \frac{1}{z - \epsilon_{\mathbf{k}} + \mu - \Sigma_{DCA}(\mathbf{K}, z)}\,. \tag{2.20}$$

where the index DCA in $\Sigma_{DCA}(\mathbf{K}, z)$ indicates that we have used coarse-grained $\bar{G}$ for the construction of self-energy. The new G is coarse-grained and used to calculate a new estimate of $\Sigma_{DCA}(\mathbf{K}, z)$. We repeat this process iteratively until convergence at a desired tolerance is obtained. The final self-energy is used to construct the dressed Green function in Eq. 3.6, required to compute the physical quantities such as spectral function, the density of states (DOS), etc. The algorithm of this calculation is demonstrated in Fig 2.2.

2.5 Complementarity of the DCA to the Finite Size Lattice Approximation with periodic boundary conditions

In the half-filled Hubbard model, the antiferromagnetic correlation length ξ increases with decreasing temperature and diverges at the phase transition. In a finite size lattice with periodic boundary conditions, as the temperature drops, once the correlation length reaches the size of the lattice, the system is fully frozen and there is a gap to excitations (c.f. Fig 2.3.a). In contrast, in the DCA, the correlations are confined within clusters of size $N_c << N$ (the size of the entire lattice) and they never reach the size of the lattice. As we lower the temperature, the correlation length approaches the size of the cluster but since the lattice remains in the thermodynamic limit, it never freezes (c.f. Fig 2.3.b). By increasing the size of clusters in the DCA, we take longer ranged correlations into account so the gap will become more pronounced. Consequently, correlation induced gaps are generally overestimated in the finite size lattice, while in the DCA they are underestimated. This complementary behavior may be seen in $G(k, \tau)$, with $k = (0, \pi)$ computed using finite size lattices with periodic boundary conditions and the DCA. As illustrated in Fig. 2.4, by increasing the size of the finite size lattice and the DCA cluster, the Green functions converge from opposite directions. In the finite size lattice, the Green function (e.g. at $\tau = \beta/2$) decreases with the increase of size which is consistent with overestimating the gap; while in the DCA, the Green function increases as the cluster size grows consistent with underestimating the gap. It is also observed that the convergence in the DCA is much faster, meaning that the result of the DCA is closer to the true curve at a given cluster size. Both finite size lattices with periodic boundary conditions and the DCA converge with corrections of $\mathcal{O}(\lambda/L^2)$ with L the linear size of the finite lattice or the DCA cluster and λ a coefficient. [20, 22] The faster convergence of the DCA corresponds to its smaller λ

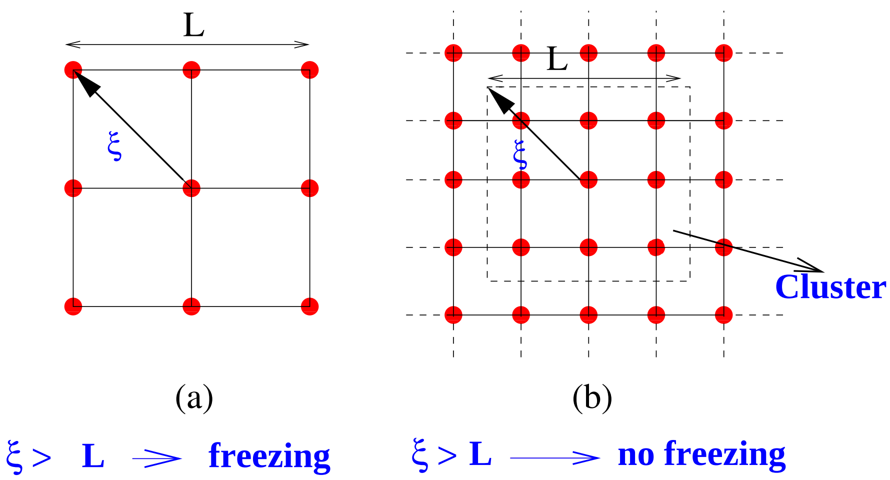

Figure 2.3: (a) The finite size lattice with periodic boundary conditions, size L and correlation length ξ and (b) the lattice with clusters of size L and the correlation length ξ.

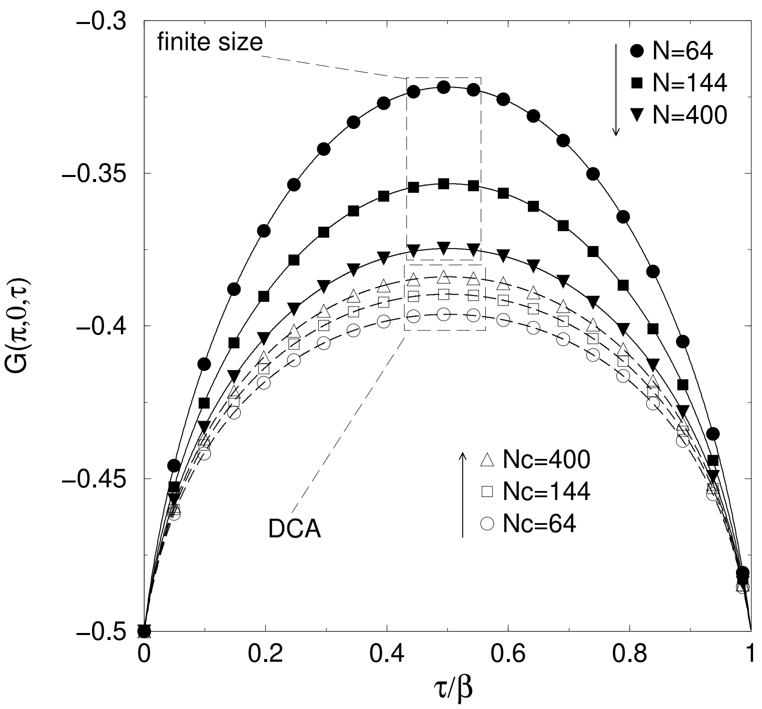

Figure 2.4: The Green function $G(k = (0, \pi), \tau)$ at $T = 0.10$ and $U/t = 1.57$ versus imaginary time τ/β ($\beta = 1/T$). Finite size results (filled symbols) and DCA results (open symbols) are displayed for lattice sizes of $N = 8 \times 8$, 12×12, and 20×20. The curves show the complementary approach of the two methods to the thermodynamic limit.

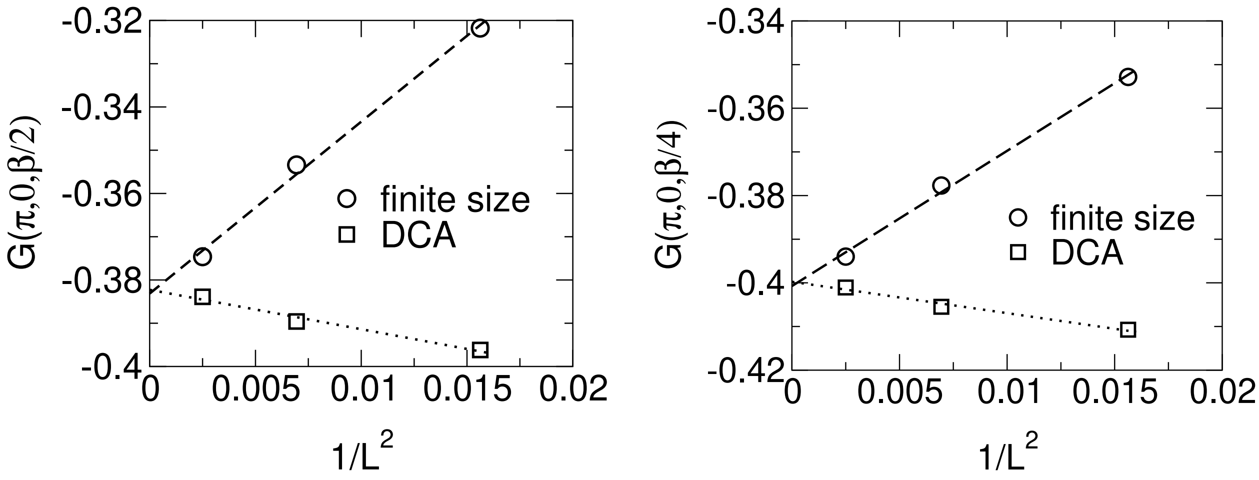

Figure 2.5: The Green function $G(k = (0, \pi), \tau)$ at $\tau = \beta/2$ (left) and $\tau = \beta/4$) (right) versus $1/L^2$ for the DCA and finite size results in Fig. 2.4. The linear extrapolations meet at a point representing the thermodynamic limit of the Green function of the Hubbard model evaluated within FLEX.

compared to finite size lattices. In Fig. 2.5, the values of the $G(k = (0, \pi), \tau = \beta/2)$ and $G(k = (0, \pi), \tau = \beta/4$ in Fig. 2.4 have been plotted versus $1/L^2$ for both the DCA and finite size results. The Green function behaves linearly as a function of $1/L^2$ for large L. The extrapolations of the DCA and finite size results meet as $L \to \infty$, approximating the value of the dressed Green function in the thermodynamic limit. The complementarity of DCA and finite size methods allows a determination of the thermodynamic limit of imaginary time Green functions with unprecedented accuracy.

2.6 Finite size versus the DCA FLEX results for the two dimensional Hubbard Model at half-filling

The Hubbard model at half filling undergoes a phase transition to anti-ferromagnetic order at low temperatures. According to the Mermin-Wagner-Hohenberg theorem, for dimension

$D = 2$ the critical temperature is zero. However, as we continue to lower the temperature, close enough to zero, a pseudogap will appear in the density of states (DOS) as a precursor to the anti-ferromagnetic phase (which has a full gap as its signature). An approach towards non-Fermi-liquid behavior is also visible in both the real and imaginary parts of the retarded self-energy. [1]

In Fig. 2.6 and Fig. 2.7, the densities of states (DOS) for lattices with finite sizes of 32×32, 64×64 and periodic boundary conditions and coarse-graining cluster sizes of 16×16 and 32×32 are plotted. We analytically continue the Green function in order to calculate the spectral function $A(k, \omega)$ and DOS using the Padé approximation. [32] In this approximation, we generate a continued fraction interpolating all the data points and use it as an analytic function of the Matsubara frequencies ω_n. The analytic continuation is accomplished by substituting ω_n with $\omega + i\eta$ where η is a small positive shift. However, the errors inherent in the numerical Fourier transform (FFT) and also the sharp high-frequency behavior of the Green function, FLEX potentials and the self-energy, limit the accuracy of the Padé. The high-frequency behavior is improved by implementing a more authentic cut off scheme introduced by Deisz *et al.* [33] in which the high-frequency tails of these quantities are Fourier transformed analytically prior to any numerical FFT and added back to the FFT outputs afterwards. In addition to this high-frequency cut off improvement, we also check for the analyticity of the Padé results in the upper-half frequency plane as a requirement for retarded physical quantities. This task is carried out by converting the continued fraction in the Padé into a ratio of two polynomials. The complex roots of these two polynomials are obtained via the Jenkins-Traub root finder routine. [34] Those orders of the Padé for which there exist poles in the upper-half plane are omitted unless these poles are canceled by the roots of the numerator. The acceptable Padé results correspond to the highest order with no uncompensated poles in the upper-half plane.

As seen in Fig. 2.6, by increasing the size of a finite lattice, the pseudogap occurs at higher temperatures and it also becomes less pronounced (sharper) as we approach the actual size of an infinite real lattice. The DCA yields a complementary behavior as shown in Fig. 2.7. By increasing the coarse-graining cluster size, similar to the finite size lattices, the pseudogap is shifted towards higher temperatures. However, unlike the finite size lattices, for the DCA the precursor becomes more pronounced (broader) as the cluster increases in size because the size of the lattice remains constant and the correlations are limited to the cluster size. Thus comparatively, *the DCA underestimates the gap while the finite size calculation overestimates it.*

By comparing the results in Fig. 2.6 and Fig. 2.7 one may see that the 32×32 DCA cluster yields more realistic physics than the corresponding 32×32 finite size lattice. The 64×64 finite size lattice results are also close to those for the 32×32 DCA cluster at slightly lower T (eg, $T = 0.055$ for the finite size and $T = 0.033$ for the DCA). However since the sizes of clusters are considerably smaller than the sizes of lattices, the DCA significantly reduces the complexity of the problem and consequently the CPU time. In terms of the CPU time, the FLEX with the numerical Fourier transforms scales as $\mathcal{N} ln \mathcal{N}$ where $\mathcal{N}$ is the product of the total number of Matsubara frequencies and the k points in the first Brillouin zone. Hence, using a 32×32 cluster in place of a 64×64 lattice both having 1024 Matsubara frequency points roughly reduces the CPU time by a factor of 4.4. If the DCA cluster size N_c equals the size of the finite lattice N, the DCA requires somewhat more CPU time than the finite size lattice due to course-graining. Nevertheless, comparatively, for large finite lattices such as 64×64, the lattice size contributions to the CPU time significantly dominate the coarse-graining ones in a 32×32 cluster. Thus, the 32×32 DCA cluster is much faster.

The FLEX often has difficulty reaching low temperatures. This is due to the fact that the χ_{ph} defined in Eq. 2.12 approaches unity as the temperature drops which in turn causes the $V^{(ph)}$ in Eq. 2.17 to diverge. In the DCA, χ_{ph} approaches unity more slowly, allowing the calculations to reach lower temperatures. One has to note that in the FLEX, the χ_{ph}^{DCA}

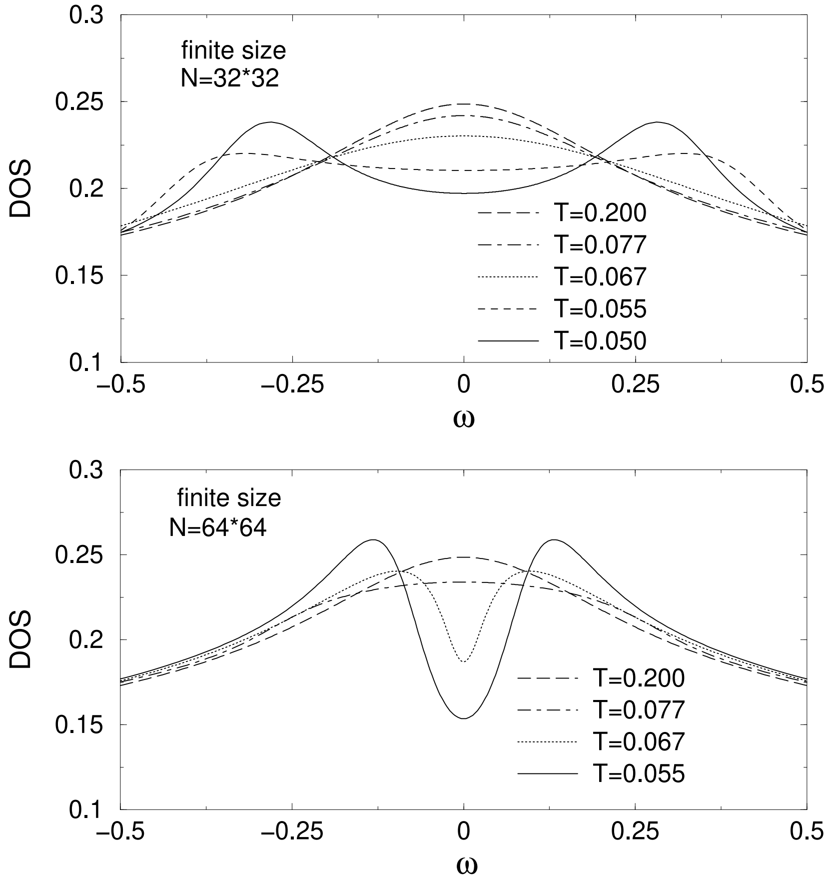

Figure 2.6: The FLEX density of states (DOS) for a 32×32 finite size lattice with periodic boundary conditions (top) versus energy for $U/t = 1.57$ at various temperatures, and for a 64×64 finite size lattice (bottom). The evolution of a week pseudogap is observed at $T = 0.067$ for the 64×64 lattice higher than $T = 0.055$ for the 32×32 one and the pseudogap is also much broader for the 32×32 lattice (128×128 finite size lattice results were obtained by Deisz *et al.* [1]).

is defined as follows

$$\chi_{ph}^{DCA}(\mathbf{Q},\omega_n) = \\ -U(T/N_c)\sum_{\mathbf{K}}\sum_{m}\bar{G}(\mathbf{K}+\mathbf{Q},\omega_n+\omega_m)\bar{G}(\mathbf{K},\omega_m)\,, \tag{2.21}$$

with $\bar{G}$ defined in Eq. 3.5. Fig. 2.8 illustrates the saturation of χ_{ph} for both the DCA and

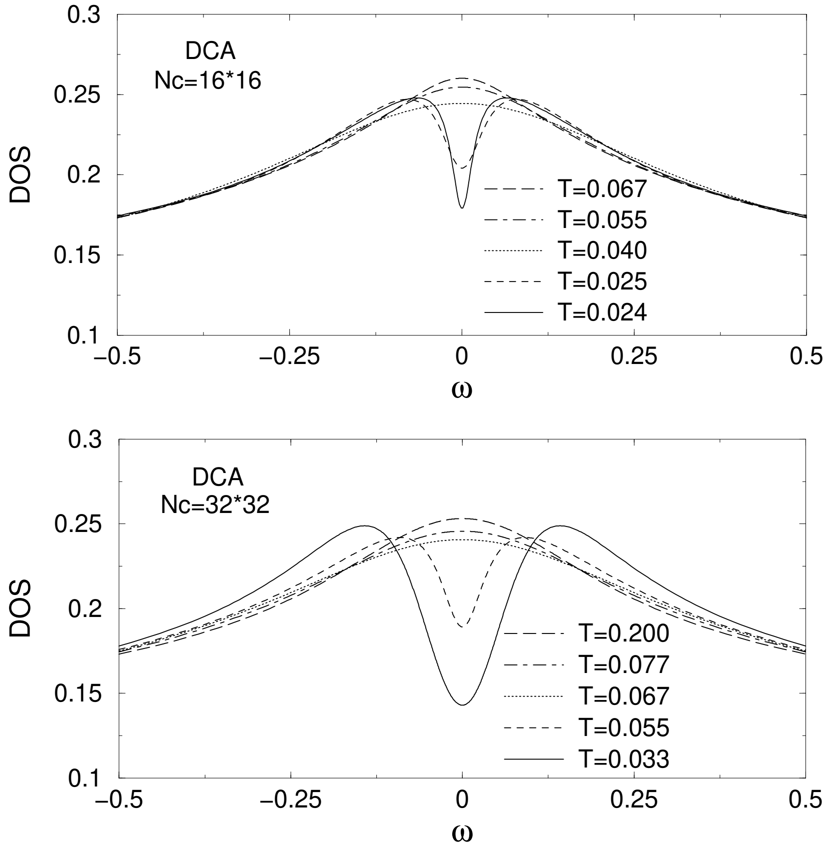

Figure 2.7: The FLEX density of states (DOS) for a 16×16 DCA cluster (top) versus energy for $U/t = 1.57$ at various temperatures, and for a 32×32 DCA cluster (bottom). For the 32×32 cluster, the evolution of a weak pseudogap is observed at $T = 0.055$ higher than $T = 0.025$ for the 16×16 one and the pseudogap is also broader for the 32×32 cluster.

finite size lattices. The χ_{ph} for the 32×32 finite size lattice (filled circles) saturates at higher temperatures compared to the 32×32 DCA cluster (open diamonds) indicating that in the DCA, for a certain cluster size, the precursor to the phase transition can evolve to lower temperatures compared to a finite size lattice of the same size with periodic boundary conditions. However, for the correlation length $\xi > L$ the DCA approximation breaks down and replacing the self-energy by its coarse-grained counterpart is no longer accurate. Here, the DCA takes on significant mean-field character.

Another feature of the Hubbard model near half-filling verified by the FLEX [1] is non-Fermi-liquid behavior. Here, this is studied by increasing the electron electron interaction U at a constant temperature. In Fig. 2.9 and Fig. 2.10 the real and imaginary parts of the self-energy at the X point (on the non-interacting Fermi surface) have been plotted versus energy for finite size lattices and the DCA respectively. As the interaction is increased, the negative slope in the real part turns positive around $\omega = 0$ which is inconsistent with the requirement that the renormalization factor $[1 - \partial Re\Sigma(\mathbf{k}_F, \omega)/\partial\omega|_{\omega=0}]^{-1}$ should be smaller than unity in the Fermi-liquid theory. There also appears an anomalous inverted peak in the imaginary part at $\omega = 0$.

As presented in Fig. 2.9, by increasing the length of the finite size lattice, the sharpness of the non-Fermi-liquid features is reduced. The same features for the DCA in Fig. 2.10 are slightly less pronounced and in a complementary fashion to the finite size lattices, their sharpness is enhanced by increasing the size of the cluster. Thus, again the DCA underestimates the non-Fermi-liquid features while the finite size calculation overestimates it.

Earlier in Fig. 2.8 it was shown that the FLEX particle-hole bubble $\chi_{ph}(q, \omega_m = 0)$ at $q = Q = (\pi, \pi)$ approaches unity as the temperature is lowered. This causes the spin-fluctuation T matrix

$$T_{\sigma,\sigma}(q, \omega_m) = \frac{3}{2}[\frac{\chi_{ph}(q, \omega_m)^2}{1 - \chi_{ph}(q, \omega_m)}]\,, \tag{2.22}$$

which is just the third term in $V^{(ph)}(q, \omega_m)$ in Eq. 2.17 to peak around the $(Q, \omega_m = 0)$ point. For real frequencies, $T_{\sigma,\sigma}(Q, \omega)$ has a sharp peak around $\omega = 0$. Since $T_{\sigma,\sigma}(Q, \omega)$ is only used to construct the irreducible self-energy, within the DCA it is constructed from coarse-grained Green functions. Thus, the DCA counterpart of Eq. 2.22 is obtained by only replacing the χ_{ph} with χ_{ph}^{DCA} defined in Eq. 2.21. Fig. 2.11 and Fig. 2.12 show how this peak sharpens as the temperature decreases or interaction increases for finite size lattices and the

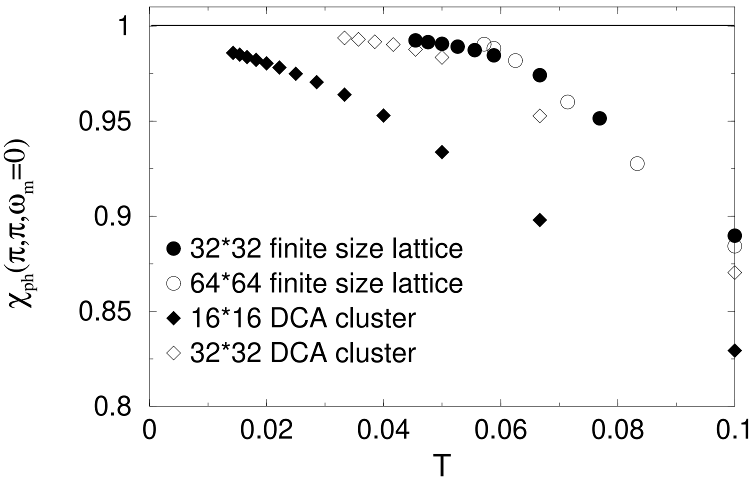

Figure 2.8: The FLEX particle-hole bubble (χ_{ph}) at $Q = (\pi, \pi)$ and $\omega_m = 0$ for a 16×16 and 32×32 DCA clusters (diamonds) and also for 32×32 and 64×64 finite size lattices with periodic boundary conditions (circles) versus temperature T at $U/t = 1.57$. The relatively rapid saturation of the finite size lattice χ_{ph} compared to the more gradual approach of the DCA results towards unity is manifest (128×128 finite size lattice results were obtained by Deisz *et al.* [1]).

DCA respectively. In the 64×64 finite size lattice (c.f. Fig 2.11 bottom), the peak continues to develop as the temperature is lowered and the interaction is raised. At $T = 0.067$ and $U = 1.6$ where there exists a pseudogap in the DOS, the peak undergoes a significant growth compared to the other graphs shown in the same figure. The 32×32 (c.f. Fig 2.11.top) lattice presents the same behavior with a slightly sharper but shorter peak.

The DCA also illustrates the same type of peaks at a slightly higher interaction and lower temperatures for the 16×16 cluster (c.f. Fig 2.12 top). Increasing the cluster size to 32×32 gives rise to higher peaks similar to the finite size lattices case but unlike the finite size lattices peaks become sharper as the size is increased.

All the results illustrated in this section indicate the complementarity of the DCA to the finite size lattice scheme. It is also observed that the DCA is capable of reproducing relatively the same physics as the finite size FLEX at slightly different parameters but a

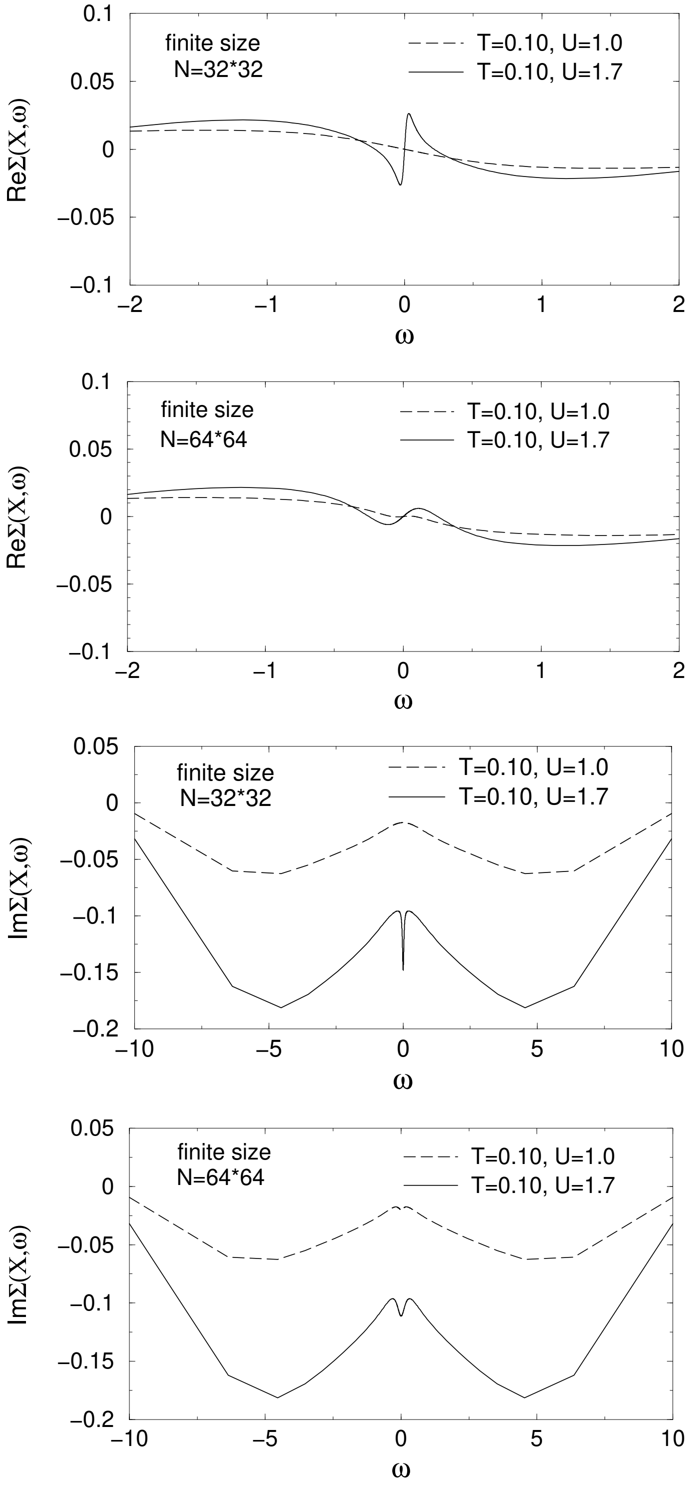

Figure 2.9: The FLEX real (top two) and imaginary (bottom two) parts of the self-energy at the X point for 32×32 and 64×64 finite size lattices with periodic boundary conditions versus energy for $T = 0.10$ and two different interactions U. The inverted peak at $\omega = 0$ in the imaginary part and the positive slope in the real part are both signatures of non-Fermi-liquid behavior. For smaller lattice sizes these signatures are more pronounced (128×128 finite size lattice results were obtained by Deisz *et al.* [1]).

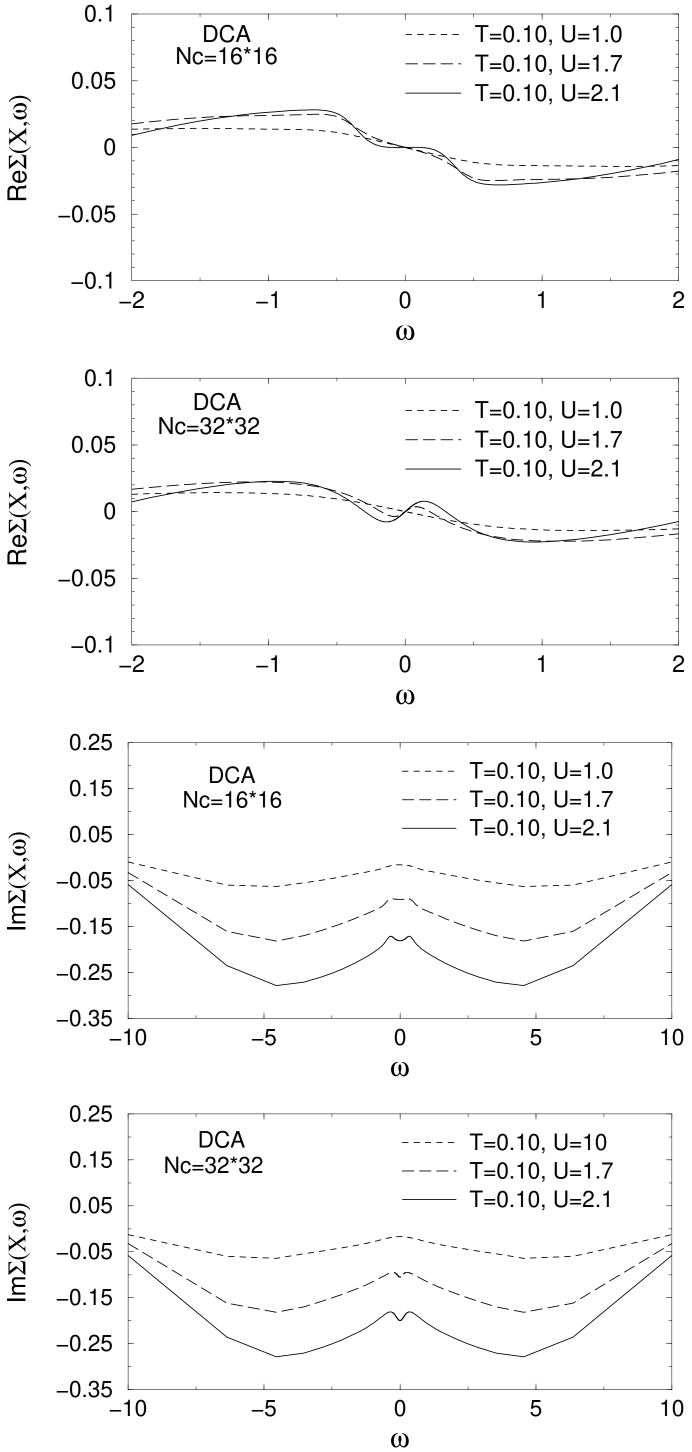

Figure 2.10: The FLEX real (top two) and imaginary (bottom two) parts of the self-energy at the X point for 16×16 and 32×32 DCA clusters versus energy for $T = 0.10$ and two different interactions U. The non-Fermi-liquid features occur at slightly higher interactions compared to the finite size lattices. Upon increasing the cluster size, these features become more pronounced (complementary to the finite size lattices with periodic boundary conditions).

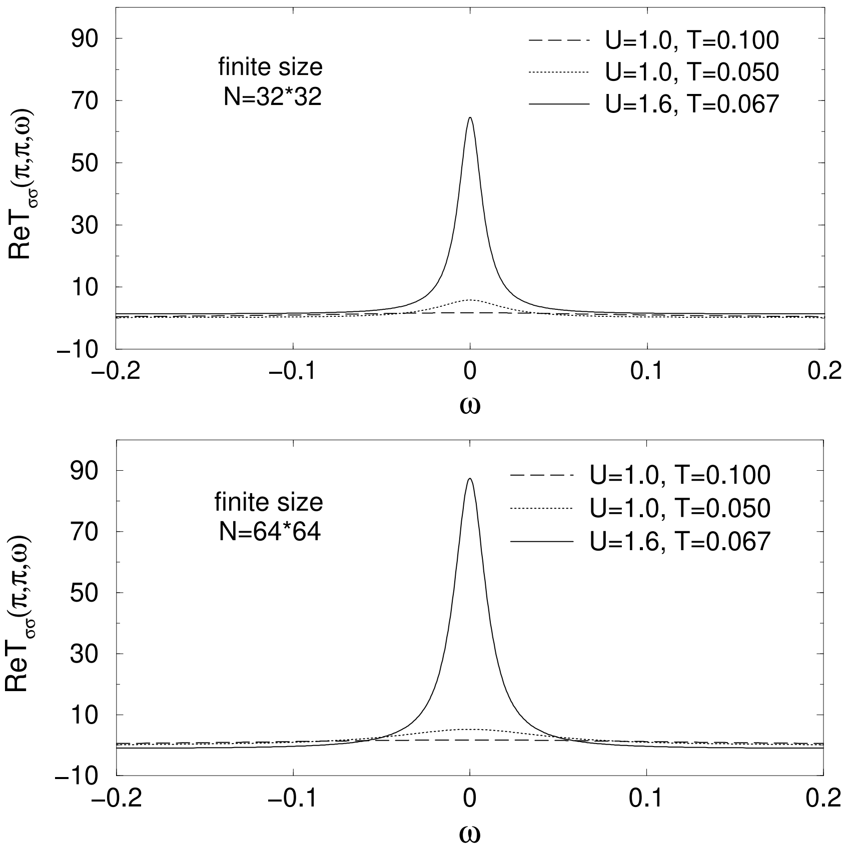

Figure 2.11: The FLEX real part of the T-matrix at $Q = (\pi, \pi)$ versus energy for 32×32 (top) and 64×64 (bottom) finite size lattices with periodic boundary conditions. For the 32×32 finite size lattice at $T = 0.067$ and $U/t = 1.6$ (solid), we observe a huge peak due to the formation of a pseudogap in the DOS. By increasing the lattice size to 64×64 a higher and broader peak occurs at the same temperature.

lower CPU cost. The combination of these two facts makes this technique a good candidate to be employed in the numerical treatment of a wide range of many-body problems.

Lastly, to better understand the effect of the DCA cluster embedded in a Fermionic bath, we can rewrite the course grained Green function defined in Eq. 3.5 as

$$\bar{G}(\mathbf{K}, z) = \frac{1}{z - \bar{\epsilon}_{\mathbf{K}} - \Sigma(\mathbf{K}, z) - \Gamma(\mathbf{K}, z)}\,. \tag{2.23}$$

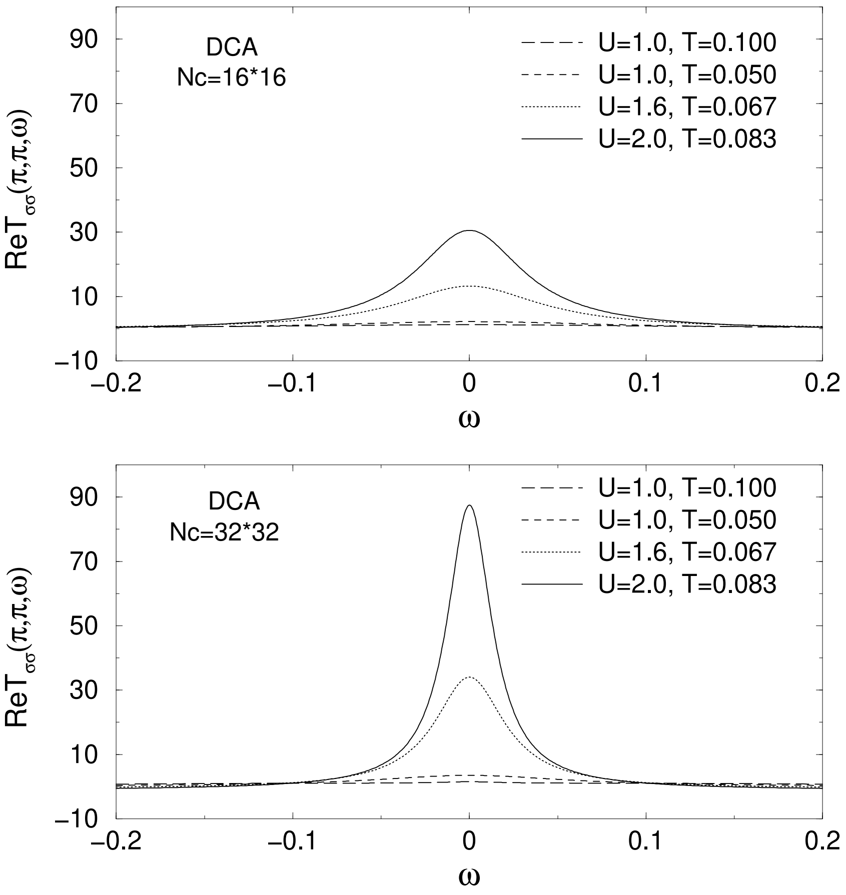

Figure 2.12: The FLEX real part of the T-matrix at $Q = (\pi, \pi)$ versus energy for 16×16 (top) and 32×32 (bottom) DCA clusters. Peaks similar to the finite size lattices appear at slightly higher interactions and lower temperatures. By increasing the cluster size, the peaks grow higher (similar to finite size lattices) and also sharpen (complementary to the finite size lattices).

where $\bar{\epsilon}_K = N_c/N \sum_{\tilde{\mathbf{k}}} \epsilon_{\mathbf{K}+\tilde{\mathbf{k}}}$ and $\Gamma(\mathbf{K}, z)$ is the host function. Maier *et al.* [26], define

$$t_{\mathbf{K}+\tilde{\mathbf{k}}} = \epsilon_{\mathbf{K}+\tilde{\mathbf{k}}} - \bar{\epsilon}_{\mathbf{K}}\,, \tag{2.24}$$

whereby $\Gamma(\mathbf{K}, z)$ can be expressed as

$$\Gamma(\mathbf{K}, z) = \frac{\frac{N_c}{N}\sum_{\tilde{\mathbf{k}}} t^2{}_{\mathbf{K}+\tilde{\mathbf{k}}} G(\mathbf{K}+\tilde{\mathbf{k}}, z)}{1 + \frac{N_c}{N}\sum_{\tilde{\mathbf{k}}} t_{\mathbf{K}+\tilde{\mathbf{k}}} G(\mathbf{K}+\tilde{\mathbf{k}}, z)} \,. \tag{2.25}$$

By Taylor expanding $t_{\mathbf{K}+\tilde{\mathbf{k}}}$ around the cluster points $\mathbf{K}$ it is found that $t_{\mathbf{K}+\tilde{\mathbf{k}}} \sim \mathcal{O}(\Delta k)$ with $\Delta k = 2\pi/L$. Thus, Eq. 2.25 yields $\Gamma(\mathbf{K}) \sim \mathcal{O}((\Delta k)^2)$ as $\Delta k \to 0$. To illustrate this, we calculate $\Gamma(r = 0, \tau = 0)$ by summing over all the $\mathbf{K}$ points and ω_n frequencies and plot it versus $(\Delta k)^2$. Fig. 2.13 illustrates this linear behavior for $N_c \geq 16$. $N_c = 1$ holds complete mean field characters and no non-local fluctuations. $N_c = 4$ is anomalous as explained in an article by Betts *et al.* [17] There, the finite size cubic lattices with less than six (four in $2D$ square lattices) distinct nearest neighbors per each site are not used in finite size scalings for estimating the physical properties of models like the spin one half XY ferromagnet or the Heisenberg antiferromagnet. For $N_c = 4$, because of the periodicity of the clusters, each cluster point is surrounded by two identical nearest neighbors in every direction and therefore has only two distinct nearest neighbors (c.f. Fig. 2.14). Thus, the effect of fluctuations are overestimated. [35] For $N_c > 4$ there is no such anomaly and hence, all the points present the linear behavior proven above. Nevertheless, calculations with $N_c = 4$ do a reasonable job in capturing the qualitative effects of corrections to the DMFA.

2.7 DCA in frequency space

As illustrated for the momentum space, the DCA results in a significant reduction of the problem complexity and it is complementary to the finite size lattice approach. In analogy to the momentum space, one could consider dividing the one dimensional Matsubara frequency space into a number of coarse-graining subcells. For both fermions and bosons, each cell should include an odd number of frequencies in order for the frequencies in the centers of these cells to preserve Fermionic or Bosonic properties. Fig. 2.15 represents how the

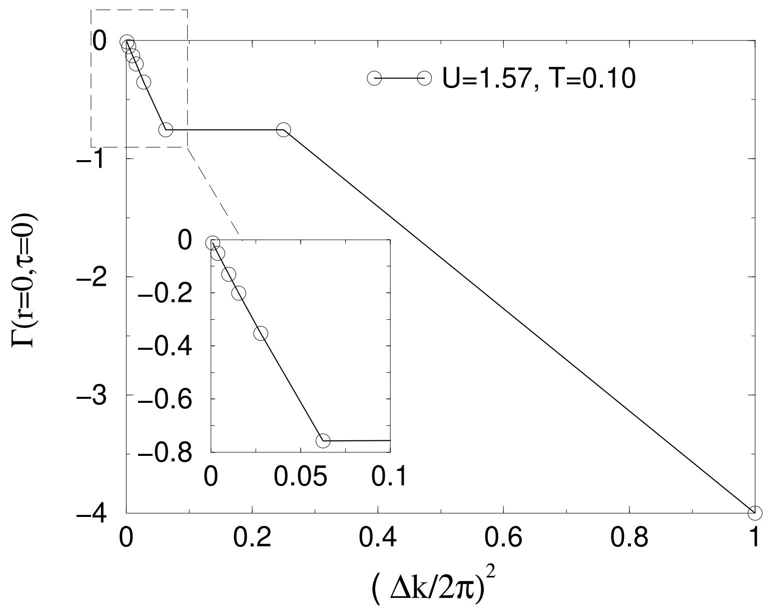

Figure 2.13: The host function $\Gamma(r = 0, \tau = 0)$ versus $(\Delta k)^2$. The linear behavior beyond $N_c = 4$ is manifest, see also the inset.

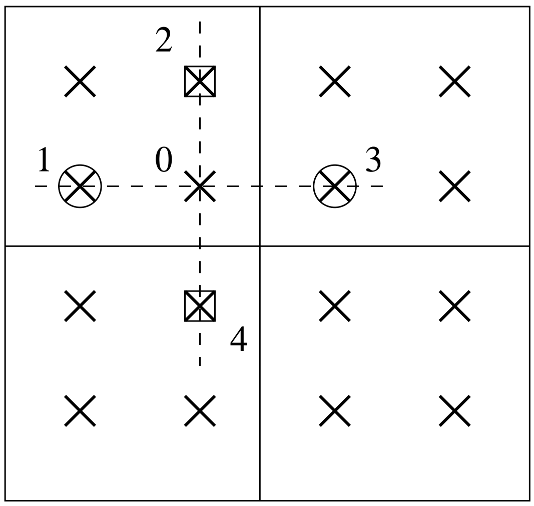

Figure 2.14: DCA clusters in the real space lattice with $N_c = 4$. Due to the periodicity of the clusters, points 2 and 4 in squares and 1 and 3 in circles are equivalent and therefore point 0 observes its nearest neighbors twice in each direction.

frequency space can be divided into coarse-graining subcells each comprising a central Ω_n frequency and a number of coarse-graining $\tilde{\omega}_n$ lying around it. The central Ω_n frequencies can be rewritten in the form of the original lattice with renormalized β shown as β_c in the figure. Similar to the case of the momentum space, we make the following transformation for the Laue function

$$\Delta = \beta \ \delta_{\omega_{n1},\omega_{n2}+\omega_{n3}} \rightarrow \Delta_{DCA} = \beta_c \ \delta_{\Omega_{n1},\Omega_{n2}+\Omega_{n3}} \,, \tag{2.26}$$

for the Matsubara frequencies of the vertex shown in Fig. 1.3 considering frequency dependent interactions in general (in condensed matter physics, most of the interactions are indeed simultaneous and thus frequency independent). As a result, we may again coarse-grain the Green function over the subcell frequencies

$$\bar{G}(\mathbf{K}, \Omega_n) = \frac{\beta_c}{\beta} \sum_{\tilde{\omega}_n} G(\mathbf{K}, \Omega_n + \tilde{\omega}_n) \,. \tag{2.27}$$

According to Fig. 2.15, the full coarse-graining of the Green function amounts to $\beta_c \rightarrow 0$ which causes all the self-energy Feynman diagrams ordered higher than first (Hartree-Fock diagrams) to vanish and consequently we arrive at a fully static problem.

Unfortunately, we can show that coarse-graining over Matsubara frequencies can lead to the violation of causality and as a result, the DCA is not systematically implementable for the Matsubara frequency quantities. The simplest example is the non-interacting Green function coarse-grained as follows [36]

$$\begin{aligned} \bar{G}^{(0)}(\mathbf{K}, \Omega_n) &= \frac{\beta_c}{\beta} \sum_{\tilde{\omega}_n} G^{(0)}(\mathbf{K}, \Omega_n + \tilde{\omega}_n) = \\ \frac{\beta_c}{\beta} \sum_{\tilde{\omega}_n} & \frac{1}{i\Omega_n + i\tilde{\omega}_n - \epsilon_k + \mu} \,. \end{aligned} \tag{2.28}$$

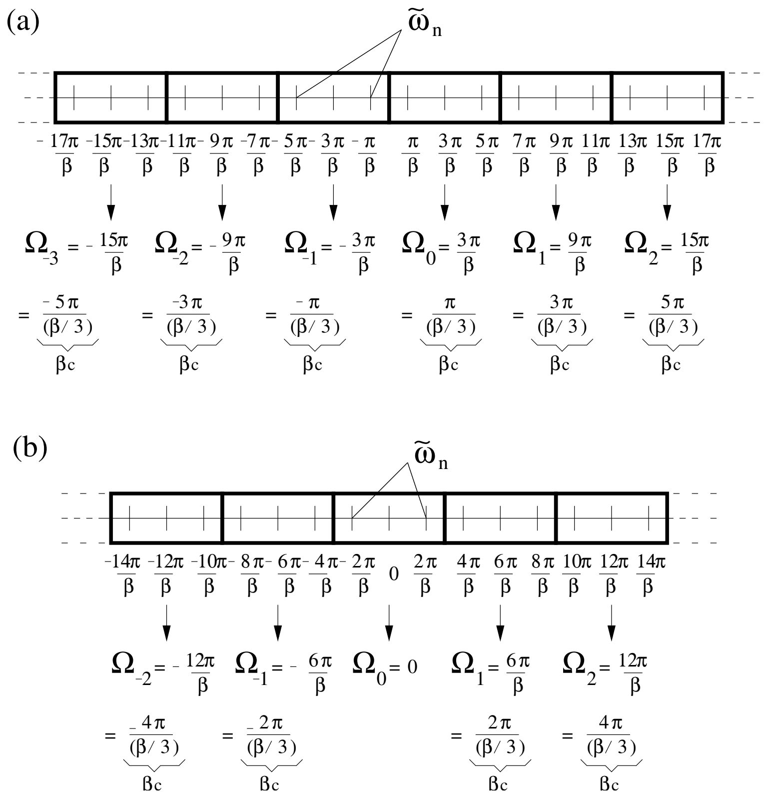

Figure 2.15: Dividing the fermion (a) and boson (b) Matsubara frequency spaces into subcells. The central Ω_n frequencies can be written in the form of the original lattice with renormalized β denoted as β_c ($\beta_c = \beta/3$ in this case).

The retarded Green function is derived by the substitution $i\Omega_n \rightarrow \Omega + i\eta$

$$\bar{G}^{(0)}_{ret}(\mathbf{K}, \Omega) = \frac{\beta_c}{\beta} \sum_{\tilde{\omega}_n} \frac{1}{\Omega + i\eta + i\tilde{\omega}_n - \epsilon_k + \mu} \, . \tag{2.29}$$

The theory of analytic functions of a complex variable tells us that in order for the Green function to remain retarded in the time space, $\bar{G}^{(0)}_{ret}(\mathbf{K}, \Omega)$ must not have any poles in the upper half plane of Ω. In Eq. 2.29, one could readily create poles in the upper half plane for negative $\tilde{\omega}_n$ which causes causality violation and consequently unphysical results.

The way around this difficulty is to use real frequencies even at finite temperatures. By invoking real frequencies we no longer coarse-grain over imaginary values. Therefore, the

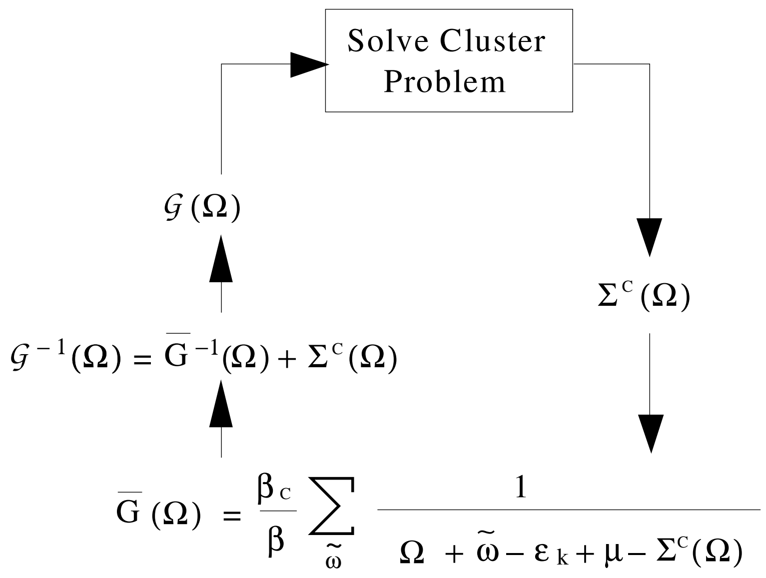

Figure 2.16: The algorithm for the cluster solvers such as the NCA in which at each step before using the cluster solver the bare Green function is calculated by excluding the cluster self-energy. This is the only step through the algorithm where problems with causality might occur.

retarded Green function will never acquire poles in the upper half plane and remains causal as shown below

$$\begin{aligned} &\bar{G}_{ret}(\mathbf{K},\Omega) = \\ &\qquad \frac{N_{\tilde{\omega}}}{N_{\omega}}\sum_{\tilde{\omega}} \frac{1}{\Omega + \tilde{\omega} + i\eta + -\epsilon_k + \mu - \Sigma_{ret}(\mathbf{K},\Omega)}\,, \end{aligned} \tag{2.30}$$

with N_{ω} the total number of frequencies and $N_{\tilde{\omega}}$ the number of those we coarse-graining over in each cell. In Ref. [16], a formal proof of causality is given (based on a geometrical argument) for coarse-graining in the momentum space. This proof can be straightforwardly applied to the real frequency space as well and it extends the application of real frequency DCA not only to the perturbative cluster solvers such as the FLEX but also techniques like the NCA.

Lastly, similar to the momentum space, care must be taken when choosing the the size of the frequency coarse-graining cells. One must make sure that the cells are not larger than some characteristic energy scale (e.g. the Kondo temperature T_K) as the coarse-graining would then suppress the relevant physics.

2.8 Summary

We introduce and examine the DCA in detail by employing it with the FLEX to study the half filled two dimensional Hubbard model. The FLEX is not as precise as nearly exact techniques such as quantum Monte Carlo in describing the Hubbard model at strong interaction regime. However, it is capable of illustrating the utility of the DCA, including the complementarity and convergence of the DCA compared to finite size lattice approaches. The DCA and finite size calculations (with periodic boundary conditions) both converge with corrections $\mathcal{O}(\lambda/L^2)$; however, in our example the coefficient λ_{DCA} was smaller and of opposite sign than λ_{FS}, indicating that the DCA converges more quickly and from a complementary direction. This complementarity was also seen in other quantities such as the pseudogap in the density of state and the non-Fermi liquid behaviour that the DCA (finite size) calculation systematically under (over) estimates.

It also appears that coarse-graining the Green functions over the Matsubara frequencies can and will lead to the violation of causality and therefore is pathological. Nevertheless, one can coarse-grain the Green function over real frequencies and preserve the causality not only for the FLEX but also cluster solvers such as NCA in which the cluster contribution to the coarse-grained dressed Green function is excluded before being inserted in the cluster solver.

The outlook for the FLEX-DCA approach is promising. Although the FLEX fails to accurately describe short-ranged physics such as moment formation (and related phenomena like the Mott gap), it does a good job describing long-ranged physics associated with spin and charge fluctuations. On the other hand, numerically exact calculations such as QMC, are too expensive to perform for large clusters, and are thus restricted to the study of short-length scales. However, since the DCA gives us a way of parsing the problem into different length scales, it may be used to combine the short-length scale information from the QMC with the long length scale information from the FLEX. This may be accomplished, by embedding a QMC cluster, of size L, into a much larger FLEX cluster of size $L' \gg L$, which is itself embedded in a mean-field. As we have shown here, this approach should be implemented by approximating the generating functional $\Phi \approx \Phi_{QMC}(L) - \Phi_{FLEX}(L) + \Phi_{FLEX}(L')$. Work along these lines is in progress.

Chapter 3

Microscopic theory of the DCA

3.1 Introduction

Strongly correlated electron systems are often characterized by short range dynamical fluctuations. Consequently, local approximations like the dynamical mean field approximation (DMFA) [14, 15, 37, 38] successfully describe many of the qualitative properties. However, in low-dimensional systems, spatial correlations become increasingly important and are thought to be responsible for e.g. non-Fermi-liquid behavior and d-wave pairing in the cuprate superconductors.

The Dynamical Cluster Approximation (DCA) was introduced as a technique to include such non-local corrections to DMFA [16, 25]. This is accomplished by mapping the lattice problem onto that of a self-consistently embedded cluster, with periodic boundary conditions. The DCA may also be viewed diagrammatically as an approximation which systematically restores momentum conservation at the internal vertices of many body Feynman diagrams, which is relinquished in the local DMFA. Here, we investigate one of the central approximations of the DCA: that compact (skeletal) contributions to the thermodynamic potential are well approximated by their cluster counterparts; whereas non-compact (non-skeletal) contri-

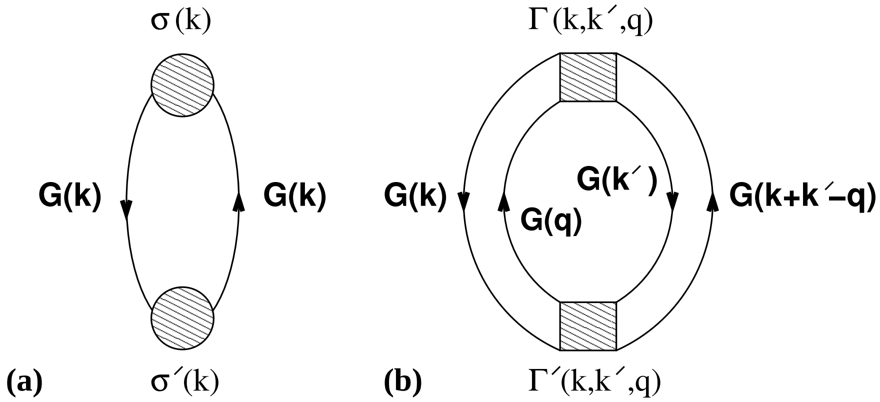

Figure 3.1: *(a) typical non-compact (non skeletal) and (b) typical compact (skeletal) diagrams.(K. Aryanpour et al., [2])*

butions should not be approximated by their cluster counterparts. Rather, they should be constructed using the appropriate Dyson equation.

3.2 General considerations

Following Baym [31], a microscopic theory may be defined by its approximation to the generating functional $\Phi[G]$ defining the thermodynamic potential (difference) of the system via

$$\Delta\Omega = \Omega - \Omega_0 = -2\mathrm{Tr}[\Sigma G - \ln(G/G_0)] + \Phi[G]\,, \tag{3.1}$$

where G is the full and G_0 the bare one particle Green function, and Σ the self energy. $\Phi[G]$ is a sum of all compact (skeletal) closed connected Feynman diagrams. The other contributions to the thermodynamic potential incorporate non-compact diagrams. Typical compact and non-compact diagrams are illustrated in Fig. 3.1. In the non-compact diagram, two self energy pieces σ and σ' are connected with two Green functions. In the compact diagram, two vertex parts, Γ and Γ', are connected with four Green functions. [39]

As shown by Müller–Hartmann [14], the DMFA may be defined by relinquishing the momentum conservation at each internal vertex in $\Phi[G]$ [40]. This conservation is described by the Laue function

$$\Delta = \sum_{\mathbf{x}} e^{i\mathbf{x}\cdot(\mathbf{k}_1+\mathbf{k}_2-\mathbf{k}_3-\mathbf{k}_4)} = N\delta_{\mathbf{k}_1+\mathbf{k}_2,\mathbf{k}_3+\mathbf{k}_4} \,. \tag{3.2}$$

In the Dynamical Mean Field Approximation (DMFA), momentum conservation is completely abandoned and the Laue function $\Delta_{DMFA} \equiv 1$. We may then sum freely over all the internal momenta labels.

The DCA is constructed to systematically restore the momentum conservation at each internal vertex, by mapping the lattice onto a self-consistently embedded cluster problem. We have provided a microscopic definition of the DCA through its Laue function. However, to clarify the relation between this microscopic definition, and the cluster problem, we must first decompose the lattice into clusters, and define the corresponding problem in reciprocal space. Here, the real lattice of N sites is tiled by N/N_c clusters each composed of $N_c = L^D$ sites where D is dimensionality and L the size of clusters (c.f. Fig. 1.2 for $L = D = 2$). We label the origin of the clusters by $\tilde{\mathbf{x}}$ and the N_c intra-cluster sites by $\mathbf{X}$. So for each site in the original lattice $\mathbf{x} = \mathbf{X} + \tilde{\mathbf{x}}$. In the reciprocal space, the points $\tilde{\mathbf{x}}$ and $\mathbf{X}$ form lattices labeled by $\tilde{\mathbf{k}}$ and $\mathbf{K}$ respectively with $K_\alpha = n_\alpha \cdot 2\pi/L$ and integer n_α. Then $\mathbf{k} = \mathbf{K} + \tilde{\mathbf{k}}$ (see Fig. 1.2).

In the DCA, we first make the separation

$$\Delta = \frac{N}{N_c}\delta_{\tilde{\mathbf{k}}_1+\tilde{\mathbf{k}}_2,\tilde{\mathbf{k}}_3+\tilde{\mathbf{k}}_4}\; N_c\delta_{\mathbf{K}_1+\mathbf{K}_2,\mathbf{K}_3+\mathbf{K}_4} \tag{3.3}$$

and then set $N/N_c\delta_{\tilde{\mathbf{k}}_1+\tilde{\mathbf{k}}_2,\tilde{\mathbf{k}}_3+\tilde{\mathbf{k}}_4} \cong 1$, so that

$$\Delta_{DCA} = N_c\delta_{\mathbf{K}_1+\mathbf{K}_2,\mathbf{K}_3+\mathbf{K}_4} \,, \tag{3.4}$$

which indicates that the momentum is partially conserved for transfers between the cells.

In this chapter, we consider the approximation made through the substitution $\Delta \to \Delta_{DCA}$ in the compact and non-compact contributions to the thermodynamic potential. Whenever the substitution is made, all internal legs are replaced by the coarse grained Green function defined by

$$\bar{G}(\mathbf{K}, z) = \frac{N_c}{N} \sum_{\tilde{\mathbf{k}}} G(\mathbf{K} + \tilde{\mathbf{k}}, z) \,. \tag{3.5}$$

The corresponding estimate of the self energy will then necessarily be a function of $\mathbf{K}$ and (complex) frequency z. The DCA estimate of the lattice Green function is then given by

$$G(\mathbf{k}, z) = \frac{1}{z - \epsilon_{\mathbf{k}} + \mu - \Sigma_{DCA}(\mathbf{K}, z)} \,. \tag{3.6}$$

It is of importance to note that by using Eq. 3.6 we have already made the approximation $\Sigma(k, z) = \Sigma_{DCA}(\mathbf{K}, z) + \mathcal{O}((\Delta k a)^2)$ where Δk is the size of the coarse graining cell shown in Fig. 1.2 and a is the lattice constant (chosen as unity). We also drop the frequency label from this point on for simplicity.

3.3 Coarse graining compact vs. non-compact diagrams

We investigate the additional approximations associated with coarse graining in compact and non-compact diagrams. To do this we will consider diagrams with all legs coarse-grained, except those explicitly displayed in Figs. 3.2 and 3.3. Consider the first non trivial correction to the coarse grained non compact diagrams as illustrated in Fig.3.2.

$$\delta^{(1)}[\Delta\Omega_{ncp}] \sim \frac{1}{N_c} \sum_{\mathbf{K}_1, \mathbf{K}_2} \sigma(\mathbf{K}_1, \mathbf{K}_2) \sigma'(\mathbf{K}_1, \mathbf{K}_2) \int_{-\infty}^{\infty}$$

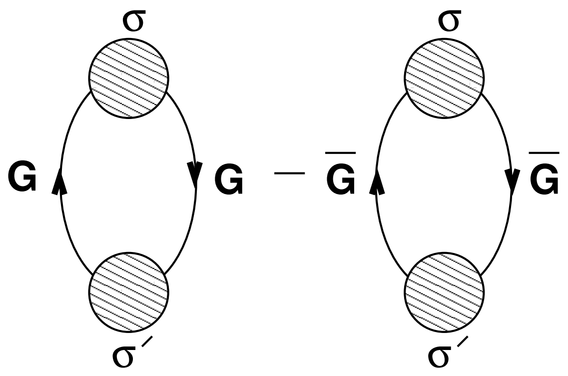

Figure 3.2: First correction by non-compact diagrams, $\delta^{(1)}[\Delta\Omega_{ncp}]$.(K. Aryanpour *et al.*, [2])

$$\int_{-\infty}^{\infty} d\epsilon_1 d\epsilon_2 G(\mathbf{K}_1, \epsilon_1) G(\mathbf{K}_2, \epsilon_2)[\rho_{ncp}(\epsilon_1, \mathbf{K}_1; \epsilon_2, \mathbf{K}_2) - \bar{\rho}_{ncp}(\epsilon_1, \mathbf{K}_1; \epsilon_2, \mathbf{K}_2)]\ \delta_{\mathbf{K}_2, \mathbf{K}_1}\ , \tag{3.7}$$

where

$$\rho_{ncp}(\epsilon_1, \mathbf{K}_1; \epsilon_2, \mathbf{K}_2) = \frac{N_c}{N} \sum_{\tilde{\mathbf{k}}_1, \tilde{\mathbf{k}}_2} \delta(\epsilon_1 - \epsilon_{\mathbf{K}_1 + \tilde{\mathbf{k}}_1}) \times \delta(\epsilon_2 - \epsilon_{\mathbf{K}_2 + \tilde{\mathbf{k}}_2})\ \delta_{\tilde{\mathbf{k}}_2, \tilde{\mathbf{k}}_1}\ , \tag{3.8}$$

and

$$\bar{\rho}_{ncp}(\epsilon_1, \mathbf{K}_1; \epsilon_2, \mathbf{K}_2) = \frac{N_c^2}{N^2} \sum_{\tilde{\mathbf{k}}_1, \tilde{\mathbf{k}}_2} \delta(\epsilon_1 - \epsilon_{\mathbf{K}_1 + \tilde{\mathbf{k}}_1}) \times \delta(\epsilon_2 - \epsilon_{\mathbf{K}_2 + \tilde{\mathbf{k}}_2})\ . \tag{3.9}$$

In the above derivations we assumed that the self energy is $\tilde{\mathbf{k}}$ independent and therefore

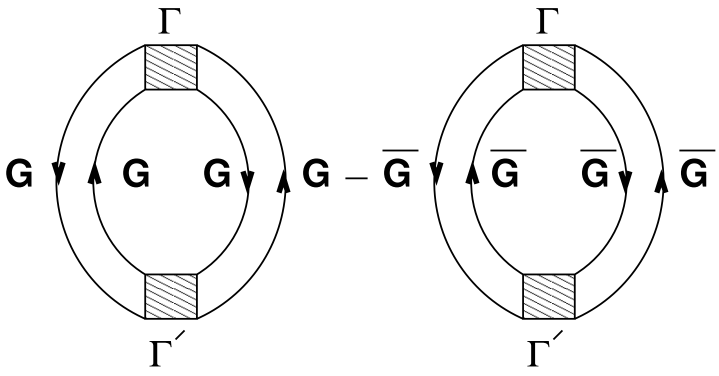

Figure 3.3: First correction by compact diagrams, $\delta^{(1)}[\Delta\Omega_{cp}]$.(K. Aryanpour *et al.*, [2])

the entire $\tilde{\mathbf{k}}$ dependence of the Green function is only through the dispersion ϵ given by

$$\epsilon_{\mathbf{K}+\tilde{\mathbf{k}}} = -2t/(2D)^{1/2}.\sum_{n=1}^{D}\cos(\mathbf{K}_n + \tilde{\mathbf{k}}_n)\,, \tag{3.10}$$

which is just the non interacting dispersion of the Hubbard model Hamiltonian with nearest neighbor hoppings and dimensionality D. By the same token, in Fig. 3.3, for the compact part with coarse grained Γ and Γ' we have

$$\begin{aligned}
&\delta^{(1)}[\Delta\Omega_{cp}] \sim \frac{1}{N_c^3}\sum_{\substack{\mathbf{K}_1,\mathbf{K}_2\\ \mathbf{K}_3,\mathbf{K}_4}}\delta_{\mathbf{K}_4,\mathbf{K}_1+\mathbf{K}_2-\mathbf{K}_3}\Gamma(\mathbf{K}_1,\mathbf{K}_2,\mathbf{K}_3,\mathbf{K}_4)\times\\
&\Gamma'(\mathbf{K}_1,\mathbf{K}_2,\mathbf{K}_3,\mathbf{K}_4)\int_{-\infty}^{\infty}\int_{-\infty}^{\infty}\int_{-\infty}^{\infty}\int_{-\infty}^{\infty}d\epsilon_1 d\epsilon_2 d\epsilon_3 d\epsilon_4\\
&G(\mathbf{K}_1,\epsilon_1)G(\mathbf{K}_2,\epsilon_2)G(\mathbf{K}_3,\epsilon_3)G(\mathbf{K}_4,\epsilon_4)\,[\,\rho_{cp}(\epsilon_1,\mathbf{K}_1;\epsilon_2\\
&,\mathbf{K}_2;\epsilon_3,\mathbf{K}_3;\epsilon_4,\mathbf{K}_4) - \bar{\rho}_{cp}(\epsilon_1,\mathbf{K}_1;\epsilon_2,\mathbf{K}_2;\epsilon_3,\mathbf{K}_3;\epsilon_4,\mathbf{K}_4)\,]\,,
\end{aligned} \tag{3.11}$$

where

$$\rho_{cp}(\epsilon_1,\mathbf{K}_1;\epsilon_2,\mathbf{K}_2;\epsilon_3,\mathbf{K}_3;\epsilon_4,\mathbf{K}_4) = \frac{N_c^3}{N^3}\sum_{\substack{\tilde{\mathbf{k}}_1,\tilde{\mathbf{k}}_2\\ \tilde{\mathbf{k}}_3,\tilde{\mathbf{k}}_4}}$$

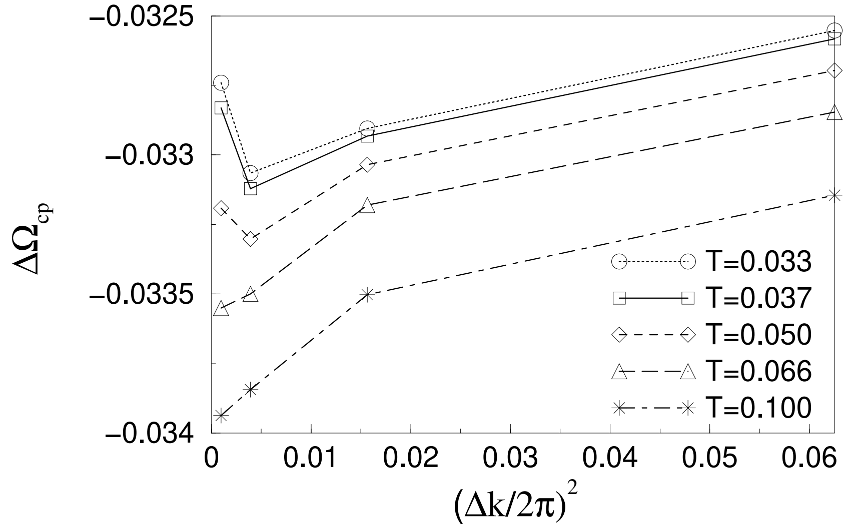

Figure 3.4: The compact contribution to the thermodynamic potential versus $(\Delta k)^2$ at $U/t = 1.57$ and various temperatures, using coarse-grained Green functions. The deviation from linearity at the lowest temperatures hint at the correlation length exceeding the cluster size. (K. Aryanpour *et al.*, [3])

$$\delta(\epsilon_1 - \epsilon_{\mathbf{K}_1+\tilde{\mathbf{k}}_1})\delta(\epsilon_2 - \epsilon_{\mathbf{K}_2+\tilde{\mathbf{k}}_2})\delta(\epsilon_3 - \epsilon_{\mathbf{K}_3+\tilde{\mathbf{k}}_3}) \times$$
$$\delta(\epsilon_4 - \epsilon_{\mathbf{K}_4+\tilde{\mathbf{k}}_4})\ \delta_{\tilde{\mathbf{k}}_4,\tilde{\mathbf{k}}_1+\tilde{\mathbf{k}}_2-\tilde{\mathbf{k}}_3}\,, \tag{3.12}$$

and

$$\bar{\rho}_{cp}(\epsilon_1, \mathbf{K}_1; \epsilon_2, \mathbf{K}_2; \epsilon_3, \mathbf{K}_3; \epsilon_4, \mathbf{K}_4) =$$
$$\frac{N_c^4}{N^4} \sum_{\substack{\tilde{\mathbf{k}}_1,\tilde{\mathbf{k}}_2\\ \tilde{\mathbf{k}}_3,\tilde{\mathbf{k}}_4}} \delta(\epsilon_1 - \epsilon_{\mathbf{K}_1+\tilde{\mathbf{k}}_1})\delta(\epsilon_2 - \epsilon_{\mathbf{K}_2+\tilde{\mathbf{k}}_2}) \times$$
$$\delta(\epsilon_3 - \epsilon_{\mathbf{K}_3+\tilde{\mathbf{k}}_3})\delta(\epsilon_4 - \epsilon_{\mathbf{K}_4+\tilde{\mathbf{k}}_4})\,. \tag{3.13}$$

We now define the Fourier transforms of ρ and $\bar{\rho}$ with respect to the energy arguments, e.g.

$$\Psi(s, \mathbf{K}) = \int_{-\infty}^{\infty} \rho(\epsilon, \mathbf{K}) e^{is\epsilon} d\epsilon\,. \tag{3.14}$$

For the non-compact corrections, Eq. 3.14 defines $\Psi_{ncp}(s_1, \mathbf{K}_1; s_2, \mathbf{K}_2)$ and $\bar{\Psi}_{ncp}(s_1, \mathbf{K}_1; s_2, \mathbf{K}_2)$, respectively. In order to calculate the difference between Ψ and $\bar{\Psi}$ in finite dimensions, we expand the dispersions and exponentials as functions of $\tilde{\mathbf{k}}$ and keep the terms up to Δk^2. The difference $\delta\Psi_{ncp}$ for the non-compact diagrams becomes

$$\begin{aligned} \delta\Psi_{ncp}(s_1, \mathbf{K}_1; s_2, \mathbf{K}_2) &\approx \frac{t^2}{3}\Delta k^2 \times \\ &[\eta(\mathbf{K}_1 + \mathbf{K}_2) - \eta(\mathbf{K}_1 - \mathbf{K}_2)]\, s_1 s_2 \times \\ &\exp\left[i(s_1\epsilon_{\mathbf{K}_1} + s_2\epsilon_{\mathbf{K}_2})\right], \end{aligned} \tag{3.15}$$

where $\eta(\mathbf{K}) = 1/D\sum_n \cos(\mathbf{K}_n)$. Reversing the Fourier transform then yields for the difference of ρ_{ncp} and $\bar{\rho}_{ncp}$

$$\begin{aligned} \delta\rho_{ncp}(\epsilon_1, \mathbf{K}_1; \epsilon_2, \mathbf{K}_2) &\approx -\frac{t^2}{3}\Delta k^2 \times \\ &[\eta(\mathbf{K}_1 + \mathbf{K}_2) - \eta(\mathbf{K}_1 - \mathbf{K}_2)] \times \\ &\frac{\partial}{\partial\epsilon_1}\delta(\epsilon_1 - \epsilon_{\mathbf{K}_1})\frac{\partial}{\partial\epsilon_2}\delta(\epsilon_2 - \epsilon_{\mathbf{K}_2}). \end{aligned} \tag{3.16}$$

Eq. 3.16 demonstrates that the difference between coarse graining and not coarse graining in non-compact diagrams yields an error of order Δk^2. After tedious but straightforward calculation for the corresponding difference between coarse graining and not coarse graining in compact diagrams we obtain $\delta\rho_{cp} \sim \mathcal{O}(\Delta k^6)$. Since $\Delta k = 2\pi/L$, for large clusters this error becomes much smaller than the error in Eq. 3.16. To illustrate the above point we simulate a two–dimensional Hubbard model (with local interaction U and a nearest-neighbor hopping $t = 1$) using the Fluctuation Exchange Approximation (FLEX) [3, 28, 29]. In Fig. 3.4, the compact contribution of the thermodynamic potential difference constructed by coarse-grained Green functions is plotted versus $(\Delta k)^2 = 1/L^2$. The variation of $\Delta\Omega_{cp}$ over the entire $1/L^2$ range is about 1%. At very low temperatures ($T < 0.066$), some deviation from

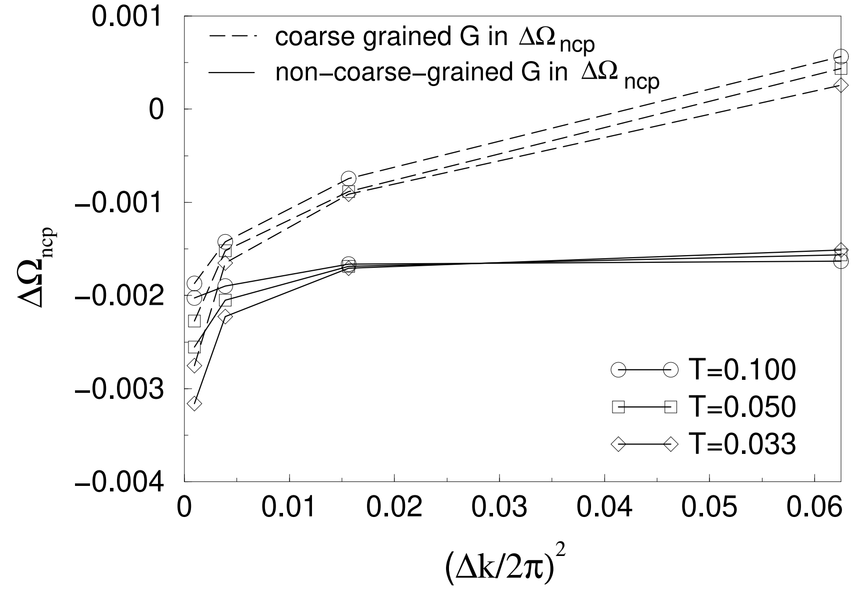

Figure 3.5: Non-compact contribution to the thermodynamic potential versus $(\Delta k)^2$ at $U/t = 1.57$ with and without coarse-grained Green functions. Using coarse-grained Green functions can result in a non-compact contribution with the wrong sign. (K. Aryanpour *et al.*, [3])

linearity is observed due to the correlation length exceeding the cluster size L and therefore the approximation of $\Sigma(k)$ by $\Sigma_{DCA}(K)$ begins to break down. Fig. 3.5 illustrates the non-compact contribution sketched versus $1/L^2$ using both coarse-grained and non-coarse-grained Green functions. Using non-coarse-grained Green functions, the variation of $\Delta\Omega_{ncp}$ over the entire $1/L^2$ range is roughly 30%. Coarse-graining the Green functions in these diagrams can even change the sign of this non-compact contributions, clearly indicating that coarse-graining the Green function is an unrealistic approximation for non-compact diagrams. However, one notices that for large cluster sizes the coarse-grained and non-coarse-grained results approach each other as the approximation to the infinite lattice becomes better.

3.4 Limit of Infinite Dimensions

To make contact with the original derivations of the DMFA [14,15], we explore the differences between the compact and non-compact graphs in the limit of many spatial dimensions, D. For $D \to \infty$, we calculate $\Delta\rho$ for both compact and non-compact diagrams by simply expanding Ψ and $\bar{\Psi}$ but this time with respect to $1/D$ instead of Δk^2. Letting $D \to \infty$ we can show that

$$\lim_{D\to\infty} \Psi_{ncp}(s_1, \mathbf{K}_1; s_2, \mathbf{K}_2) \approx \bar{\Psi}_{D\to\infty} \times \\ \exp(\frac{-\mathrm{t}^2}{12}\Delta \mathrm{k}^2[\eta(\mathbf{K}_2 - \mathbf{K}_1) - \eta(\mathbf{K}_1 + \mathbf{K}_2)]\mathrm{s}_1\mathrm{s}_2)\,, \tag{3.17}$$

Expanding the exponential in Eq. 3.17

$$\lim_{D\to\infty} \Psi_{ncp}(s_1, \mathbf{K}_1; s_2, \mathbf{K}_2) \approx \bar{\Psi}_{D\to\infty} \times \\ (1 - \frac{t^2}{12}\Delta k^2[\eta(\mathbf{K}_2 - \mathbf{K}_1) - \eta(\mathbf{K}_1 + \mathbf{K}_2)] \\ s_1 s_2 + \ldots)\,, \tag{3.18}$$

and consequently

$$\lim_{D\to\infty} \delta\rho_{ncp}(\epsilon_1, \mathbf{K}_1; \epsilon_2, \mathbf{K}_2) \approx \frac{t^2}{12}\Delta k^2 \times \\ [\eta(\mathbf{K}_2 - \mathbf{K}_1) - \eta(\mathbf{K}_1 + \mathbf{K}_2)]\frac{\partial}{\partial\epsilon_1}\frac{\partial}{\partial\epsilon_2} \\ \bar{\rho}_{D\to\infty}(\epsilon_1, \mathbf{K}_1; \epsilon_2, \mathbf{K}_2) + \mathcal{O}(\Delta k^4)\,. \tag{3.19}$$

However, for the difference in the compact diagrams as $D \to \infty$ we find $\lim_{D\to\infty} \delta\Psi_{cp} = 0$. Thus, for all Δk, there are non-local corrections to non-compact diagrams while there are none to compact diagrams as $D \to \infty$. This result is consistent with what Müller-Hartmann has shown for the DMFA [14]. Regardless of whether the expansion parameter is Δk or $1/D$, there is a fundamental difference between compact and non-compact diagrams which requires different treatments of each. Consequently, only the compact contributions should be formed from coarse-grained Green functions, whereas non-compact graphs should be inferred from the appropriate Dyson equation.

Even though we directly invoked the nearest neighbor hopping dispersion in our algorithm, our arguments can be generalized to other models assuming that the Green function falls off exponentially as $G(r) \sim e^{-r/r_s}$ where r_s is a characteristic length depending on dimensionality. The next section is devoted to this argument in real space.

The arguments made here may also be applied to the DMFA simply by taking $N_c = 1$. They also may be extended to other cluster approaches, such as the Molecular Coherent Potential Approximation [41] and its formal equivalent for dynamical systems, the Molecular Cluster Dynamical Mean Field [19].

3.5 Real space approach

Thus far in this chapter for the Hubbard model in particular, we have shown both analytically and numerically that the error produced by coarse-graining the non-compact diagrams is significantly larger than the error produced by coarse-graining the compact ones. Here, we would like to give a more general argument in real space. We wish to emphasize two points in this new approach. First, since the derivation of the DCA in this section relies only upon the exponential fall off of the Green function as a function of distance, it is far more intuitive than the momentum space argument in previous sections of this chapter (also c.f. Ref. [2]). Second, it ties the derivation of the DCA to the original derivation of the DMFA in the limit of infinite dimensions, where similar arguments are employed. [15]

The exponential fall off behavior occurs naturally in high dimensions. In the tight-binding Hamiltonian (c.f. Eq. 2.2), the factor t corresponds to the hopping of electrons among nearest neighboring sites. Thus, one could show that the real space Green function $G(r)$ (we drop the frequency label from this point on for simplicity) for r nearest neighbor hops is proportional to $G(r) \sim t^r$ as $t \to 0$. On the other hand, Metzner *et al.*, and Müller-Hartmann [**?**,15] have shown that in D dimensions, the factor t should be renormalized as $t/\sqrt{D}$ in order to have a finite density of states width as $D \to \infty$. As a result of this renormalization

$$G(r) \sim t^r \sim (1/\sqrt{D})^r \sim D^{-r/2} = e^{-r/r_s}$$
$$r_s = \frac{2}{lnD}, \tag{3.20}$$

meaning that $G(r)$ falls off exponentially as a function of r.

In the DCA, we attempt to minimize the error due to coarse-graining the Green function (and potentials) in the Feynman diagrams. Consider the first non-trivial correction to the coarse-grained non-compact diagrams generated by replacing the explicit coarse-grained Green function lines by the non-coarse-grained ones as illustrated in Fig. 3.2

$$\delta^{(1)}[\Delta\Omega_{ncp}] \sim \frac{1}{N}\sum_{\mathbf{k}} \sigma(\mathbf{K})\sigma'(\mathbf{K})G(\mathbf{k})^2 - \frac{1}{N_c}\sum_{\mathbf{K}}$$
$$\sigma(\mathbf{K})\sigma'(\mathbf{K})\bar{G}(\mathbf{K})^2, \tag{3.21}$$

where $\mathbf{K}$ are the coarse-graining cells momenta and $\mathbf{k} = \mathbf{K} + \tilde{\mathbf{k}}$ include all the momenta in the first Brillouin zone shown in Fig. 1.2. In this derivation we also presume that the self-energy is $\tilde{\mathbf{k}}$ independent and the entire $\tilde{\mathbf{k}}$ dependence is embedded in the Green functions. By breaking up the sums over $\mathbf{k}$ in Eq. 3.21 into $\mathbf{K}$ and $\tilde{\mathbf{k}}$ sums and writing all the G in terms of their Fourier transforms at the same time we get

$$\delta^{(1)}[\Delta\Omega_{ncp}] \sim \frac{1}{N}\sum_{\tilde{\mathbf{k}},\mathbf{K}} \sigma(\mathbf{K})\sigma'(\mathbf{K}) \sum_{\mathbf{x}_1,\mathbf{x}_2} G(\mathbf{x}_1)G(\mathbf{x}_2) \times$$
$$e^{-i\tilde{\mathbf{k}}\cdot(\mathbf{x}_1+\mathbf{x}_2)}e^{-i\mathbf{K}\cdot(\mathbf{x}_1+\mathbf{x}_2)} - \frac{N_c}{N^2}\sum_{\mathbf{K},\tilde{\mathbf{k}}_1,\tilde{\mathbf{k}}_2} \sigma(\mathbf{K})\sigma'(\mathbf{K}) \times$$

$$\sum_{\mathbf{x}_1,\mathbf{x}_2} G(\mathbf{x}_1)G(\mathbf{x}_2)e^{-i\tilde{\mathbf{k}}_1\cdot\mathbf{x}_1}e^{-i\tilde{\mathbf{k}}_2\cdot\mathbf{x}_2}e^{-i\mathbf{K}\cdot(\mathbf{x}_1+\mathbf{x}_2)}\,, \tag{3.22}$$

in which we used Eq. 3.5 for $\bar{G}(\mathbf{K})$. According to Fig. 1.2, we can split $\mathbf{x} = \mathbf{X} + \tilde{\mathbf{x}}$ where $\tilde{\mathbf{x}}$ extend between two separate clusters while $\mathbf{X}$ always remain within a single cluster. By making this separation in Eq. 3.22 one picks up phases including products of $-i\mathbf{K}\cdot\mathbf{X}$, $-i\mathbf{K}\cdot\tilde{\mathbf{x}}$, $-i\tilde{\mathbf{k}}\cdot\mathbf{X}$ and $-i\tilde{\mathbf{k}}\cdot\tilde{\mathbf{x}}$ in their exponents. The phase associated with the product $\mathbf{K}\cdot\tilde{\mathbf{x}} = 2n\pi$ with n an integer equals unity. The phases involving $-i\tilde{\mathbf{k}}\cdot\mathbf{X}$ products are also neglected as discussed in section 1.3. Hence, Eq. 3.22 can be rewritten as follows

$$\begin{aligned}
&\delta^{(1)}[\Delta\Omega_{ncp}] \sim \frac{1}{N}\sum_{\mathbf{K}}\sigma(\mathbf{K})\sigma'(\mathbf{K})\sum_{\mathbf{X}_1,\mathbf{X}_2}\sum_{\tilde{\mathbf{x}}_1,\tilde{\mathbf{x}}_2} G(\mathbf{X}_1+\tilde{\mathbf{x}}_1)\times \\
&\mathbf{G}(\mathbf{X}_2+\tilde{\mathbf{x}}_2)e^{-i\mathbf{K}\cdot(\mathbf{X}_1+\mathbf{X}_2)}\sum_{\tilde{\mathbf{k}}} e^{-i\tilde{\mathbf{k}}\cdot(\tilde{\mathbf{x}}_1+\tilde{\mathbf{x}}_2)} - \frac{N_c}{N^2}\sum_{\mathbf{K}}\sigma(\mathbf{K})\times \\
&\sigma'(\mathbf{K})\sum_{\mathbf{X}_1,\mathbf{X}_2}\sum_{\tilde{\mathbf{x}}_1,\tilde{\mathbf{x}}_2} G(\mathbf{X}_1+\tilde{\mathbf{x}}_1)\mathbf{G}(\mathbf{X}_2+\tilde{\mathbf{x}}_2)e^{-i\mathbf{K}\cdot(\mathbf{X}_1+\mathbf{X}_2)}\times \\
&\sum_{\tilde{\mathbf{k}}_1,\tilde{\mathbf{k}}_2} e^{-i\tilde{\mathbf{k}}_1\cdot\mathbf{x}_1}e^{-i\tilde{\mathbf{k}}_2\cdot\mathbf{x}_2}\,.
\end{aligned} \tag{3.23}$$

Implementing the following substitutions

$$\begin{aligned}
&\sum_{\tilde{\mathbf{k}}} e^{-i\tilde{\mathbf{k}}\cdot(\tilde{\mathbf{x}}_1+\tilde{\mathbf{x}}_2)} = \frac{N}{N_c}\delta_{\tilde{\mathbf{x}}_1,-\tilde{\mathbf{x}}_2} \quad \text{and} \quad \sum_{\tilde{\mathbf{k}}_1,\tilde{\mathbf{k}}_2} e^{-i\tilde{\mathbf{k}}_1\cdot\mathbf{x}_1}e^{-i\tilde{\mathbf{k}}_2\cdot\mathbf{x}_2} \\
&= (\frac{N}{N_c})^2\delta_{\tilde{\mathbf{x}}_1,0}\delta_{\tilde{\mathbf{x}}_2,0}\,,
\end{aligned} \tag{3.24}$$

Eq. 3.23 simplifies into

$$\begin{aligned}
&\delta^{(1)}[\Delta\Omega_{ncp}] \sim \frac{1}{N_c}\sum_{\mathbf{K}}\sigma(\mathbf{K})\sigma'(\mathbf{K})[\sum_{\mathbf{X}_1,\mathbf{X}_2,\tilde{\mathbf{x}}} G(\mathbf{X}_1+\tilde{\mathbf{x}})\times \\
&\mathbf{G}(\mathbf{X}_2-\tilde{\mathbf{x}})e^{-i\mathbf{K}\cdot(\mathbf{X}_1+\mathbf{X}_2)} - \sum_{\mathbf{X}_1,\mathbf{X}_2} G(\mathbf{X}_1)\mathbf{G}(\mathbf{X}_2)\times \\
&e^{-i\mathbf{K}\cdot(\mathbf{X}_1+\mathbf{X}_2)}]\,.
\end{aligned} \tag{3.25}$$

Setting $\sigma(\mathbf{K})\sigma'(\mathbf{K}) = \xi(\mathbf{K})$ and performing the $\mathbf{K}$ summation

$$\delta^{(1)}[\Delta\Omega_{ncp}] \sim \sum_{\mathbf{X}_1,\mathbf{X}_2} \xi(\mathbf{X}_1+\mathbf{X}_2)[\sum_{\tilde{\mathbf{x}}} G(\mathbf{X}_1+\tilde{\mathbf{x}}) \times$$
$$\mathbf{G}(\mathbf{X}_2-\tilde{\mathbf{x}}) - G(\mathbf{X}_1)\mathbf{G}(\mathbf{X}_2)] = \sum_{\mathbf{X}_1,\mathbf{X}_2} \xi(\mathbf{X}_1+\mathbf{X}_2) \times$$
$$\sum_{\tilde{\mathbf{x}}\neq 0} G(\mathbf{X}_1+\tilde{\mathbf{x}})\mathbf{G}(\mathbf{X}_2-\tilde{\mathbf{x}})\,. \tag{3.26}$$

Knowing that $\xi(\mathbf{X}_1+\mathbf{X}_2) = \sum_{\mathbf{X}} \sigma(\mathbf{X})\sigma'(\mathbf{X}+\mathbf{X}_1+\mathbf{X}_2)$ and also that the lowest order of $\sigma(\mathbf{X}) \sim G^3(\mathbf{X}) \sim e^{-3|\mathbf{X}|/r_s}$ we conclude that in Eq. 3.26, the largest contribution is due to terms having $\mathbf{X}_1 = -\mathbf{X}_2$ or in other words, local ξ. As shown in Fig. 3.6, the first term in the $\tilde{\mathbf{x}}$ sum corresponds to $|\tilde{\mathbf{x}}| = L$ (size of the cluster) and $\mathbf{X}$ can be as large as $\mathbf{X} = -(L-1)$ in the opposite direction. Hence, the leading order term in Eq. 3.26 falls off as

$$\delta^{(1)}[\Delta\Omega_{ncp}] \sim \xi(0) \times 2D \times G(L-(L-1)) \times$$
$$G(-L+(L-1)) \sim 2D\xi(0)e^{\frac{-1}{r_s}}e^{\frac{-1}{r_s}} = 2D\xi(0)e^{\frac{-2}{r_s}}\,, \tag{3.27}$$

where $2D$ is the number of $|\tilde{\mathbf{x}}| = L$ contributions in D different dimensions of a D dimensional cubic lattice. In Eq. 3.27 we also used the fact that due to the lattice symmetry, $G(-\mathbf{X}) = G(\mathbf{X})$. As $D \to \infty$, using $r_s = 2/lnD$

$$\delta^{(1)}[\Delta\Omega_{ncp}] \sim 2D\xi(0)e^{-lnD} = 2\xi(0)DD^{-1} \sim \mathcal{O}(1)\,. \tag{3.28}$$

which indicates the existence of non-local corrections to the non-compact contribution of the thermodynamic potential even at infinite dimensions. Now we replace the coarse-grained self-energy bubbles in Fig. 3.2 with coarse-grained vertices having four external legs and look at the difference between compact diagrams with and without coarse-grained Green functions which are explicitly shown in the figure. Since we earlier dropped the frequency labels in the Green functions, here we use indices 1, 2, 3 and 4 to emphasize that these Green

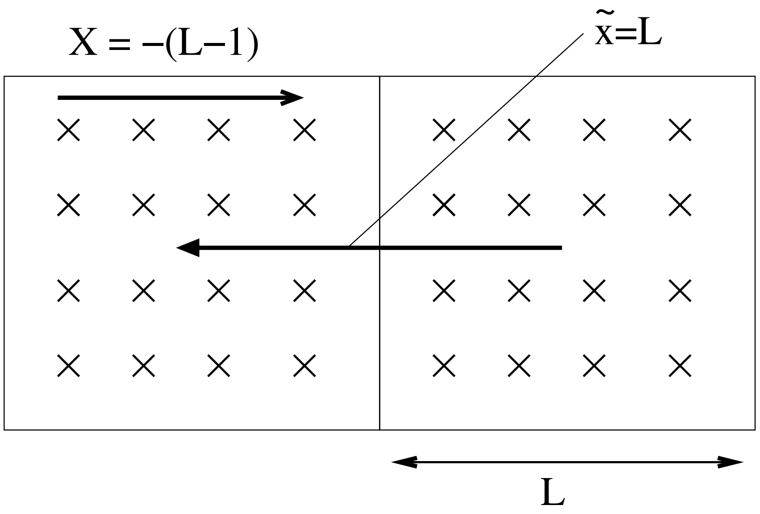

Figure 3.6: *Two adjacent clusters with their* $\mathbf{X}$ *and* $\tilde{\mathbf{x}}$ *vectors.(K. Aryanpour et al., [3])*

functions have different frequency labels. The first correction to the compact contribution of the thermodynamic potential depicted in Fig. 3.3 is

$$\begin{aligned}
&\delta^{(1)}[\Delta\Omega_{cp}] \sim \frac{1}{N^3}\sum_{\substack{\mathbf{k}_1,\mathbf{k}_2\\ \mathbf{q}}} \Gamma(\mathbf{K}_1,\mathbf{K}_2,\mathbf{Q})\Gamma'(\mathbf{K}_1,\mathbf{K}_2,\mathbf{Q})G_1(\mathbf{k}_1)\times \\
&G_2(\mathbf{k}_2)G_3(\mathbf{q})G_4(\mathbf{k}_1+\mathbf{k}_2-\mathbf{q}) - \frac{1}{N_c^3}\sum_{\substack{\mathbf{K}_1,\mathbf{K}_2\\ \mathbf{Q}}} \Gamma(\mathbf{K}_1,\mathbf{K}_2,\mathbf{Q})\times \\
&\Gamma'(\mathbf{K}_1,\mathbf{K}_2,\mathbf{Q})\bar{G}_1(\mathbf{K}_1)\bar{G}_2(\mathbf{K}_2)\bar{G}_3(\mathbf{Q})\bar{G}_4(\mathbf{K}_1+\mathbf{K}_2-\mathbf{Q}),
\end{aligned} \tag{3.29}$$

where similar to Eq. 3.21, all the vertices are coarse-grained but the Green functions are not. Following the same procedure as for the non-compact difference we arrive at

$$\begin{aligned}
&\delta^{(1)}[\Delta\Omega_{cp}] \sim \sum_{\substack{\mathbf{X}_1,\mathbf{X}_2\\ \mathbf{X}_3,\mathbf{X}_4}} \Lambda(\mathbf{X}_1+\mathbf{X}_4,\mathbf{X}_2+\mathbf{X}_4,\mathbf{X}_3-\mathbf{X}_4)\times \\
&[\sum_{\tilde{\mathbf{x}}} G_1(\mathbf{X}_1-\tilde{\mathbf{x}})G_2(\mathbf{X}_2-\tilde{\mathbf{x}})G_3(\mathbf{X}_3+\tilde{\mathbf{x}})G_4(\mathbf{X}_4+\tilde{\mathbf{x}}) -
\end{aligned}$$

$$G_1(\mathbf{X}_1)G_2(\mathbf{X}_2)G_3(\mathbf{X}_3)G_4(\mathbf{X}_4)]\,, \tag{3.30}$$

where

$$\begin{aligned}
&\Lambda(\mathbf{X}_1+\mathbf{X}_4,\mathbf{X}_2+\mathbf{X}_4,\mathbf{X}_3-\mathbf{X}_4) = \frac{1}{N_c^3}\sum_{\substack{\mathbf{K}_1,\mathbf{K}_2\\ \mathbf{Q}}}\Gamma(\mathbf{K}_1,\mathbf{K}_2,\mathbf{Q})\times \\
&\Gamma'(\mathbf{K}_1,\mathbf{K}_2,\mathbf{Q})e^{-i\mathbf{K}_1\cdot(\mathbf{X}_1+\mathbf{X}_4)}e^{-i\mathbf{K}_2\cdot(\mathbf{X}_2+\mathbf{X}_4)}e^{-i\mathbf{Q}\cdot(\mathbf{X}_3-\mathbf{X}_4)} = \\
&\sum_{\substack{\mathbf{X},\mathbf{X}'\\ \mathbf{X}''}}\Gamma(\mathbf{X},\mathbf{X}',\mathbf{X}'')\times \\
&\Gamma'(\mathbf{X}+\mathbf{X}_1+\mathbf{X}_4,\mathbf{X}'+\mathbf{X}_2+\mathbf{X}_4,\mathbf{X}''+\mathbf{X}_3-\mathbf{X}_4)\,.
\end{aligned} \tag{3.31}$$

Once again, the largest contribution is associated with local Λ, i.e., $\mathbf{X}_1 = -\mathbf{X}_4$, $\mathbf{X}_2 = -\mathbf{X}_4$ and $\mathbf{X}_3 = \mathbf{X}_4$. Therefore

$$\begin{aligned}
\delta^{(1)}[\Delta\Omega_{cp}] &\sim \sum_{\mathbf{X}}\Lambda(0)[\sum_{\tilde{\mathbf{x}}}G_1(-\mathbf{X}-\tilde{\mathbf{x}})G_2(-\mathbf{X}-\tilde{\mathbf{x}})\times \\
&G_3(\mathbf{X}+\tilde{\mathbf{x}})G_4(\mathbf{X}+\tilde{\mathbf{x}}) - G_1(\mathbf{X})G_2(\mathbf{X})G_3(\mathbf{X})G_4(\mathbf{X})] = \\
&\Lambda(0)\sum_{\mathbf{X},\tilde{\mathbf{x}}\neq 0}G_1(\mathbf{X}+\tilde{\mathbf{x}})G_2(\mathbf{X}+\tilde{\mathbf{x}})G_3(\mathbf{X}+\tilde{\mathbf{x}})G_4(\mathbf{X}+\tilde{\mathbf{x}})\,.
\end{aligned} \tag{3.32}$$

Considering $|\tilde{\mathbf{x}}| = L$ and $\mathbf{X}_{min} = -(L-1)$

$$\begin{aligned}
&\delta^{(1)}[\Delta\Omega_{cp}] \sim \Lambda(0)\times 2D\times G_1(-L+(L-1))\times \\
&G_2(-L+(L-1))G_3(L-(L-1))G_4(L-(L-1)) = \\
&2D\Lambda(0)e^{\frac{-4}{r_S}} = 2\Lambda(0)D^{-1}\,, \qquad (r_s = \frac{2}{lnD})
\end{aligned} \tag{3.33}$$

which vanishes as $D \to \infty$.

Comparing Eq. 3.33 with Eq. 3.28 shows that the first correction to the compact contribution of the thermodynamic potential falls off exponentially twice as fast as the equivalent correction in the non-compact contribution. In addition, even at the infinite dimensional limit, there are corrections of order one to the non-compact contribution whereas for the compact diagrams the DCA becomes exact and there are no corrections. This justifies coarse-graining only in the compact diagrams. The Green functions in the non-compact diagrams have to be explicitly constructed from the coarse-grained self-energy $\Sigma_{DCA}(\mathbf{K}, \omega_n)$ using Eq. 3.6.

3.6 Summary

We justify one of the central underlying approximations of the dynamical cluster approximation. We both analytically and numerically demonstrate that coarse graining the Green functions in non-compact diagrams results in a larger amount of error compared to that incurred in compact diagrams. Consequently, non-compact diagrams and their contribution to the thermodynamic potential are not coarse-grained. The distinction between non-compact and compact diagrams persists even in the limit of infinite dimensions. This concurs with previous work on dynamical mean field theory and has implications for other cluster approaches.

Chapter 4

The dynamical cluster approximation (DCA) versus the cellular dynamical mean field theory (CDMFT) in strongly correlated electron systems

4.1 Introduction

The DCA [16, 25] and the CDMFT [19] are both approximation methods incorporating the non-local correlations in the correlated electron systems relinquished by fully local techniques such as the Dynamical Mean Field Approximation (DMFA) [14, 15, 37, 38] and the Coherent Potential Approximation (CPA). [42–44] The DCA is formulated in the momentum space by dividing the first Brillouin zone in a number of subcells with periodic boundary conditions within which the momentum conservation is relinquished but is conserved between any two of them whereas the CDMFT is formulated in the real space by dividing the real lattice into clusters with open boundary conditions.

It has been shown [22] that due to the periodic (open) boundary conditions, the DCA (CDMFT) converges with corrections of $\mathcal{O}(1/L_c^2)$ ($\mathcal{O}(1/L_c)$) with L_c the linear size of the cluster. Hence, for large enough L_c, one would expect the DCA to converge more quickly than the CDMFT to the exact results.

In this work, a toy model called *the simplified one-dimensional large-N model*, first introduced and studied by I. Affleck *et al.* [21], is employed to demonstrate the convergence comparison between the DCA and CDMFT. This model has a mean filed solution which becomes exact as one approaches the thermodynamic limit. We study the convergence of the DCA and CDMFT towards the exact results for this model and conclude that for large enough cluster sizes the DCA converges much faster than the CDMFT. The DCA also requires much less CPU time than the CDMFT for large L_c calculations.

4.2 General considerations

The *simplified one-dimensional large-N model* Hamiltonian reads

$$
\begin{aligned}
H = & -t \sum_{i,\sigma} (f^{\dagger}_{i,\sigma} f_{i+1,\sigma} + f^{\dagger}_{i+1,\sigma} f_{i,\sigma}) \\
& + \frac{J}{2N} \sum_{i,\sigma,\sigma'} (f^{\dagger}_{i,\sigma} f_{i,\sigma'} f^{\dagger}_{i+1,\sigma'} f_{i+1,\sigma} \\
& + f^{\dagger}_{i+1,\sigma} f_{i+1,\sigma'} f^{\dagger}_{i,\sigma'} f_{i,\sigma}) \,,
\end{aligned}
\tag{4.1}
$$

where $i = 1, ..., L$ and $\sigma = 1, ..., N$. This model is the extension of the Hubbard-Heisenberg model with SU(2) spins replaced by SU(N) ones. Taking the large L and N limit the quantity $\chi = (1/N) \sum_{\sigma} f^{\dagger}_{i,\sigma}(t) f_{i+1,\sigma}(t)$ does not fluctuate. By the substitution of χ with its mean field average and also setting $J = 1$, we rescale the hopping term $t \to t/J$ and the Hamiltonian reduces to a non-interacting one with a renormalized $t \to t + \chi$. We arrive at the following self-consistent equations for χ

$$\chi = \frac{1}{L}\sum_k f(\beta E_k)cosk, \qquad E_k = -2(t+\chi)cosk + \mu\,, \tag{4.2}$$

with μ the chemical potential, $f(\beta E_k)$ the Fermi function and β the inverse temperature.

In the DCA, the first Brillouin zone in the momentum space is divided into L_c subcells with the linear size of $\Delta k = 2\pi/L_c$ (c.f. Fig. 1.2 (left) for a square lattice). The self-energy part in Eq. 4.2, namely

$$\Sigma(k) = -2\ \chi\ cosk\,, \tag{4.3}$$

is replaced by its DCA counterpart

$$\Sigma_{DCA}(\mathbf{K}_c) = -4\frac{\chi_{cl}^{DCA}}{\Delta k}sin(\Delta k/2)cos(\mathbf{K}_c)\,, \tag{4.4}$$

in which $\chi_{cl}^{DCA} = (1/N)\sum_\sigma f^\dagger_{i,\sigma}(t)f_{i+1,\sigma}(t)$ with i and $i+1$ belonging to the same cluster and $cosk$ in Eq. 4.3 is replaced by

$$\frac{2}{\Delta k}sin(\Delta k/2)cos(\mathbf{K}_c) = \frac{L_c}{L}\sum_{\tilde{\mathbf{k}}} cos(\mathbf{K}_c + \tilde{\mathbf{k}})\,, \tag{4.5}$$

with $\mathbf{K}_c$ the cluster momenta and $\tilde{\mathbf{k}}$ the momenta within each subcell which are coarse-grained over (c.f. Fig. 1.2 (left) for a square lattice). Consequently, the self-consistent equations for χ_{cl}^{DCA} are

$$\begin{aligned}
\chi_{cl}^{DCA} &= \frac{1}{L_c}\sum_{\mathbf{K}_c}\frac{2}{\Delta k}sin(\Delta k/2)cos(\mathbf{K}_c)\bar{f}(\beta E(\mathbf{K}_c)),\\
\bar{f}(\beta E(\mathbf{K}_c)) &= \frac{L_c}{L}\sum_{\tilde{\mathbf{k}}} f(\beta E_{\mathbf{K}_c+\tilde{\mathbf{k}}}),\\
E_{\mathbf{K}_c+\tilde{\mathbf{k}}} &= -2\ t\ cos(\mathbf{K}_c+\tilde{\mathbf{k}}) - 4\frac{\chi_{cl}^{DCA}}{\Delta k}sin(\Delta k/2)cos(\mathbf{K}_c)\\
&\qquad +\mu\,.
\end{aligned} \tag{4.6}$$

One notes that in Eq. 4.6, both $f(\beta E_k)$ and $cosk$ in Eq. 4.2 have been replaced by their coarse-grained equivalents and the summation runs over only the cluster momenta $\mathbf{K}_c$ rather than the entire first Brillouin zone in Eq. 4.2.

After self-consistency is achieved, one can use the cluster quantity χ_{cl}^{DCA} to compute its lattice counterpart

$$\chi_{latt}^{DCA} = \frac{1}{L}\sum_k f(\beta E_{K_c+\tilde{\mathbf{k}}}) \cos k \,. \tag{4.7}$$

In the CDMFT, the real space lattice is divided into L_c clusters (c.f. Fig. 1.2 (right) for a square lattice). Considering that $(\chi_{cl}^{CDMFT})_i = (1/N)\sum_\sigma f^\dagger_{i,\sigma}(t) f_{i+1,\sigma}(t)$ does not fluctuate, we can obtain the cluster self-energy as $(\Sigma_c)_{i,j} = (\chi_{cl}^{CDMFT})_i \delta_{i,j-1} + (\chi_{cl}^{CDMFT})_j \delta_{i,j+1}$. The fact that both $(\chi_{cl}^{CDMFT})_i$ and $(\Sigma_c)_{i,j}$ depend upon the site labels is due to the open boundary conditions on the clusters in the real lattice. In the Hamiltonian in Eq. 4.1, the non-interacting part can be represented as a so called *t- matrix* defined by

$$\begin{aligned}
\hat{t}(\tilde{\mathbf{k}})_{i,j} &= \hat{t}(\mathbf{X}_i - \mathbf{X}_j, \tilde{\mathbf{k}}) = \frac{1}{L_c}\sum_{\mathbf{K}_c} e^{i(\mathbf{K}_c+\tilde{\mathbf{k}})(\mathbf{X}_i-\mathbf{X}_j)} \epsilon_{\mathbf{K}_c+\tilde{\mathbf{k}}}, \\
\epsilon_{\mathbf{K}_c+\tilde{\mathbf{k}}} &= -2\ t\ cos(\mathbf{K}_c + \tilde{\mathbf{k}})\,,
\end{aligned} \tag{4.8}$$

with $\mathbf{X}_i$ and $\mathbf{X}_j$ the intercluster positions (c.f. Fig. 1.2 (right) for a square lattice). The t-matrix is the Fourier transform of the hopping energy dispersion at a certain $\tilde{\mathbf{k}}$ between every two points inside the real lattice cluster. Having $\psi_i^\nu(\tilde{\mathbf{k}})$ and $\lambda^\nu(\tilde{\mathbf{k}})$ $(\nu = 1, ..., L_c)$ the eigenstates and the eigenvalues of the matrix $\hat{t} + \hat{\Sigma}$ respectively, we can calculate the cluster Green function as

$$(G_c)_{i,j} = \frac{L_c}{L}\sum_{\tilde{\mathbf{k}},\nu} \psi_i^\nu(\tilde{\mathbf{k}})(\psi_j^\nu(\tilde{\mathbf{k}}))^* \frac{1}{i\omega_n + \mu - \lambda^\nu(\tilde{\mathbf{k}})}\,. \tag{4.9}$$

Using the above relation, the self-consistent equations for $(\chi_{cl}^{CDMFT})_i$ are

$$(\chi_{cl}^{CDMFT})_i = \frac{L_c}{L} \sum_{\tilde{\mathbf{k}},\nu} \psi_i^{\nu}(\tilde{\mathbf{k}})(\psi_{i+1}^{\nu}(\tilde{\mathbf{k}}))^* f(\beta E_{\tilde{\mathbf{k}},\nu}),$$
$$E_{\tilde{\mathbf{k}},\nu} = \mu - \lambda^{\nu}(\tilde{\mathbf{k}})\,. \tag{4.10}$$

As the above derivations illustrate, in the DCA, coarse-graining the momentum space maps the lattice problem onto a cluster in **k**-space. The corresponding cluster in real space is fictitious and has no physical meaning. Consequently, only local quantities are identical for the cluster and lattice. Non-local cluster quantities like χ_{cl}^{DCA} are not identical to their corresponding lattice quantities and thus have no physical meaning. In the CDMFT, the cluster is defined in real space and the coarse-grained Green function differs from the CDMFT lattice Green function only in the neglect of phase-factors corresponding to the position of the cluster in the lattice. Thus, the two quantities are identical for distances inside the cluster and as a result, $\chi_{latt}^{CDMFT} \approx \chi_{cl}^{CDMFT}$.

By numerically solving self-consistent Eq. 4.2, 4.6 and 4.10, we can make a comparison between the exact solution and the predictions by the DCA and the CDMFT.

4.3 Results

In Fig. 4.1, χ has been plotted versus β for $t = 1$ and fixed filling of $n = 0.37$ ($\mu \approx 1$) using the DCA and CDMFT for $L_c = 2, 4, 8$ and 16 respectively. It is more physical to do the calculations at fixed filling n instead of fixed chemical potential μ. As illustrated, it is clear that the DCA results converge faster than the CDMFT ones to the exact solution even for small L_c. The CDMFT results converge consistently whereas for small L_c ($L_c = 8$ in particular) the DCA results fluctuate around the exact solution. Nevertheless, at large enough L_c, the DCA behaves consistently and converges from below. Odd cluster sizes have

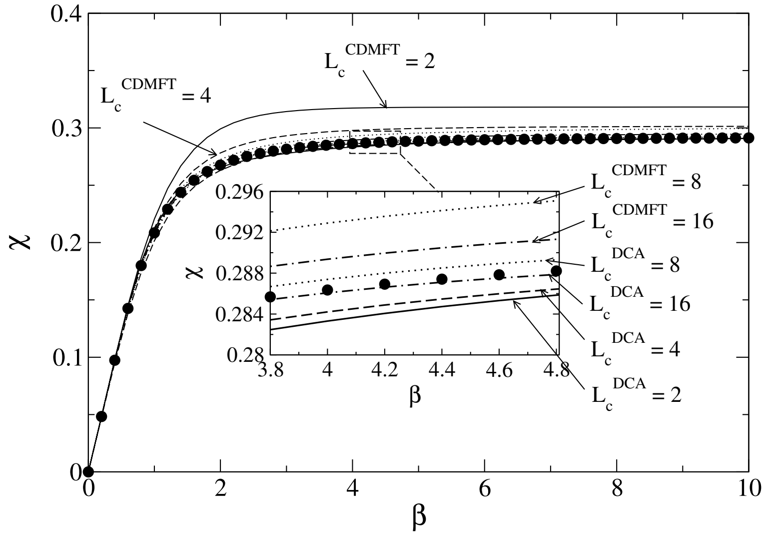

Figure 4.1: χ as a function of β (inverse temperature) at $t = 1$ and filling $n = 0.37$ ($\mu \approx 1$) for both the DCA and the CDMFT at $L_c = 2, 4, 8, 16$. The exact result is represented bu the solid circles. (K. Aryanpour *et al.*, [4])

been avoided in these calculations because for the DCA, the periodic boundary conditions on the cluster suppress $Q = \pi$ fluctuations by frustrating the cluster.

In Fig. 4.2, χ has been plotted as a function of the inverse cluster size $1/L_c$ computed by the DCA and the CDMFT at fixed inverse temperature $\beta = 5$ for $t = 1$ and $n = 0.37$ ($\mu \approx 1$) and compare the results with the exact solution (solid line). The DCA begins to converge quadratically and the CDMFT linearly in $1/L_c$ to the exact solution beyond $L_c = 32$ and $L_c = 10$ respectively (the fits in the insets). The scaling behavior of both the DCA and CDMFT at large enough L_c are consistent with previous results in Ref. [22].

It is noteworthy that for this Hamiltonian in particular, the values of L_c beyond which the scaling behaviors of the DCA and the CDMFT are observed are relatively high. E.g., in the one dimensional Falicov-Kimball model at half filling, these scaling behaviors are manifest beyond $L_c = 2$. [22]

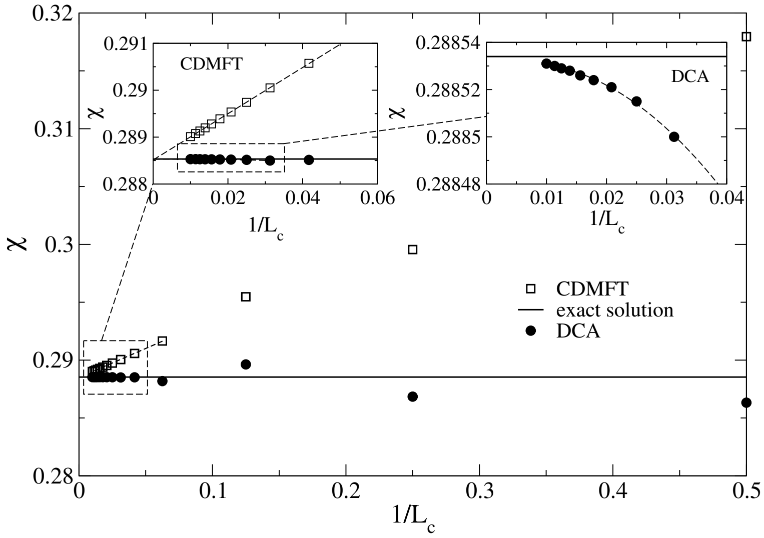

Figure 4.2: χ as a function of $1/L_c$ at $\beta = 5$, $t = 1$ and filling $n = 0.37$ ($\mu \approx 1$). The insets show the convergence of the DCA (filled circles) and CDMFT (open squares) results to the exact solution (solid line) beyond $L_c = 16$ for the CDMFT and $L_c = 32$ for the DCA. The dashed lines in the insets represent the linear and quadratic fits in $1/L_c$ to the CDMFT and DCA results respectively. (K. Aryanpour *et al.*, [4])

4.4 Summary

The results in both Figs. 4.1 and 4.2 indicate the superiority of the DCA over the CDMFT in terms of faster convergence with the cluster size L_c. The DCA also significantly reduces the computational CPU time compared to the CDMFT. In the CDMFT, because of the open boundary conditions on the cluster, the Green function in both real and momentum spaces is not diagonal. Thus, expensive diagonalizations of large matrices are required for large cluster sizes.

Another significant difference between these two techniques appears in the calculation of the self-energy. The DCA approximates the lattice self-energy by a constant within a DCA subcell in momentum space and as a result, the self-energy becomes a step function in k-space. Thus, one may use an approach such as the Akima spline which is the smoothest curve interpolating through these step functions to generate an analytic form for the self-energy. Using the Akima spline is consistent with the assumption that the self-energy is a smoothly varying function in momentum space. In the CDMFT, since the lattice self-energy is approximated by the cluster self-energy in real space, its Fourier transform to momentum space yields a smooth self-energy curve. Due to the open boundary conditions of the cluster, the translational invariance is violated and the self-energy in momentum space is not diagonal. Nevertheless, by using the *Random Phase Approximation* (RPA), [45] the translational invariance can be restored and the self-energy becomes a diagonal function in momentum space.

Chapter 5

Magnetism in semiconductors: A dynamical mean field study of ferromagnetism in $Ga_{1-x}Mn_xAs$

5.1 Introduction

Ferromagnetic semiconductors have recently drawn significant attention as they may form the basis of a newly developed area in both physics and industry called *spintronics*. In spintronics, the spin degree of freedom of charge carriers (electrons or holes) is used to carry information in addition to the charge. Ferromagnetic semiconductors are a good source of polarized holes. However, most semiconductors are very resistant to the solution of magnetic impurities. Recently, the *molecular-beam epitaxy* technique, [9,46] led to a successful growth of $Ga_{1-x}Mn_xAs$.

The valence band of GaAs is p-like, so the spin-orbit coupling is strong. G. Zaránd and B. Jankó [10] recently employed a model for $Ga_{1-x}Mn_xAs$ that incorporates the spin-orbit coupling effect in the band structure of pure GaAs along with the interaction between valence band holes and Mn impurity spins. This model is derived by simplifying a more general Hamiltonian for zinc-blende semiconductors first introduced by Kohn and Luttinger. [11, 47, 48] The strong spin-orbit coupling effect for valence holes is introduced by quantizing their spins along the direction of their momenta. In this *chiral basis* the non-interacting part of the Hamiltonian gains a very simple diagonal form at the cost of complicating the impurity-hole interaction term. Based upon a perturbative approach (RKKY), G. Zaránd and B. Jankó find that $Ga_{1-x}Mn_xAs$ is a *frustrated* ferromagnet exhibiting features similar to spin glasses and spin ice compounds.

In this chapter the Dynamical Mean Field Approximation (DMFA) [13–15, 37] is utilized to perform a systematic analysis of this model. A self-consistent mean field formalism is presented first to take advantage of the simplicity of the non-interacting (interacting) part of the Hamiltonian in the chiral (non-chiral) basis. This formalism is then employed to compute the magnetization for Mn impurities and thereby the ferromagnetic phase transition temperature T_c will be obtained for different values of impurity-hole coupling J_c, the concentration of Mn impurities $\mathbf{x}$ and valence carrier concentration n_h. The polarization of valence hole spins versus temperature will also be studied along with the magnetic phase diagram for $Ga_{1-x}Mn_xAs$ with respect to the impurity concentration, valence carrier concentration and temperature. The ultimate objective is to study the effect of chirality for this model and inspect the conclusions drawn by Zaránd and Jankó using a more systematic technique, i.e, the DMFA. This task is implemented by comparing the results of the chiral Hamiltonian with those for a single band Hamiltonian in which the chirality has been switched off.

5.2 Formalism

The simplified Kohn-Luttinger Hamiltonian in the non-chiral basis reads:

$$H = H_0 + \sum_{R_i} H_{int}(R_i)\,. \tag{5.1}$$

In Eq.5.1, H_0 includes the electronic (or in this case holonic) dispersion plus a spin-orbit coupling term, both taken from the band structure of pure GaAs. As illustrated in Fig.5.1, GaAs is a direct gap semiconductor with a valence band maximum at the center of the first Brillouin zone, Γ. [49] The strong spin-orbit interaction couples the $l = 1$ angular momentum of the p orbitals to the electron spin ($s = 1/2$) resulting in a total spin $J = l + s = 3/2$ for valence holes. There are two energy bands corresponding to $J = 3/2$ and $j_z = \pm 1/2, \pm 3/2$ states (cf. Fig.5.1, heavy and light hole bands). These two bands are degenerate at Γ point. The total $J = 1/2$ band is well below these two bands due to a large spin-orbit splitting, $\delta_{so} \approx 340$ meV (cf. Fig.5.1, the split-off band). Hence, for small concentrations of holes, one can write H_0 in the form of a two-band model: [10, 11, 49]

$$H_0 = \sum_{\mathbf{k}} \hat{c}^{\dagger}_{\mathbf{k}} \hat{\epsilon}_{\mathbf{k}} \hat{c}_{\mathbf{k}}\,, \tag{5.2}$$

where $\hat{\epsilon}_{\mathbf{k}}$ is a 4×4 matrix (indicated by carets) associated with $J = 3/2$ and $j_z = \pm 3/2, \pm 1/2$ states.

In $Ga_{1-x}Mn_xAs$, the Mn ions are believed to be in Mn^{2+} state with a half-filled d shell of total spin $S = 5/2$. The relatively large magnitude of the Mn ion total spin justifies the treatment of them as classical quantities. The interaction between Mn spins and valence holes in general depends on the incoming and outgoing momenta of the holes $\mathbf{k}$ and $\mathbf{k}'$. However, close enough to the Γ point, this momentum dependence is weak and may be

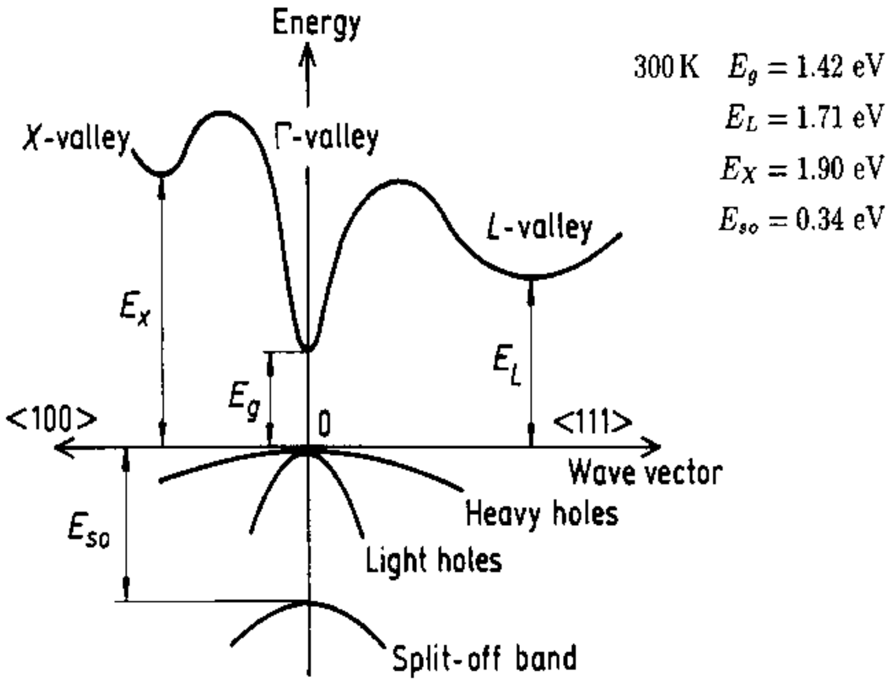

Figure 5.1: The band structure of pure GaAs near the Γ point (center of the first Brillouin zone) showing both the heavy and light hole bands. [www.ioffe.rssi.ru/SVA/NSM/Semicond/GaAs/Figs/421.gif]

ignored. Thus, we arrive at a simple interaction term in Eq.5.1: [10, 50]

$$H_{int}(R_i) = J_c S \cdot J(R_i)\,, \tag{5.3}$$

with J_c the exchange coupling and $J(R_i)$ the spin density of the holes at site i where there is a Mn ion. J in Eq.5.3 represents the total $J = 3/2$ spin of valence holes.

The spin-orbit Hamiltonian in Eq.5.2 can be further simplified to include only spherically symmetric terms and it will be called H_{sp}. To diagonalize H_{sp}, [10] we choose a *chiral basis* in which the spins of valence holes are quantized along the direction of their momenta $\hat{\mathbf{k}}$ (for momenta, carets indicate unit vectors), e.g, $J \cdot \hat{\mathbf{k}} = \pm 3/2$ and $\pm 1/2$. In this basis, the energy of plane waves propagating along $\hat{\mathbf{k}}$ is $\epsilon(k) = k^2/2m_\mu$ with $m_\mu = m_h \approx 0.5m$ and

$m_\mu = m_l \approx 0.07m$ for heavy and light hole masses with $\mu = \pm 3/2$ and $\pm 1/2$ respectively and m is the electron mass. [10] Consequently, in this chiral basis H_{sp} is represented in a simple diagonal form:

$$H_{sp} = \sum_{\mathbf{k},\mu} \frac{k^2}{2m_\mu} c^\dagger_{\mathbf{k},\mu} c_{\mathbf{k},\mu} \,. \tag{5.4}$$

Note that in this equation, neither the operators nor the dispersion are matrices. The heavy hole band contains about 90% of the total valence holes. The diagonalization of H_{sp} comes at the price of a complicated momentum dependent interaction term:

$$H_{int}(R_i) = \frac{J_c}{V} \sum_{\mathbf{k},\mathbf{k}'} \sum_{\alpha} S_i{}^\alpha \hat{c}^\dagger_{\mathbf{k}} \hat{J}^\alpha(\hat{\mathbf{k}},\hat{\mathbf{k}}') \hat{c}_{\mathbf{k}'} e^{-i(\mathbf{k}-\mathbf{k}')\cdot R_i} = \frac{1}{V} \sum_{\mathbf{k},\mathbf{k}'} \hat{c}^\dagger_{\mathbf{k}} \hat{V}_i(\hat{\mathbf{k}},\hat{\mathbf{k}}') \hat{c}_{\mathbf{k}'} e^{-i(\mathbf{k}-\mathbf{k}')\cdot R_i}$$
$$\hat{V}_i(\hat{\mathbf{k}},\hat{\mathbf{k}}') = J_c S_i \cdot \hat{J}(\hat{\mathbf{k}},\hat{\mathbf{k}}') \,, \tag{5.5}$$

with V the total volume of the sample and $\hat{J}^\alpha(\hat{\mathbf{k}},\hat{\mathbf{k}}') = \hat{D}^\dagger(\hat{\mathbf{k}}) \hat{J}^\alpha \hat{D}(\hat{\mathbf{k}}')$ where $\hat{D}$ are spin 3/2 rotation matrices.

We develop a DMFA algorithm that takes advantage of the simple diagonal form of H_{sp} in the chiral basis and the local form of $H_{int}(R_i)$ in the non-chiral basis as follows: [10]

1. We start out with the simple diagonal form of H_{sp} dispersion in the chiral basis $\epsilon_\mu(k) = k^2/2m_\mu$ as represented in Eq.5.4. The non-chiral dispersion $\hat{\tilde{\epsilon}}(k)$ (tildes label the non-chiral basis) can be easily evaluated by a backward rotation of the chiral dispersion $\hat{\epsilon}(k)$ into the non-chiral basis:

$$\hat{\tilde{\epsilon}}(k) = \hat{D}(\hat{\mathbf{k}}) \hat{\epsilon}(k) \hat{D}^\dagger(\hat{\mathbf{k}}) \,. \tag{5.6}$$

2. $\hat{\tilde{\epsilon}}(k)$ is used to calculate the non-chiral coarse-grained Green function matrix with an initial guess for the self-energy, usually zero:

$$\hat{\tilde{\bar{G}}}(i\omega_n) = \frac{1}{N} \sum_{\mathbf{k}} [i\omega_n I - \hat{\tilde{\epsilon}}(k) + \mu I - \hat{\tilde{\Sigma}}(i\omega_n)]^{-1} \,, \tag{5.7}$$

with N the number of $\mathbf{k}$ points in the first Brillouin zone. Note that the self-energy $\hat{\tilde{\Sigma}}(i\omega_n)$ has no momentum dependence as we are implementing the DMFA.

3. The cluster excluded Green function $\hat{\tilde{\mathcal{G}}}_0(i\omega_n)$ is derived to solve the impurity problem as follows:

$$\hat{\tilde{\mathcal{G}}}_0(i\omega_n) = [\hat{\tilde{\bar{G}}}^{-1}(i\omega_n) + \hat{\tilde{\Sigma}}(i\omega_n)]^{-1} . \tag{5.8}$$

4. The interacting part of the Hamiltonian in the non-chiral basis, as appears in Eq.5.3, is treated in a fashion similar to the *coherent potential approximation* (CPA). [42–44] As illustrated in Fig.5.2, in the self-energy diagrammatics for the impurity problem in the chiral basis, we need to average over all the possible configurations of Mn impurity atoms to restore the lattice translational invariance. As a result, each impurity site denoted by x_i or x_j gets renormalized by an impurity concentration factor $\mathbf{x}$. For the moment, we assume that there is an impurity atom on every site of the lattice and therefore $\mathbf{x} = 1$. Solid lines are one-particle cluster excluded hole Green function matrices $\hat{\mathcal{G}}_0(\mathbf{k}, i\omega_n)$ in the chiral basis and dashed lines are impurity-hole interaction matrices $\hat{V}(\mathbf{k}, \mathbf{k}')$ defined in Eq.5.5 (the index i drops as we average over the entire impurity configurations on the lattice). We also sum over all internal momenta while conserving the total momentum at every internal vertex. Thus, for instance, the self-energy contribution corresponding to diagram (c) in Fig.5.2 reads:

$$\hat{\Sigma}^{(c)}(\mathbf{k}_1, i\omega_n) = \frac{1}{N^2}\delta_{\mathbf{k}_1,\mathbf{k}_4} \sum_{\mathbf{k}_2,\mathbf{k}_3} \hat{V}(\mathbf{k}_1, \mathbf{k}_2)\hat{\mathcal{G}}_0(\mathbf{k}_2, i\omega_n)\hat{V}(\mathbf{k}_2, \mathbf{k}_3)\hat{\mathcal{G}}_0(\mathbf{k}_3, i\omega_n)\hat{V}(\mathbf{k}_3, \mathbf{k}_4) . \tag{5.9}$$

For two-impurity crossing diagrams such as diagram (bb) in Fig.5.2, one must subtract the contribution due to sites $i = j$ to avoid overcounting as shown below:

$$\hat{\Sigma}^{(bb)}(\mathbf{k}_1, i\omega_n) = \frac{1}{N^3}\delta_{\mathbf{k}_1,\mathbf{k}_5}\Big(\sum_{\mathbf{k}_2,\mathbf{k}_3,\mathbf{k}_4} \hat{V}(\mathbf{k}_1, \mathbf{k}_2)\hat{\mathcal{G}}_0(\mathbf{k}_2, i\omega_n)\hat{V}(\mathbf{k}_2, \mathbf{k}_3)\hat{\mathcal{G}}_0(\mathbf{k}_3, i\omega_n)\hat{V}(\mathbf{k}_3, \mathbf{k}_4) \times$$

$$\hat{\mathcal{G}}_0(\mathbf{k}_4, i\omega_n)\hat{V}(\mathbf{k}_4, \mathbf{k}_5)\delta_{\mathbf{k}_2-\mathbf{k}_3,\mathbf{k}_5-\mathbf{k}_4} - \frac{1}{N}\Big(\sum_{\mathbf{k}_2,\mathbf{k}_3,\mathbf{k}_4} \hat{V}(\mathbf{k}_1, \mathbf{k}_2)\hat{\mathcal{G}}_0(\mathbf{k}_2, i\omega_n)\hat{V}(\mathbf{k}_2, \mathbf{k}_3)\hat{\mathcal{G}}_0(\mathbf{k}_3, i\omega_n) \times$$
$$\hat{V}(\mathbf{k}_3, \mathbf{k}_4)\hat{\mathcal{G}}_0(\mathbf{k}_4, i\omega_n)\hat{V}(\mathbf{k}_4, \mathbf{k}_5)\Big) \,. \tag{5.10}$$

In the DMFA, we freely sum over all internal momenta in the Feynman diagrams

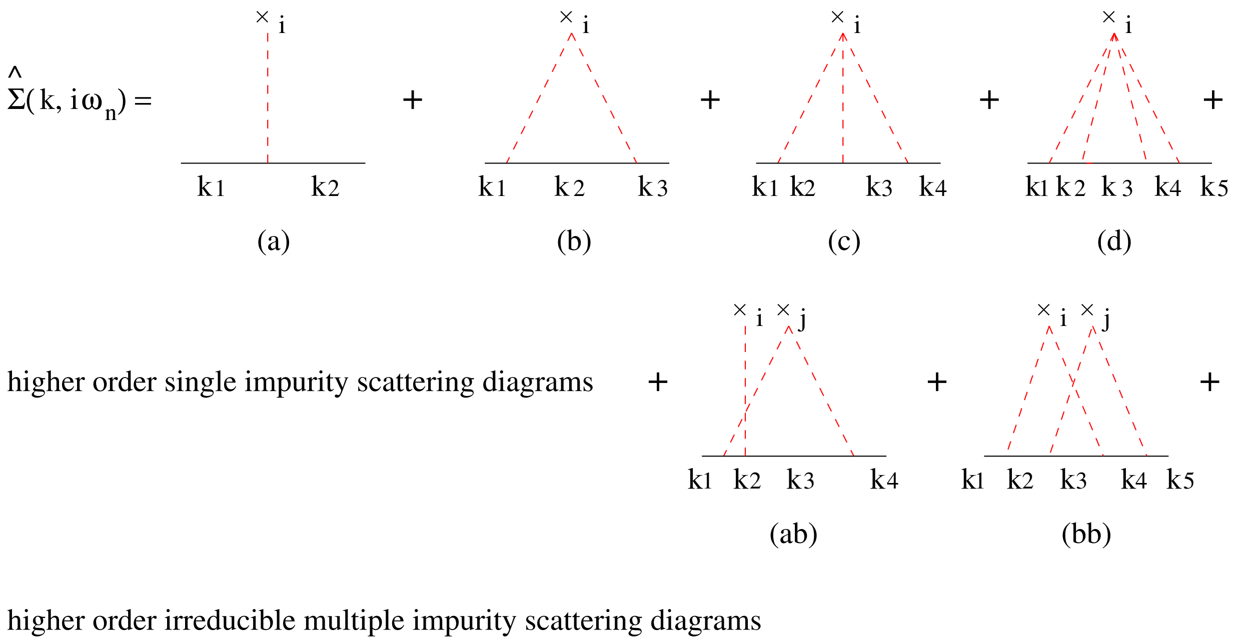

Figure 5.2: Irreducible Feynman diagrammatics for the self-energy in the chiral basis. x$_i$ and x$_j$ are single Mn impurities residing at sites i and j respectively. Solid lines are one-particle cluster excluded hole Green function matrices $\hat{\mathcal{G}}_0(\mathbf{k}, i\omega_n)$ in the chiral basis and dashed lines are impurity-hole interaction matrices $\hat{V}(\mathbf{k}, \mathbf{k}')$. Diagrams (a),(b),(c) and (d) all correspond to single impurity scatterings. Diagrams (ab) and (bb) are irreducible self-energy diagrams associated with scatterings off two different impurity sites and vanish in the DMFA.

relinquishing the total momentum conservation at internal vertices. In order to implement this in diagram (bb) of Fig.5.2, it is sufficient to set $\delta_{\mathbf{k}_2-\mathbf{k}_3,\mathbf{k}_5-\mathbf{k}_4} \to 1/N$ which leads to:

$$\hat{\Sigma}^{(bb)}(\mathbf{k}_1, i\omega_n) = 0 \qquad\qquad (\delta_{\mathbf{k}_2-\mathbf{k}_3,\mathbf{k}_5-\mathbf{k}_4} \to \frac{1}{N}) \tag{5.11}$$

The above result can be generalized to all multiple impurity diagrams. In other words, we find that all multiple impurity diagrams vanish in the DMFA and only the single impurity diagrams survive. This is a tremendous simplification of the original problem since as proven ahead, all the Green functions and interactions in the Feynman diagrams can now be mapped back to the non-chiral basis where they are local.

Knowing that in the non-chiral basis interactions are local:

$$\hat{\mathcal{G}}_0(\mathbf{k}, i\omega_n) = \hat{D}^\dagger(\hat{\mathbf{k}})\hat{\tilde{\mathcal{G}}}_0(\mathbf{k}, i\omega_n)\hat{D}(\hat{\mathbf{k}}) \qquad \hat{V}(\mathbf{k}, \mathbf{k}') = \hat{D}^\dagger(\hat{\mathbf{k}})\hat{\tilde{V}}\hat{D}(\hat{\mathbf{k}}')\,. \tag{5.12}$$

Hence, Eq.5.9 can be rewritten as:

$$\hat{\Sigma}^{(c)}(\mathbf{k}_1, i\omega_n) = \frac{1}{N^2}\delta_{\mathbf{k}_1,\mathbf{k}_4}\sum_{\mathbf{k}_2,\mathbf{k}_3}\hat{V}(\mathbf{k}_1, \mathbf{k}_2)\hat{\mathcal{G}}_0(\mathbf{k}_2, i\omega_n)\hat{V}(\mathbf{k}_2, \mathbf{k}_3)\hat{\mathcal{G}}_0(\mathbf{k}_3, i\omega_n)\hat{V}(\mathbf{k}_3, \mathbf{k}_4) = \frac{1}{N^2}\times$$
$$\delta_{\mathbf{k}_1,\mathbf{k}_4}\sum_{\mathbf{k}_2,\mathbf{k}_3}\hat{D}^\dagger(\hat{\mathbf{k}_1})\hat{\tilde{V}}\hat{D}(\hat{\mathbf{k}_2})\hat{D}^\dagger(\hat{\mathbf{k}_2})\hat{\tilde{\mathcal{G}}}_0(\mathbf{k}_2, i\omega_n)\hat{D}(\hat{\mathbf{k}_2})\hat{D}^\dagger(\hat{\mathbf{k}_2})\hat{\tilde{V}}\hat{D}(\hat{\mathbf{k}_3})\hat{D}^\dagger(\hat{\mathbf{k}_3})\hat{\tilde{\mathcal{G}}}_0(\mathbf{k}_3, i\omega_n)\times$$
$$\hat{D}(\hat{\mathbf{k}_3})\hat{D}^\dagger(\hat{\mathbf{k}_3})\hat{\tilde{V}}\hat{D}(\hat{\mathbf{k}_4})\,. \tag{5.13}$$

But, $\hat{D}(\hat{\mathbf{k}})\hat{D}^\dagger(\hat{\mathbf{k}}) = 1$ and one can show that to all orders for single-impurity self-energy diagrams:

$$\hat{\Sigma}^{(c)}(\mathbf{k}_1, i\omega_n) = \delta_{\mathbf{k}_1,\mathbf{k}_4}\hat{D}^\dagger(\hat{\mathbf{k}_1})\hat{\tilde{V}}\frac{1}{N}\sum_{\mathbf{k}_2}\hat{\tilde{\mathcal{G}}}_0(\mathbf{k}_2, i\omega_n)\hat{\tilde{V}}\frac{1}{N}\sum_{\mathbf{k}_3}\hat{\tilde{\mathcal{G}}}_0(\mathbf{k}_3, i\omega_n)\hat{\tilde{V}}\hat{D}(\hat{\mathbf{k}_4}) + \cdots$$
$$= \delta_{\mathbf{k}_1,\mathbf{k}_4}\hat{D}^\dagger(\hat{\mathbf{k}_1})\hat{\tilde{V}}\bar{\hat{\tilde{\mathcal{G}}}}_0(i\omega_n)\hat{\tilde{V}}\bar{\hat{\tilde{\mathcal{G}}}}_0(i\omega_n)\hat{\tilde{V}}\hat{D}(\hat{\mathbf{k}_4}) + \cdots = \delta_{\mathbf{k}_1,\mathbf{k}_4}\hat{D}^\dagger(\hat{\mathbf{k}_1})\hat{\tilde{\Sigma}}(i\omega_n)\hat{D}(\hat{\mathbf{k}_4})\,. \tag{5.14}$$

So, the DMFA self-energy in the chiral basis can be simply mapped onto the local non-chiral basis self-energy by a backward rotation from $\hat{\mathbf{k}}$ axis to z axis. The simplification achieved by the DMFA due to the elimination of multiple impurity scattering Feynman diagrams allows us to define the local impurity Green function in a CPA manner:

$$\hat{\tilde{G}}_{imp}(i\omega_n) = [\hat{\tilde{\mathcal{G}}}_0^{-1}(i\omega_n) - J_c S \cdot \hat{J}]^{-1} . \tag{5.15}$$

Eq.5.15 is just the summation of all single impurity Green function diagrams to infinite orders.

5. $\hat{\tilde{G}}_{imp}(i\omega_n)$ needs to be averaged over all possible impurity spin orientations at a single impurity site. This task is implemented by defining an effective action: [51]

$$\tilde{S}_{eff}(S) = -\sum_n \log\det\left[\frac{1}{i\omega_n}(\hat{\tilde{\mathcal{G}}}_0^{-1}(i\omega_n) - J_c S \cdot \hat{J})\right] \times e^{i\omega_n 0^+} , \tag{5.16}$$

whereby

$$\mathcal{Z} = \int d\Omega_S \exp[-\tilde{S}_{eff}(S)] , \tag{5.17}$$

and

$$\left\langle \hat{\tilde{G}}_{imp}(i\omega_n) \right\rangle_s = \frac{1}{\mathcal{Z}} \int d\Omega_S \; \hat{\tilde{G}}_{imp}(i\omega_n) \exp[-\tilde{S}_{eff}(S)] . \tag{5.18}$$

Earlier on while discussing the impurity scattering self-energy, we assumed that $\mathbf{x} = 1$ or there is an impurity atom on every lattice site. If $\mathbf{x} < 1$, we need to avergae over all possible impurity configurations as well. For sites with no impurity atoms, $\hat{\tilde{G}}_{imp}(i\omega_n) = \hat{\tilde{\mathcal{G}}}_0(i\omega_n)$. Thus, the total configurationally averaged Green function reads:

$$\hat{\tilde{G}}_{avg}(i\omega_n) = \left\langle \hat{\tilde{G}}_{imp}(i\omega_n) \right\rangle_s \mathbf{x} + \hat{\tilde{\mathcal{G}}}_0(i\omega_n)(1 - \mathbf{x}) . \tag{5.19}$$

6. $\hat{\tilde{G}}_{avg}(i\omega_n)$ is the total local Green function for the system. We can now recompute the

self-energy as:

$$\hat{\tilde{\Sigma}}(i\omega_n) = \hat{\tilde{\mathcal{G}}}_0^{-1}(i\omega_n) - \hat{\tilde{G}}_{avg}^{-1}(i\omega_n)\,. \tag{5.20}$$

This self-energy is used as an input to step 2 and by following the subsequent steps, we self-consistently solve for $\hat{\tilde{G}}_{avg}(i\omega_n)$. At the end of each iteration, we take the difference between the current self-energy matrix (at zeroth Matsubara frequency as $\hat{\tilde{\Sigma}}(i\omega_0)$ includes the largest contribution) and the one evaluated in the previous iteration. The loop ends whenever this difference is less than a desired tolerance. Fig.5.3 illustrates the DMFA algorithm for the Green function.

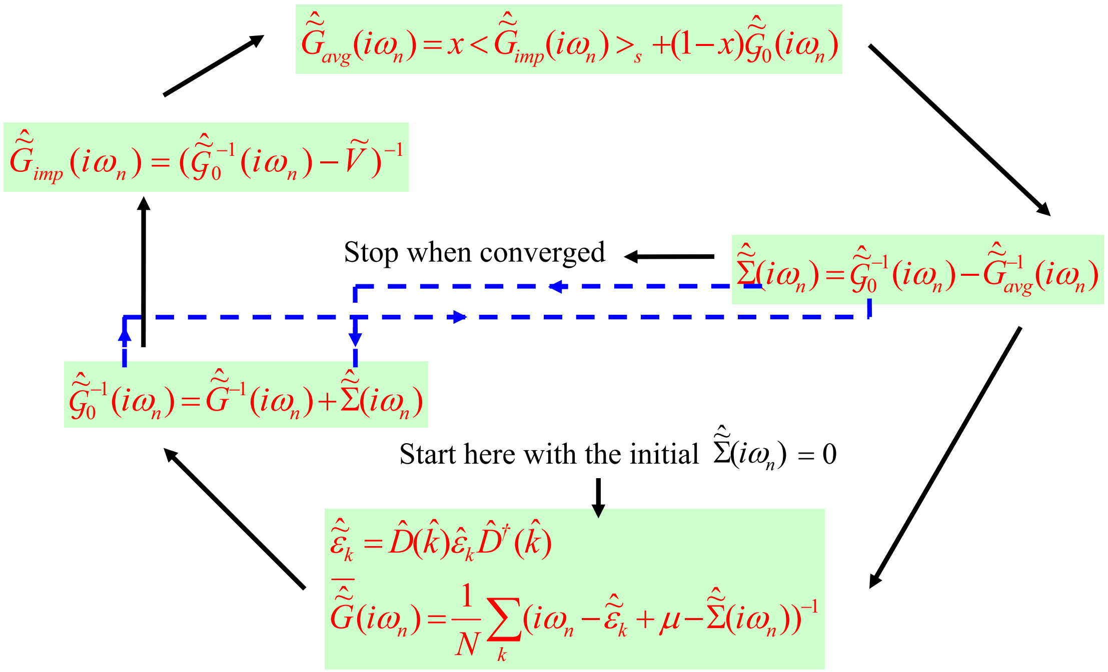

Figure 5.3: The DMFA algorithm for the Green function.

5.3 Results

In this project, the self-consistent algorithm illustrated in Fig.5.3 is implemented in Fortran. The code calculates the local mean field quantities such as $\hat{\tilde{G}}(i\omega_n)$ and impurity spin magnetization m_z self-consistently by averaging over all possible impurity spin orientations and configurations. A significant amount of effort was spent improving the numerical approximations as well as increasing the computational speed. Summations over the Matsubara frequencies are cut off at relatively high frequencies. To avoid undesirable effects and errors at high frequencies due to these cutoffs, these summations are treated analytically up the the second order term in the high frequency expansion of their summands. Integrations over momenta in the first Berillouin zone are also performed over a mesh that is denser inside the Fermi surface and coarser outside because lower energy states dominate the physics at low temperatures. Therefore, higher energy states take less calculations and consequently less computational time. In addition, standard numerical routines have been utilized in the code in order to optimize its accuracy. For instance, all integrations are done numerically using the *Gaussian Quadratures* technique. [52] Also, to improve convergence, an elegant scheme called *Broyden's method* [53] was employed.

By using the effective action and partition function defined in Eq.5.16 and Eq.5.17 respectively, the magnetization for local Mn spins along the z axis can be computed as:

$$m_z = \frac{1}{\mathcal{Z}} \int d\Omega_S S_z \exp[-(\tilde{S}_{eff}(S) - S \cdot H)]\,, \tag{5.21}$$

in which an infinitesimal magnetic field H was applied to break the symmetry along a preferential direction (Here, the z axis). The mean field approximation provides us with following analytic expressions for magnetization as a function of temperature and magnetic field in the vicinity of the ferromagnetic phase transition temperature T_c:

$$m_z = \frac{25}{12}\left[\, t \,\left(\sqrt[3]{-\frac{6h}{5} + \frac{2}{5}\sqrt{\frac{16(t-1)^3}{5} + 9h^2}} + \sqrt[3]{-\frac{6h}{5} - \frac{2}{5}\sqrt{\frac{16(t-1)^3}{5} + 9h^2}}\,\right) + h \,\right]$$

$$T > T_c$$

$$m_z = \frac{25}{12}\left(\frac{4t}{\sqrt{5}}\sqrt{1-t}\ \cos\left[\,\frac{1}{3}\arctan\left(\sqrt{\frac{16(1-t)^3}{45\ h} - 1}\,\right)\right] + h \right)$$

$$T < T_c\,, \tag{5.22}$$

where

$$t = \frac{T}{T_c} \qquad \mathit{and} \qquad h = \frac{H}{T_c}\,. \tag{5.23}$$

Thus, by plotting m_z versus T, one can calculate T_c by fitting the data to the above formulae.

Two additional parameters are also introduced here. One is a reduced effective mass for heavy and light holes:

$$\frac{1}{\mu} = \frac{1}{m_h} + \frac{1}{m_l}\,, \tag{5.24}$$

and the other is the ratio of light and heavy hole effective masses:

$$\alpha = \frac{m_l}{m_h}\,. \tag{5.25}$$

The above parameterization enables us to switch off the chirality by setting $\alpha = 1$ while keeping μ constant. This way the total non-interacting energy dispersion remains intact but $j_z = 3/2$ and $j_z = 1/2$ holes fall onto a single band and become degenerate. Thus, the effect of chirality may be studied by tuning α for fixed μ.

The value of the hole-impurity coupling J_c determines how strongly valence band holes interact with Mn impurity sites in the lattice. For J_c larger than certain values, holes can form bound states with the Mn impurity atoms and as a result, there will be an impurity band forming inside the pure GaAs gap. Usually, the formation of this state is manifest when the holes' density of states splits into two separate regions. [54] Here, instead of plotting the density of states, the discontinuity of the holes' chemical potential for carrier concentration n_h equal to the impurity concentration $\mathbf{x}$ indicates the impurity band formation.

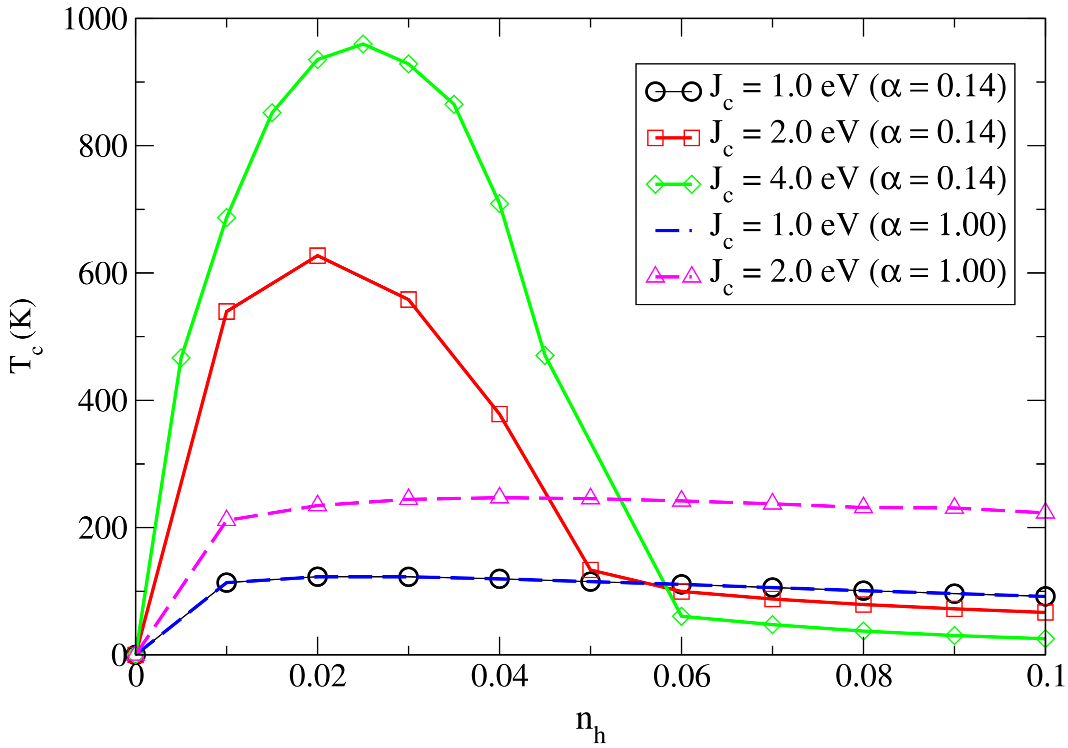

Figure 5.4: Phase transition temperature T_c versus carrier concentration n_h for $\mathbf{x} = 0.05$ and various J_c values.

Fig.5.4 presents some preliminary results for phase transition temperatures T_c versus carrier concentration n_h for various values of coupling constant J_c (more simulations are in progress to obtain more precise T_c estimates). For $J_c = 1.0$ eV and $\alpha = 0.14$ (The chiral ratio), the system is considerably far from the impurity band regime and T_c has a relatively slow variation with respect to n_h. For $J_c = 2.0$ eV and $\alpha = 0.14$, the system is beyond the J_c threshold for the impurity band formation. The physics is dominated by the spin-polarized impurity band and T_c is maximum when the impurity band is half filled ($n_h = \mathbf{x}/2$). [54] For $J_c = 4.0$ eV and $\alpha = 0.14$, the impurity band regime is well established and the maximum T_c is large. According to the results illustrated in Fig.5.4, J_c between $1.0 < J_c < 2.0$ eV would correspond to the maximum T_c obtained from experimental $T_c \approx 110K$. [9, 55–57]. The results for $J_c = 1.0$ eV and $\alpha = 1.0$ (single band ratio) almost overlap with results for the chiral ratio. However, at $J_c = 2.0$ eV the difference between the chiral and single band results is evident. T_c corresponding to $\alpha = 1.0$, are higher than T_c for $\alpha = 0.14$ up to $n_h = \mathbf{x}$. This may be in support of the Zaránd and Jankó claim [10] that due to the chirality of the Hamiltonian, $Ga_{1-x}Mn_xAs$ is a *frustrated* ferromagnet. Nevertheless, below $n_h = \mathbf{x}$, the chiral ratio yields higher T_c. One possible explanation is that unlike the chiral case, when $\alpha = 1.0$, the system is not yet in the impurity band regime for $J_c = 2.0$ eV. The reason may be that for $\alpha = 1.0$, both $j_z = 3/2$ and $j_z = 1/2$ holes are degenerate and have higher kinetic energy due to their reduced effective masses. Hence, higher J_c are required to force both of them towards the impurity band state. While for the chiral case, $j_z = 3/2$ holes can form the impurity band state first and by further increasing J_c, the second impurity band for $j_z = 1/2$ holes will form. The $\alpha = 1.0$ impurity band results for T_c are in progress. It is however believed that for $\alpha = 1.0$, the impurity band regime will be established at larger J_c compared to the chiral case.

In Fig.5.5, the chemical potential has been plotted as a function of carrier concentration n_h for $T = 0.05$ eV, $\alpha = 0.14$ and also different values of J_c coupling. At $J_c = 4.0$ eV, there is a strong indication of impurity band formation due to the discontinuity of holes' chemical potential for $n_h = \mathbf{x}$. Because of this discontinuity, it is very difficult to calculate T_c for $n_h = \mathbf{x}$ in the impurity band regime and that is why in Fig.5.4, the value of T_c for $n_h = \mathbf{x}$ and $J_c = 4.0$ eV is missing. Instead, T_c was calculated for two other values of n_h neighboring

x. The chemical potential results for $\alpha = 1.0$ case are still in progress.

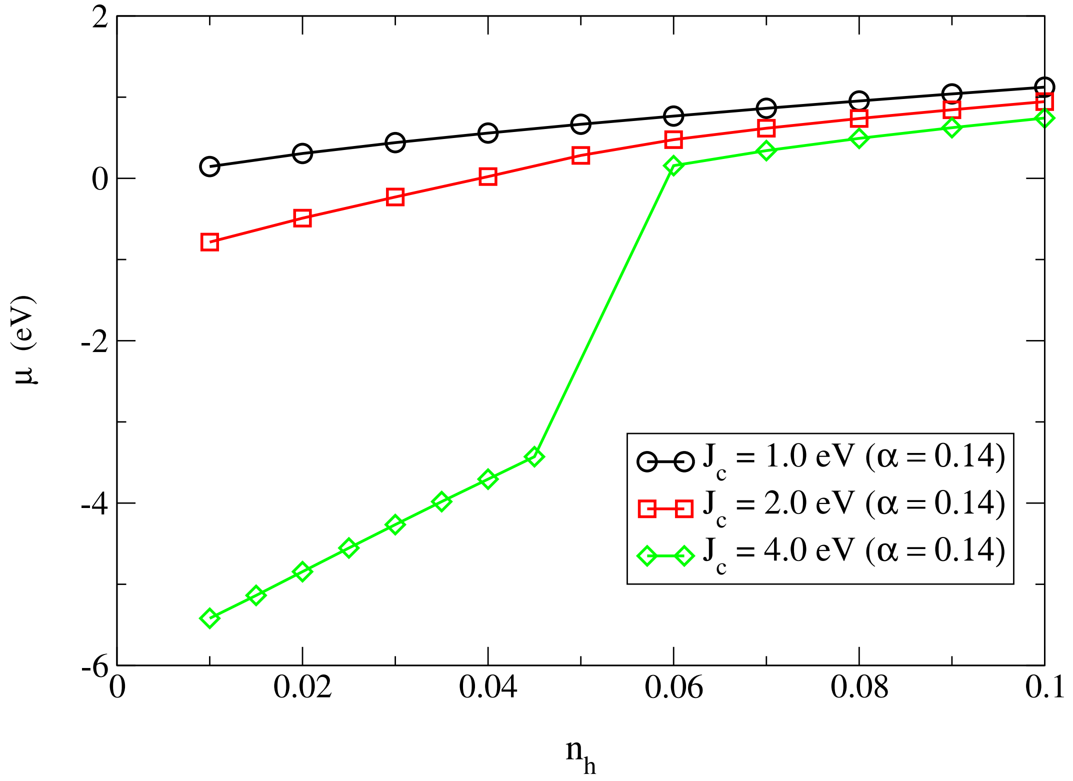

Figure 5.5: Variation of the chemical potential μ versus carrier concentration n_h for $T = 0.05$ eV and different values of J_c coupling.

Lastly, the other physical quantity of interest in this project is the carrier polarization, i.e, the difference between spin-up and spin-down carrier concentrations defined as follows:

$$\mathcal{P} = \frac{1}{\beta}\sum_{i\omega_n}\left[3\Big(\hat{\tilde{G}}_{11}(i\omega_n) - \hat{\tilde{G}}_{44}(i\omega_n)\Big) + \Big(\hat{\tilde{G}}_{22}(i\omega_n) - \hat{\tilde{G}}_{33}(i\omega_n)\Big)\right], \tag{5.26}$$

where β is the inverse of temperature. The first term is weighted by an overall factor of 3 as it corresponds to $j_z = 3/2$ holes and the second term corresponds to $j_z = 1/2$ holes. While the system is in paramagnetic phase, $\hat{\tilde{G}}_{11}(i\omega_n) = \hat{\tilde{G}}_{44}(i\omega_n)$ and $\hat{\tilde{G}}_{22}(i\omega_n) = \hat{\tilde{G}}_{33}(i\omega_n)$. Hence, $\mathcal{P} = 0$. $\mathcal{P}$ becomes finite as the system turns ferromagnetic. This quantity is of great importance from *spintronics* point of view as it measures the spin polarization of the holes which is the underlying phenomena behind information transport via carriers spin degrees of freedom. Work on the computation, analysis and study of $\mathcal{P}$ is already in progress and results will soon be presented.

5.4 Summary

This chapter was focused on the study of magnetism in magnetically doped semiconductors with the specific example of $\mathrm{Ga}_{1-x}\mathrm{Mn}_x\mathrm{As}$. Recently, there has been a great amount of interest in magnetic semiconductors on both fundamental and applied research sides. Amongst a number of interesting models proposed so far, the model employed by G. Zaránd and B. Jankó [10] was of specific attention as it incorporates both the strong spin-orbit coupling effect in the band structure of the carriers and the interaction with magnetic impurity atoms. The Hamiltonian for this model is a simplification of a more general Hamiltonian first introduced by Kohn and Luttinger. [11, 47, 48]. The spin-orbit coupling part of this simplified Hamiltonian can be diagonalized by the quantization of carriers spins along their momentum directions that maps the Hamiltonian onto a chiral basis. Based upon a perturbation theory approach, (RKKY) Zaránd and Jankó conclude that due to the chirality of this Hamiltonian, $\mathrm{Ga}_{1-x}\mathrm{Mn}_x\mathrm{As}$ is a *frustrated* ferromagnet exhibiting features similar to spin glasses and spin ice compounds. [10] In this project, for the first time, a systematic approach predicated upon the DMFA was developed and invoked in order to more precisely address the effect of chirality in Zaránd and Jankó Hamiltonian. A self-consistent algorithm was developed to implement the DMFA for this problem and also calculate the magnetization, ferromagnetic phase transition temperature T_c and carrier spin polarization for a variety of physically relevant parameters. Our formalism allows us to switch the chirality on and off and compare the results of both modes.

Our findings so far, even though rather preliminary and incomplete, to some extent support the conclusions of Zaránd and Jankó [10] that chirality leads to frustration in $Ga_{1-x}Mn_xAs$ system. However, it also seems evident that the impurity band regime is established more easily in the chiral mode compared to the non-chiral mode as a result of which T_c can be still higher in the chiral mode for low carrier concentrations. More solid conclusions and arguments require further data production and are to appear soon.

Chapter 6

Summary

6.1 Summary

In this dissertation, various approximation methods and algorithms for studying electron-electron correlations are introduced, discussed and implemented for different physical systems and models. A number of these models (like the Hubbard model) have been extensively studied so that some of their most significant physical properties under certain conditions are quite well known. These models serve as tools to evaluate the validity and also limitations of these techniques. One is also capable of making a comparison among these various methods in terms of their success in reproducing and illustrating the well known properties of the models and systems they are applied to.

Chapter 1 begins with an introduction on *strongly correlated electron systems* and some of their most striking features. Next, there follows the *dynamical mean field approximation* (DMFA) as the first approximation approach to incorporate electron-electron correlations locally in space as well as dynamically in time. The algorithm for this technique requires a full suppression of the non-local correlations by relinquishing the momentum conservation at all the internal vertices of the Feynman diagrams or in other words coarse-graining over the entire first Brillouin zone. Considering the limited capability of the DMFA to yield realistic physics when non-local correlations play major roles, the *dynamical cluster approximation* (DCA) and *cellular dynamical mean field theory* (CDMFT) are presented. Both the DCA and CDMFT systematically add non-local corrections to the DMFA by restoring correlations within clusters in the first Brillouin zone and real lattice respectively. The DCA (CDMFT) becomes exact as the size of clusters approaches zero (infinity) in the first Brillouin zone (real lattice) and it reduces to the DMFA when one cluster spans the entire first Brillouin zone (the cluster in real lattice includes only one lattice site).

In chapter 2, the DCA is applied to the Hubbard model in conjunction with the *fluctuation exchange approximation* (FLEX). The FLEX is a perturbative approach to compute the self-energy of an interacting electron system. In the FLEX, certain classes of Feynmn diagrams that can be summed over to all orders using geometric series are selected out of the entire Feynman diagrammatics and they account for the total self-energy of the interacting system. This approximation proves unrealistic in the limit of strong Hubbard interaction. Nevertheless, it can serve as a tool for testing the DCA. This chapter makes a comparison between physical results obtained using the DCA and finite size lattices. It first concludes that the DCA is complementary to the finite size lattice techniques in the sense that it underestimates the effect of correlations in most physical features whereas finite size lattices freeze rather fast as the temperature falls and the correlation effects are therefore always overestimated by them. Secondly, it also turns out that the DCA is more favorable because it consumes far less computer time. To get as accurate results using finite size lattices, one needs to invoke large finite size lattices taking a lot of memory and CPU time on computers. Finally, it proves that employing a DCA like coarse-graining in frequency space for Matsubara frequencies fails since it leads to the violation of causality. However, if one were to use a real frequency formalism for Feynman diagrammatics even at finite temperatures, the DCA would be implementable.

In chapter 3, the microscopic theory of the DCA is presented in detail. This microscopic theory prescribes a unique procedure for implementing the DCA based on the Feynman diagrammatics for the thermodynamic potential. The Feynaman diagrams for thermodynamic potential are closed (no external legs) diagrams that can be classified into two groups of *compact* (no self-energy insertions) and *non-compact* (having self-energy insertions). The DCA is implemented by coarse-graining the Green function only in the compact part of the thermodynamic potential. The non-compact part is explicitly constructed using the full non-coarse-grained Green function. It can be illustrated that constructing non-compact diagrams using the coarse-grained Green functions is associated with significantly large errors compared to compact diagrams and therefore must be avoided. Moreover, compact diagrams include vertex corrections in them with four Green function legs while non-compact diagrams include self-energy corrections with two Green function legs. As it can be shown that Green functions fall off exponentially as a function of distance in real lattice, the compact diagrams generate smaller errors due to being coarse-grained because they fall off exponentially more rapidly.

Chapter 4 is focused on a comparison between the DCA and CDMFT in terms of their convergence as a function of their cluster sizes. Earlier on in chapter 1, it is demonstrated analytically that the CDMFT converges with corrections of order $1/L_c$ while the DCA converges with corrections of order $1/{L_c}^2$ where L_c is the linear size of the cluster. In this chapter, a Hamiltonian called the *simplified one-dimensional large-N model* with an exact self-consistent mean field solution is invoked to be approximated by both the DCA and CDMFT. By plotting the DCA and CDMFT results for this model versus $1/L_c$ and observing how they converge towards the exact solution at large L_c, the predicted converging schemes of both the DCA (with $1/{L_c}^2$ corrections) and CDMFT (with $1/L_c$ corrections) are explicitly confirmed. It also turns out that the DCA is far less numerically expensive compared to the CDMFT in terms of the computational CPU time. However, the CDMFT has the advantage of yielding a smooth self-energy curve in momentum space as opposed to a step function form of the DCA self-energy on the cluster points.

Chapter 5 concerns one of the most striking phenomena in modern physics and industry, namely, *spintronics*. In spintronics, the main focus is to make semiconductors ferromagnetic because the spin degree of freedom of charge carriers (electrons or holes) can then be used to carry information in addition to the charge. However, most semiconductors are resistive against the solution of magnetic impurities in them. Recently, the *molecular-beam epitaxy* technique, [9, 46] led to a successful growth of $\mathrm{Ga}_{1-x}\mathrm{Mn}_x\mathrm{As}$. In $\mathrm{Ga}_{1-x}\mathrm{Mn}_x\mathrm{As}$, the effects of the spin-orbit coupling for valance band holes of pure GaAs and also their interaction with Mn impurity atoms are incorporated in a simplified Kohn-Luttinger [11, 47, 48] Hamiltonian derived by G. Zaránd and B. Jankó. [10]. The non-interacting spin-orbit coupling of this Hamiltonian is diagonalized in a *chiral basis* where the spins of the holes are quantized along the direction of their momenta. By using a perturbation theory approach (RKKY), Zaránd and Jankó conclude that due to the chirality of the spin-orbit coupling in the Hamiltonian, $\mathrm{Ga}_{1-x}\mathrm{Mn}_x\mathrm{As}$ is a *frustrated* ferromagnet exhibiting features similar to spin glasses and spin ice compounds. [10] Using the DMFA as a more physical and systematic technique, the magnetization and whereby the ferromagnetic phase transition temperature T_c are computed for different values of impurity-hole coupling J_c, the concentration of Mn impurities $\mathbf{x}$ and valence carrier concentration n_h. The goal is to study the effect of chirality in the Hamiltonian describing $\mathrm{Ga}_{1-x}\mathrm{Mn}_x\mathrm{As}$ system by comparing the results obtained by this Hamiltonian in both the chiral mode and a single band mode in which the chirality has been switched off.

6.2 Future developments

In this dissertation, the DCA technique is applied to the Hubbard model using the FLEX. The FLEX, even though not so precise as nearly exact algorithms such as QMC, can nicely illustrate the utility of the DCA and its superiority over finite size lattice approaches (with periodic boundary conditions). In addition, there is provided an elaborate microscopic theory as a unique and accurate prescription for the DCA implementation. The DCA is also compared with the CDMFT and certain advantages of the DCA over the CDMFT are discussed and emphasized (The CDMFT, however, has the advantage of yielding a smooth self-energy curve over the DCA as mentioned in chapter 4). As a result of the entire above-mentioned studyings and investigations, the DCA is bench marked as a promising candidate to be further employed in a variety of correlated electron systems using more sophisticated cluster solving algorithms such as QMC and NCA. Nevertheless, the outlook for the FLEX-nearly approach is still very significant. The FLEX is capable of adequately describing the long-range physics of correlated electron systems with spin and charge fluctuations. On the other hand, nearly exact algorithms such as QMC, while precisely describing the short-range physics such as moment formation, are too expensive to perform for large clusters. Hence, the combination of the FLEX and QMC using the DCA could capture both the short-range and long-range physics associated with electron-electron correlations and can therefore be considered a prospective project in the future.

The discussion of ferromagnetic semiconductors in this dissertation is the first step to employ the DMFA in order to study the effects of strong spin-orbit coupling and disorder in $Ga_{1-x}Mn_xAs$ (or other III-V doped semiconductor compounds). The chief focus of what is presented in this dissertation is the significance of the chirality in the physics of $Ga_{1-x}Mn_xAs$ in particular as a magnetic semiconductor system. However, far more physical information and applications can be achieved by using the techniques implemented and developed in this project. To mention a few, the calculation of the holes polarization, charge transport coefficients and AC susceptibilities, the study of the *Angle Resolved Photo Emission Spectroscopy* (ARPES), the extension to the other semiconductor systems and the possibility of invoking cluster techniques such as the DCA in order to introduce non-local correlations essential for studying the glassy behavior of magnetic semiconductors are already in progress.

Bibliography

[1] J. J. Deisz, D. W. Hess and J. W. Serene. *Phys. Rev. Lett.* **76**, 1312 (1996).

[2] K. Aryanpour, M. H. Hettler and M. Jarrell. *Phys. Rev. B* **65**, 153102 (2002).

[3] K. Aryanpour, M. H. Hettler and M. Jarrell. *Phys. Rev. B.* **67**, 085101 (2003).

[4] K. Aryanpour, Th. A. Maier and M. Jarrell. Preprint cond-mat/0301460.

[5] P. Fulde. *Electron Correlations in Molecules and Solids* (Springer, 1995).

[6] F. C. Zhang and T. M. Rice. *Phys. Rev. B.* **37**, 3759 (1988).

[7] J. Kondo. *Progr. Theor. Phys.* **32**, 37 (1964).

[8] P. W. Anderson. *Phys. Rev.* **124**, 41 (1961).

[9] H. Munekata, H. Ohno, S. von Molnár, A. Segmüller, L. L. Chang and L. Esaki. *Phys. Rev. Lett.* **63**, 1849 (1989).

[10] G. Zaránd and B. Jankó. *Phys. Rev. Lett* **89**, 047201 (2002).

[11] W. Kohn and J. M. Luttinger. *Phys. Rev.* **98**, 915 (1955).

[12] M. Jarrell. *Phys. Rev. Lett.* **69**, 168 (1992).

[13] A. Georges and G. Kotliar. *Phys. Rev. B* **45**, 6479 (1992).

[14] E. Müller-Hartmann. *Z.Phys. B: Condens. Matter* **74**, 507 (1989).

[15] W. Metzner and D. Vollhardt. *Phys. Rev. Lett.* **62**, 324 (1989).

[16] M. H. Hettler, M. Mukherjee, M. Jarrell and H. R. Krishnamurthy. *Phys. Rev. B* **61**, 12739 (2000).

[17] D. D. Betts and G. E. Stewart. *Can. J. Phys.* **75**, 47 (1997).

[18] D. F. Eliot and K. R. Rao. *Fast Transformations: Algorithms, Analyses, Applications* (Academic Press, New York, 1982).

[19] G. Kotliar, S. Y. Savarasov, G. Pálsson and G. Biroli. *Phys. Rev. Lett.* **87**, 186401 (2001).

[20] Th. A. Maier, O. Gonzalez, M. Jarrell and Th. Schulthess. *Two Quantum Cluster Approxiamtions, to be published in Computer Simulations Studies in Condensed Matter Physics X, edited by D.P. Landau, S.P. Lewis, and H. B. Schüttler (cond-mat/0205460)* (Springer-Verlag, Berlin Heidelberg).

[21] I. Affleck and B. Marston. *Phys. Rev. B.* **37**, 3774 (1988).

[22] Th. A. Maier and M. Jarrell. *Phys. Rev. B.* **65**, 041104 (2002).

[23] Hideo Ohno. *Journal of Magnetism and Magnetic Materials* **200**, 110 (1999).

[24] P. G. J. van Dongen. *Phys. Rev. B.* **50**, 14016 (1994).

[25] M. H. Hettler, A. N. Tahvildar-Zadeh, T. Pruschke M. Jarrell and H. R. Krishnamurthy. *Phys. Rev. B.* **58**, 7475 (1998).

[26] Th. A. Maier, M. Jarrell, Th. Pruschke and J. Keller. *Eur. Phys. J.* **13**, 613 (2000).

[27] Y. Imai and N. Kawakami. *Phys. Rev. B.* **65**, 233103 (2002).

[28] N. E. Bickers, D. J. Scalapino and S. R. White. *Phys. Rev. Lett.* **62**, 961 (1989).

[29] N. E. Bickers and S. R. White. *Phys. Rev. B.* **43**, 8044 (1990).

[30] J. W. Serene and D. W. Hess. *Phys. Rev. B.* **44**, 3391 (1991).

[31] G. Baym. *Phys. Rev.* **127**, 1391 (1962).

[32] H. J. Vidberg and J. W. Serene. *J. Low Temp. Phys.* **19**, 179 (1977).

[33] J. J Deisz, D. W. Hess and J. W. Serene (To appear in "Recent Progress In Many Body Theories" vol. 4, edited by E. Schachinger, et al. (Plenum, New York)) . Preprint cond-mat/9411026R.

[34] M. A. Jenkins and J. F. Traub. *Comm. ACM* **15** (97-99) (1972). (The routine is available at http://www.netlib.org/tomspdf/419.pdf).

[35] Th. Maier (Private communications).

[36] T. Pruschke (Private communications).

[37] T. Pruschke, M. Jarrell and J. K. Freericks. *Adv. in Phys.* **42**, 187 (1995).

[38] A. Georges, G. Kotliar, W. Krauth and M. Rozenberg. *Rev. Mod. Phys.* **68**, 13 (1996).

[39] A. A. Abrikosov, L. P. Gorkov and I. E. Dzyaloshinski. *Methods of Quantum Field Theory in Statistical Physics* (Dover, New York, 1975).

[40] Müller-Hartmann actually showed this for self energy diagrams.

[41] F. Ducastelle. *J. Phys. C. Sol. State. Phys.* **7**, 1795 (1974).

[42] D. W. Taylor. *Phys. Rev.* **156**, 1017 (1967).

[43] P. Soven. *Phys. Rev.* **156**, 809 (1967).

[44] P. L. Leath and B. Goodman. *Phys. Rev.* **148**, 968 (1966).

[45] D. Sénéchal, D. Perez and M. Pioro-Ladrière. *Phys. Rev. Lett.* **84**, 522 (2000).

[46] J. K. Furdyna. *J. Appl. Phys.* **64**, R29 (1988).

[47] T. Dietl, H. Ohno and F. Matsukura. *Phys. Rev. B.* **63**, 195205 (2001).

[48] M. Abolfath, T. Jungwirth, J. Brum and A. H. MacDonald. *Phys. Rev. B.* **63**, 054418 (2001).

[49] J. S. Blakemore. *J. Appl. Phys.* **53**, R123 (1982).

[50] P. Kacman. *Semicond. Sci. and Technol.* **16**, R25 (2001).

[51] N. Furukawa. Preprint cond-mat/9812066.

[52] W. H. Press, S. A. Teukolsky and W. T. Vetterling. *Numerical Recipes in Fortran 77: The Art of Scientific Computing* (Cambridge University Press, 1992).

[53] D. D. Johnson. *Phys. Rev. B.* **38**, 12807 (1988).

[54] A. Chattopadhyay, S. Das Sarma and A. J. Millis. *Phys. Rev. Lett.* **87**, 227202 (2001).

[55] H. Ohno, H. Munekata, T. Penney, S. von Molnár and L. L. Chang. *Phys. Rev. Lett.* **68**, 2664 (1992).

[56] H. Ohno, A. Shen, F. Matsukura, A. Oiwa, A. Endo, S. Katsumoto and Y. Iye. *Appl. Phys. Lett.* **69**, 363 (1996).

[57] A. Van Esch, L. Van Bockstal, J. De Boeck, G. Verbanck, A. S. van Steenbergen, P. J. Wellmann, B. Grietens, R. Bogaerts, F. Herlach and G. Borghs. *Phys. Rev. B.* **56**, 13103 (1997).